Theses and Dissertations | Student Graduate Works

3-21-2019

Tracking Shock Movement on the Surface of an Oscillating, Straked Semispan Delta Wing

Justin A. Pung

Recommended Citation

TRACKING SHOCK MOVEMENT ON THE SURFACE OF
AN OSCILLATING, STRAKED SEMISPAN DELTA WING

THESIS

Justin A. Pung, Capt, USAF

AFIT-ENY-MS-19-M-238

DEPARTMENT OF THE AIR FORCE
AIR UNIVERSITY

AIR FORCE INSTITUTE OF TECHNOLOGY

Wright-Patterson Air Force Base, Ohio

The views expressed in this thesis are those of the author and do not reflect the official policy or position of the United States Air Force, Department of Defense, or the United States Government.

Tracking Shock Movement on the Surface of an Oscillating, Straked Semispan Delta Wing

THESIS

Presented to the Faculty

Department of Aeronautics and Astronautics

Graduate School of Engineering and Management

Air Force Institute of Technology

Air University

Air Education and Training Command

In Partial Fulfillment of the Requirements for the

Degree of Master of Science in Aeronautical Engineering

Justin A. Pung, BSAE

Capt, USAF

March, 2019

AFIT-ENY-MS-19-M-238

Tracking Shock Movement on the Surface of an Oscillating, Straked Semispan Delta Wing

Justin A. Pung, BSAE
Capt, USAF

Approved:

//signed//	01 March 2019
Lt Col Darrell S. Crowe, PhD (Committee Chairman)	Date
//signed//	01 March 2019
Dr. Donald L. Kunz (Committee Member)	Date
//signed//	01 March 2019
Dr. Mark F. Reeder (Committee Member)	Date

Abstract

A recent research effort, sponsored by the Air Force Office of Scientific Research, numerically investigated the unsteady aerodynamic flow field around an oscillating, straked, delta wing. The study was centered on determining the importance of the unsteady aerodynamic forces acting as a driver for a nonlinear motion known as limit cycle oscillations. The current effort focused on creating a computational model to compare to the results of previous tests and modeling efforts and discover new information regarding the onset of LCO.

The computational model was constructed using the Cartesian overset capabilities of the CREATE-AV™fixed wing fluid dynamics solver Kestrel. The geometry of the model was based on an Euler model that was recently developed to investigate the same experiments. Adaptive mesh refinement was also employed during the numerical simulations to better capture the translation of the shock along the surface of the semispan. The developed numerical model was tested at a variety of flow conditions, including varying free-stream Mach numbers, starting trim angles, oscillation amplitudes and oscillation frequencies.

The results showed a number of trends that could influence the onset and sustainment of LCO. First, the aerodynamic phenomena of shock-induced trailing edge separation (SITES) was observed during a number of the simulations. Popular among aeroelasticians as a possible source of LCO, SITES is thought to cause a change in the aerodynamic forces acting on the flexible structure, propagating the LCO motion. Second, the quantitative results of the computational model showed good agreement with published, qualitative observations made during wind tunnel experiments. Third, a separation bubble was observed aft a shock on the top surface of the semispan. This previously unobserved flow feature could have a significant impact on the forces acting on the model during the oscillation.

iv

Table of Contents

List of Figures

viii

ix

List of Tables

List of Symbols

xiii

List of Abbreviations

Tracking Shock Movement on the Surface of an Oscillating, Straked Semispan Delta Wing

I. Introduction

Unsteady aerodynamic forces and their impact on flexible structures have been an important area of study for the entirety of heavier-than-air flight. As modern aircraft designs continue to push the limits of existing flight capabilities, more complex flow phenomena are produced. Thin, highly cambered airfoils and vortex-generating structures, such as strakes, can provide improved performance for modern aircraft but also add a layer of complexity to the flow physics. More advanced flow features can result in even more complicated fluid-structure interaction (FSI) problems. Strong aeroelastic instabilities and nonlinearities can be produced from these interactions which can lead to a number of detrimental effects on the structure of an aircraft. One such nonlinearity is known as limit cycle oscillations (LCO).

The LCO motion is an anti-symmetric oscillatory motion of the wings that has been observed on a variety of high performance aircraft in the Department of Defense (DoD) arsenal, like the F-16. The oscillations of the wings cause a lateral motion of the fuselage which can negatively impact mission capability. Related to the aerodynamic instability flutter, the point of LCO onset is dependent on a variety of flight conditions, like angle of attack and flight speed. Wing loading is also an important factor in LCO onset, with different munition combinations having significantly different onset speeds. The complicated, nonlinear nature of the LCO instability make developing dynamic models for the motion difficult. In order to determine the LCO onset of the different configurations, flight testing is usually required. For the F-16, these flight tests are typically conducted by the Air Force SEEK EAGLE Office (AFSEO) in order to certify specific munition combinations for operational use.

Responsible for testing, evaluating and certifying external equipment and munitions for the Air Force, AFSEO conducts the flutter testing for new F-16 loadouts.

1

Normally, LCO onset points are also investigated during the flutter flight testing process. Because of the large number of different loadout options, testing every possible combination would be extremely expensive in terms of funding and manpower. In order to limit the size of the test matrix, a predictive capability for determining the point of LCO onset is desirable. By accurately determining the munition configurations and flight conditions which are most likely to exhibit LCO, a test plan can be designed to examine those conditions while avoiding more predictably stable conditions. Limiting the scope of the flight test matrix could lead to significant savings of both manpower and funding.

1.1 Background and Motivations

Limit cycle oscillations are a nonlinear form of the aeroelastic instability flutter. As defined by Hodges, flutter is a "dynamic instability of a flight vehicle associated with the interaction of aerodynamic, elastic and inertial forces" [1]. Flutter occurs when the aerodynamic and structural forces cause the flexible structure to oscillate at the harmonic frequency of the structure. The amplitude of the oscillation continues to grow over time, as shown in Figure 2.1, until the flow parameters change or the motion causes the catastrophic failure of the structure. Because of the danger flutter presents, the onset point of the phenomenon is found using both numerical models and flight testing. Since they are related, the onset point for LCO is often discovered when flight testing for flutter.

As the name suggests, there are three notable features of the LCO motion [2]. First, the combination of aerodynamic and structural forces cause an anti-symmetric **oscillation** of the aircraft wings. Second, unlike flutter, the amplitude of the oscillation does not grow with time but instead reaches a **limited** or stable value. Figure 1.2 shows the stable amplitude of LCO over time. Finally, the oscillatory motion is also **cyclic**, meaning that it repeats itself over time. Limit cycle oscillations have typically been a problem for high performance aircraft with wingtip launchers, like the F-16 and F-18. High flight speeds are usually required to cause the onset of LCO.
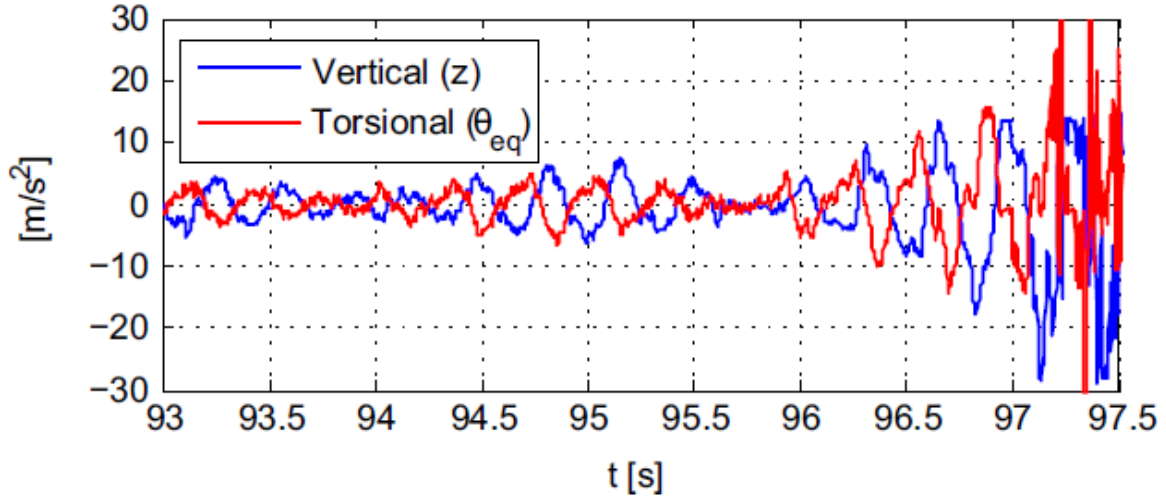
Figure 1.1: Example of acceleration profile caused by flutter [4]
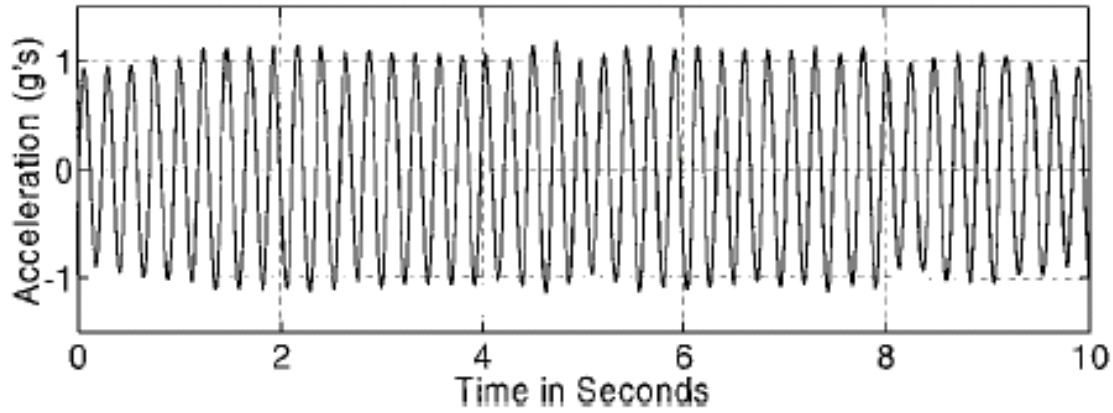
Figure 1.2: Example of acceleration profile caused by LCO [2]

Denegri analyzed wing response data from F-16 flutter testing and noted that LCO are typically encountered at transonic flight conditions [3] . Flight speed has also been shown to be an important factor in the amplitude of the oscillations, with increased velocity leading to a large amplitude. Flutter models have a difficult time predicting the limited amplitude nature of LCO but can determine the oscillation frequency. Exterior loads on the wing (munitions) can significantly alter the onset speed of LCO. However, the wing loading is not hypothesized to be the direct cause of LCO.

The nonspecific cause of LCO is generally considered to be a nonlinear interaction between the structural and aerodynamic forces acting on the flexible wing [2].

3

However, the exact aerodynamic mechanism that drives the oscillations is unknown. There are numerous theories, but the phenomenon known as shock-induced trailing edge separation (SITES) is considered to be the leading candidate by many aeroelastic experts. As the shock slows the flow over the top of an airfoil, separation can occur. The separation can cause the shock along the surface of the airfoil translate, which in turn can alter the forces acting on the structure, propagating the oscillations [5]. When analyzing the aerodynamics during LCO motion, discerning SITES from the other complicated aerodynamics is difficult. To analyze the impact of SITES on the flow field, more simplified experiments were conducted to help isolate the impact.

One simplified experiment that examined a simplified LCO motion was a series of wind tunnel tests conducted by Cunningham on a straked, semispan delta wing [6]. There were two goals of the experiment. First, to characterize the flow field around a simple straked delta wing in the transonic regime. Second, to create a database of aerodynamic loads to validate computational models. To accomplish this, the straked semispan model was oscillated in a wind tunnel to mimic LCO motion. The impact of the motion on the flow field was examined using a number of data collection techniques, including unsteady pressure measurements and accelerometers. A variety of flow speeds were tested, ranging from subsonic to high transonic, that covered the range of velocities where LCO has been shown to be prevalent. The large amount of data collected from the experiment provided an opportunity to validate the results of future computational models. The computational models could then be used to further investigate the flow field of an oscillating semispan.

Computational fluid dynamics (CFD) provide the opportunity to gain more insight into a given aerodynamic problem. In general, CFD is a numerical process to solve a set of equations that describe the physics of an aerodynamic flow. One of the advantages of CFD is that it allows for complete control of the inputs into a problem, ensuring that the model is predicting the exact conditions intended. Also, because of the ability to probe any point in the data field, information can be pulled from the model that is difficult to collect using experiments. These advantages make

4

CFD a powerful tool, especially when paired with experimental results to help explain additional physics that could not be otherwise discerned. The research outlined in this thesis made use of this symbiotic relationship to discover more details regarding the unsteady aerodynamics at play during LCO.

1.2 Research Objectives

The research presented here had two main objectives. The first was to gain a better understanding of the flow dynamics around a straked, highly cambered delta wing in order to investigate the possible aerodynamic causes of the LCO motion. To accomplish this, a computational model based on a series of wind tunnel experiments was developed. The tests investigated the flow field near an oscillating, straked delta wing in an attempt to pinpoint the aerodynamic cause of LCO. A wide variety of data was collected during the experiments, however, a complete visualization of the flow field could provide even more. By creating a computational model of the tests, more detailed information was able to be pulled from the original wind tunnel studies. Comparing the results of the numerical model with the results of the experiment also provided an opportunity to ensure current unsteady computational fluid dynamics models were capable of handling the complex aerodynamics present.

The second objective was to compare the results of the new computational model with solutions from a previous numerical effort. Recently, an Euler model was developed for the Cunningham experiments to assist with predictive modeling capabilities and better understand the onset of LCO in the F-16. The model, created using the ZONA Technologies Euler unsteady solver (ZEUS), utilized a boundary layer coupling scheme for generating efficient computational solutions. However, an Euler solution, even with a boundary layer model included, does not include a potentially significant portion of the viscous effects acting on the flow. To quantify the overall impact of the viscous forces on the amount of shock movement during the forced oscillation, a new computational model was developed to solve the Navier-Stokes (N-S) equations. Using the DoD software Kestrel, solutions to the discretized N-S

equations were collected and compared to the those from the boundary layer coupled Euler equations. The following effort outlines the methods used and results acquired to complete the objectives outlined above.

II. Literature Review

Fully characterizing and understanding the flow field around a straked delta wing is a complex aerodynamic problem with many driving factors. Understanding these factors and how they could contribute to or even drive LCO is pivotal to this work. This chapter will provide an overview of fundamental physics and important research necessary to understanding the intricacies of the task at hand. Section 2.1 covers the basics of classical flutter and LCO while comparing and contrasting the two phenomena. The basic principles of a viscous, three-dimensional flow are covered in Section 2.2. Section 2.3 details numerical methods that have proven effective at accurately modeling separated flow including hybrid turbulence models, time step/grid spacing analysis and adaptive mesh refinement. Section 2.4 outlines a series of unsteady, transonic wind tunnel experiments conducted by Cunningham [7]. The experiments consisted of oscillating a semispan straked delta wing at Mach numbers known to experiences LCO. Section 2.5 examines recent efforts by Hope [8] to validate an efficient Euler solver using the pressure data collected during the Cunningham experiments. The effort tested sensitivity of the flow field to a variety of parameters, including the Mach number, frequency and amplitude of oscillation and the trim angle. These two studies provided the basis for the effort described here, effectively bounding the problem and yielding a copious amount of data to compare new solutions.

2.1 Fluid Structure Interaction Phenomena

One of the goals of the Cunningham experiments was to investigate the flow field around a straked delta wing with the purpose of better understanding the driving forces behind LCO [7]. These nonlinear, periodic oscillations are the result of the coupled reaction of aerodynamic and elastic forces. Section 2.1.1 covers the fundamental physics of classical flutter phenomenon, a more well understood aeroelastic phenomena that is closely related to LCO. Section 2.1.2 then describes LCO in detail.

7
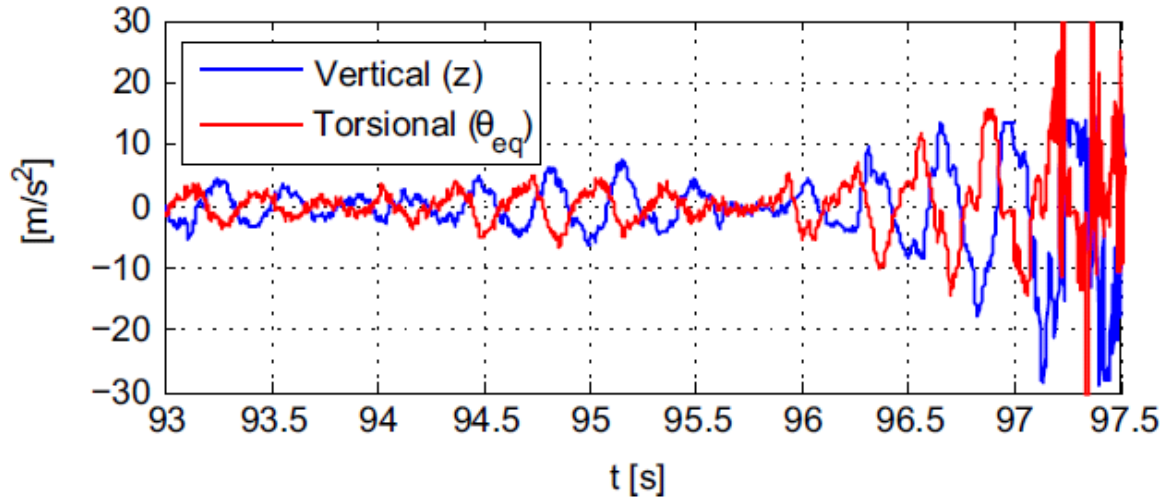
Figure 2.1: Amplitude of acceleration increases with time during flutter [4]

2.1.1 Classical Flutter. As defined by Hodges and Pierce, flutter is a "dynamic instability of a flight vehicle associated with the interaction of aerodynamic, elastic and inertial forces" [1]. Flutter is caused by the aerodynamic forces interacting with the flexible structure, forcing an oscillatory motion. When the vibrations occur at the harmonic frequency of the structure, the amplitude of the motion quickly escalates, leading to a catastrophic failures of the structure. Figure 2.1 shows an example of the quickly increasing amplitude of acceleration during flutter. For aircraft, lifting surface flutter is the most typical form. The flutter phenomenon is not, however, purely limited to wings but can occur in any structure that is subjected to aerodynamic forces, like buildings and bridges. Since flutter can progress so quickly, potentially causing quick structural failure, structures subject to aerodynamic loading are carefully designed to avoid flutter modes. In some cases, when the geometry is particularly complex or the flow field is especially taxing, the only way to ensure flutter will not occur in the intended operating range is with extensive testing. In the early years of flutter modeling, most models were based on classical flutter analysis.

Classical flutter analysis was method used prior to 1980 to determine the flight conditions where flutter first occurs for an aircraft. Instead of solving the equations of motion for the structure, the solution for an airfoil is assumed to resemble simple

8

harmonic motion. The plunge displacement, h, is defined as

$$h(t) = \bar{h} \exp(i\omega t)$$

while the pitching displacement, θ, is

$$\theta(t) = \bar{\theta} \exp(i\omega t)$$

where $\bar{h}$ and $\bar{\theta}$ are the amplitudes of the plunge and pitching displacements, ω is the frequency of the oscillation, and t is time. While the plunging and pitching motions operate at the same frequency, they can be out of phase. To rectify this, $\bar{h}$ is typically represented with a complex number while $\bar{\theta}$ is a real number. The lifting load amplitude, $\bar{L}$ during the oscillations is defined as

$$\bar{L} = -\pi\rho_\infty b^3 \omega^2 \left[l_h(k, M_\infty) \frac{\bar{h}}{b} + l_\theta(k, M_\infty) \bar{theta} \right]$$

where ρ_∞ is the freestream density, b is the airfoil semi-chord and two dimensionless, complex functions that account for plunging and pitching, l_h and l_θ. The amplitude of the pitching moment, $\bar{M}$, has a similar definition

$$\bar{M} = \pi\rho_\infty b^4 \omega^2 \left[m_h(k, M_\infty) \frac{\bar{h}}{b} + m_\theta(k, M_\infty) \bar{theta} \right]$$

where again dimensionless functions for aerodynamic coefficients representing the effects of pitching and plunging are used, m_h and m_θ. The aerodynamic coefficients for pitching and plunging are functions of the reduced frequency and the freestream Mach number. The reduced frequency, k, is defined as

$$k = \frac{b\omega}{U_\infty}$$

where U_∞ is the airspeed, while the Mach number is

$$M_\infty = \frac{U_\infty}{c_\infty}$$

where c_∞ is the freestream speed of sound. The equations above, when partnered with an unsteady aerodynamic solver, can be used in an iterative process to identify the airspeed that flutter occurs for specific values of k and M_∞ [1]. While the classical flutter method can find the stability boundary for the onset of flutter, it is unable to provide any other measure of flutter stability. This is due to its inability to provide the model dampening for an arbitrary flight condition. This limitation lead to further development of flutter analysis methods.

A number of more advanced, unsteady methods were developed to provide more information regarding the onset of flutter, rather than just the stability boundary [1]. The k-method was developed in the 1950's and was a substantial improvement to classical flutter analysis. Many flutter analysis methods included a parameter that simulated the effect of structural dampening. At first, this was generally a set, constant value that was picked based on past analysis to achieve better results. In 1948, Scanlan and Rosenbaum treated the damping coefficients as unknown parameters and solved for the flutter determinant. The result was a method to calculate the stability boundary for flutter as well as establish a margin of stability around the boundary, aiding aircraft designers in the avoidance of flutter. While the k-method is still used by some today, it was determined that it improperly imposes an artificial damping coefficient on the system, causing the frequency and damping parameters to misrepresent the system. To fix this, the $p - k$ method was created. It conducts a p-method analysis, determining the stability boundary from complex eigenvalues, but enforces the that the solution must be simple harmonic motion. The $p - k$ method balances accuracy and with computational speed, making it a preferred method for flutter analysis today. Flutter is generally treated as a linear phenomenon, making the modeling process more straightforward. This is not the case for LCO.
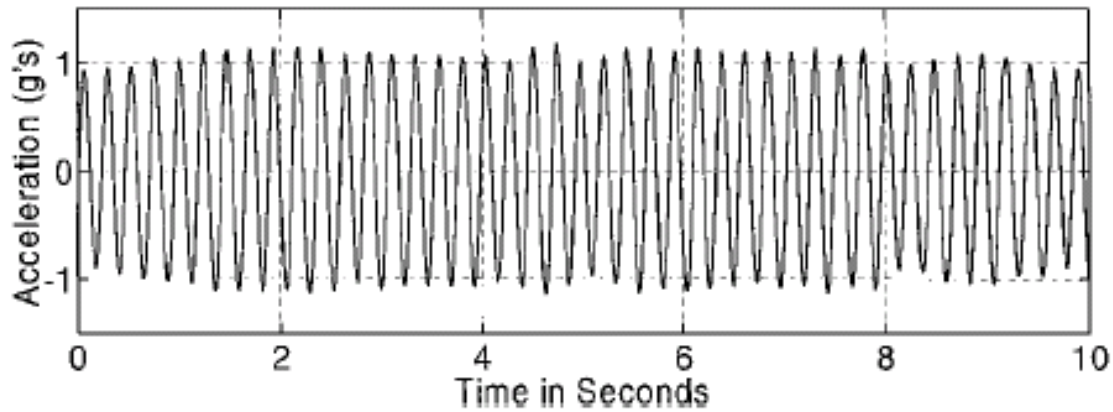
Figure 2.2: The acceleration profile caused by LCO [2]

2.1.2 Limit Cycle Oscillations. Limit cycle oscillations are an aeroelastic phenomenon that results from a nonlinear coupling of aerodynamic and structural forces. Similar to flutter, LCO is a sine-wave like motion with pitching and twisting modes. Unlike flutter however, the amplitude of LCO does not continue to grow over time but instead reaches a peak value for a given air speed [2]. Also, the anti-symmetric oscillatory pattern of the motion repeats over time, indicating LCOs cyclic nature. All of these features can be seen in Figure 2.2, which shows an example acceleration profile caused by LCO. Limit cycle oscillations are also self-sustaining. Meaning, once initiated, the LCO motion will continue until the flight conditions are substantially changed to stop it. High performance aircraft like the F-16 and F-18 have been observed to suffer from LCO at a number of subsonic and transonic flight speeds.

While it is widely accepted that a nonlinear interaction between structural and aerodynamic forces causes LCO, the exact aerodynamic phenomena that propagates LCO is unknown. One of the leading candidates for this aerodynamic "spring" is know as shock-induced trailing edge separation (SITES). Flows in the transonic regime at moderate angles of attack are especially susceptible to the onset of SITES. Work by Cunningham [5] and Meijer [9] showed that onset of SITES can cause a step change in the pitching moment of an airfoil, which can be treated as a nonlinear spring in

11

the system [5]. As the shock moves, either during a maneuver or because of LCO, the pitching moment can fluctuate between higher and lower values, sustaining the motion.

Even though LCO does not cause catastrophic failure like flutter, it does have a number of negative impacts [2]. The most significant problem is that LCO causes a strong lateral motion of the fuselage. As the wings oscillate in an anti-symmetric fashion, the force is translated to the fuselage as a powerful side-to-side motion, creating a difficult operating environment for the flight crew. Another problem presented by LCO is that it can possibly damage munitions on the hardpoints at the wingtips if the munitions are exposed to oscillations for a significant period of time. Finally, while the amplitude of the oscillations is not generally powerful enough to cause structural failure, LCO does increase the stress on a structure. The increased loading can cause additional fatigue to the wing, requiring additional maintenance and reducing mission availability. All of these negative impacts make LCO a very problematic aeroelastic phenomenon and something that must be avoided during normal operation of an aircraft. Predicting the various combinations of operational parameters that can cause LCO becomes an important task.

The onset speed for LCO is, like the onset speed for flutter, dependent on a number of flow parameters as well as the combination of munitions being carried [3]. Because of the complexity of the aerodynamic and structural interactions, developing an analytic solution to the equations of motion that govern LCO is impossible. Instead, because of their close relationship, flutter models can be used to predict the onset speed of LCO for straight and level flight relatively well [2]. However, the flutter models are unable to predict the onset of LCO for normal operating conditions of the F-16. Because of this, extensive flight testing is required to identify the safe flight envelopes for particular combinations of munitions. Since each new combination of munitions must be tested, this process can be very expensive.

2.2 *Viscous Flow Behavior*

Many of the test cases examined by Cunningham exhibited a significant amount of viscous flow effects through out the oscillatory maneuvers. This included massively separated flows, resulting in turbulent eddies forming near the model, and multiple shocks forming on the top surface of the straked delta wing. To best model these complicated phenomena, a basic understanding of the underlying physics is necessary. Section 2.2.1 covers the development and characteristics of turbulent flow. Section 2.2.2 explains the details behind a shock causing a flow to separate on the surface of a wing and how that could lead to LCO.

2.2.1 Turbulent Flow.   Turbulence, as defined by Pope (pg 3, [10]), are unsteady, seemingly random motion aerodynamic flows dominated by vortical structures. Turbulence is an instability in the aerodynamic flow that causes the laminar flow to breakdown and become chaotic. A laminar flow progresses to a turbulent one through a process known as transition. Transition occurs as infinitesimal spatial disturbances coalesce into a completely turbulent flow [11]. Flows usually transition when either influenced by an outside instability or the Reynolds number reaches a critical value. Turbulence has a significant impact on a variety flow parameters including increased drag and heat transfer. Turbulent flows possess multiple length and time scales, making their complex nature difficult to describe.

The vortical structures of a turbulent flow are nether all the same size nor do they have the same frequency content. The turbulent length and time scales are generally broken into three categories: integral scale, Taylor microscales and Kolmogorov scales (pg 195, [10]). Integral scales are the largest of the three and are typically on the same order of magnitude as the geometry of the flow. The Kolmogorov scales are the smallest scales in the turbulent flow and are limited by viscous effects in the boundary layer. Taylor miscroscales lie in between the integral and Kolmogorov scales. As shown in Figure 2.3, the additional kinetic energy that is present as a result of the vortical motion is distributed over the three length scales [12]. Most of

13
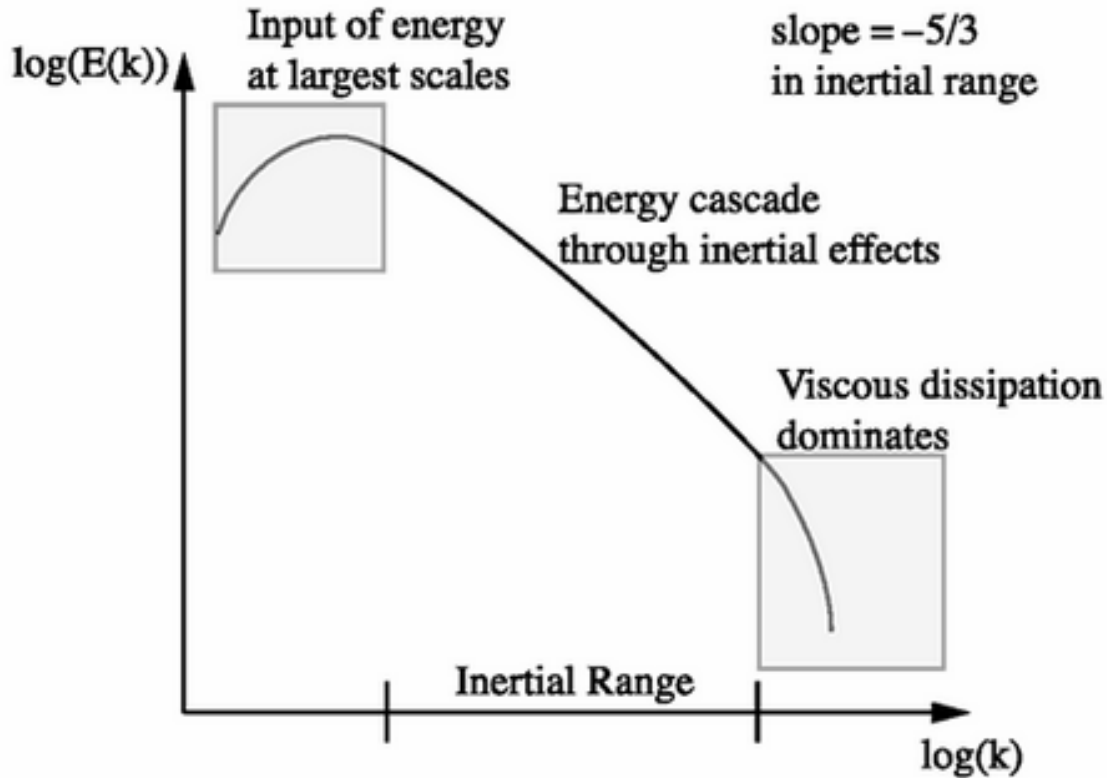
Figure 2.3: Distribution of turbulent kinetic energy over the length scales of turblent flow [12].

the kinetic energy is stored in the integral scale vortices and the amount decreases as the length scales decrease. This represents the turbulent energy cascade, in which energy is passed from larger to smaller scales as the large eddies break down. The breakdown of these turbulent scales is caused by viscous effects that gradually extract energy from the flow, decreasing the local Reynolds number. Since the viscous forces near a surface are more prevalent, the turbulent length scales near a physical boundary tend to be very small. The boundary layer characteristics are important in determining the drag and heat transfer properties of a flow, so, understanding the turbulent flow near a surface is vital.

The transition to turbulence has multiple effects on the boundary layer region of a flow. The vortical structures cause higher gradients in velocity and temperature near the wall which leads to an increase in the drag and heat transfer. Turbulence also

14

thickens the boundary layer, delaying the flow's return to freestream conditions farther from the surface. In order to empirically characterize turbulent boundary layers, a number of wind tunnel experiments have been conducted by many aerodynamics experts. By relating a position and velocity of the flow to the velocity gradient at the wall, a number of empirical estimates were developed. Figure 2.4 shows the relationship between the wall bounded velocity U^+ and the wall-bounded coordinate y^+ [13]. The wall bounded velocity, U^+, is defined as:

$$U^+ = \frac{U}{\sqrt{\frac{\tau_w}{\rho}}}$$

where U is flow velocity, τ_w is the shear stress at the surface, and ρ is the fluid density. The wall coordinate distance from the wall, y^+, is defined as:

$$y^+ = \frac{y\sqrt{\frac{\tau_w}{\rho}}}{\nu}$$

where y is the standard distance from the wall and ν is the kinematic viscosity. All four defined regions in a turbulent boundary layer are governed by different empirical relationships. From a modeling perspective, the most important of these relationships is in the viscous sub-layer, the region right next to the surface. There, U^+ can be assumed to equal y^+. This estimation is utilized by many turbulent models to extrapolate flow behavior infinitesimal close to the wall since measurements in this region are extremely difficult. The requirement for flow information right next to wall drives the need for fine grid spacing at the wall.

2.2.2 Shock Induced Trailing Edge Separation. Separation is a viscous phenomenon that is caused by a fluid being influenced by an adverse pressure gradient, causing the velocity of a portion of the flow to become zero or negative value (pg 10, [11]). An adverse pressure gradient is a change in pressure along a surface that opposes the bulk motion of the fluid. When a flow separates, vortical structures are

15
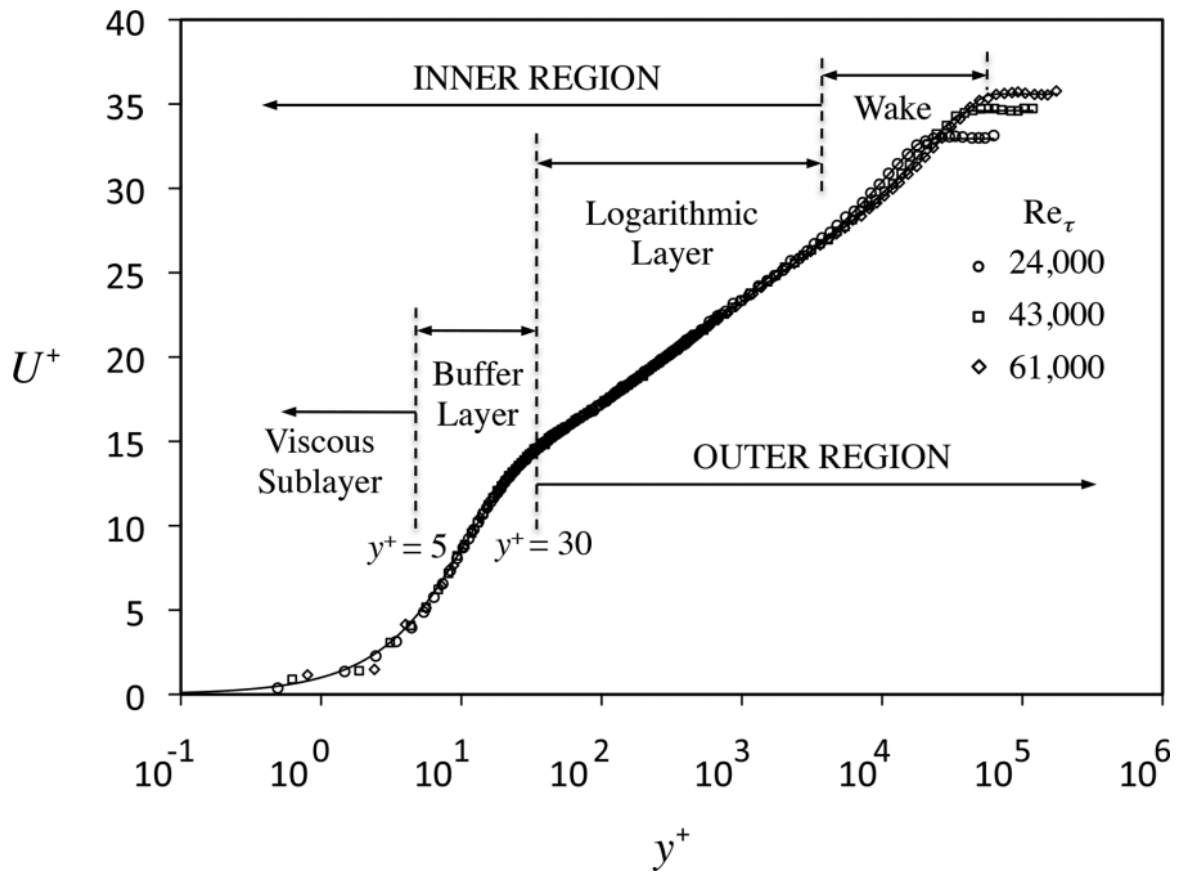
Figure 2.4: Wall coordinates y^+ and U^+ their relationship in turbulent boundary layer [13]

ejected downstream creating a primarily turbulent region in flow. The likelihood and severity of separation is influenced by a large number of flow parameters including geometry, Reynolds number, and angle of attack. The presence of turbulence also influences flow separation, with the former delaying separation when compared to a laminar flow because of the increased kinetic energy. Flow features, like shocks, can also impact when and where a flow will separate.

High performance airfoil shapes can experience separation at different operating conditions. Once the freestream Mach number reaches a certain value, a shock can appear on the top and bottom surface of the wing. The shock is caused by the airfoil accelerating the local airspeed to a value over Mach 1.0. As the flow decelerates approaching the trailing edge of the airfoil, a normal shock develops, quickly pulling energy from the flow. If the shock is strong enough, as shown in Figure 2.5, it can cause the flow to separate. This phenomenon is known as shock induced trailing edge separation (SITES). The flow on the top surface is more likely to separate due to the presence of an adverse pressure gradient and the normal shock is stronger on the top surface. SITES has been observed on many different wing shapes, including the straked delta wing model [7]. In fact, SITES is one of the proposed driving mechanisms behind LCO. The oscillations could cause a shock to change positions on the top of a airfoil, potentially changing the point of separation. If there is enough shock movement, the forces acting on the wing can be altered enough to force an opposing oscillation. This would then cause the shock to move again, which would force another oscillation. This action would continue until the flight conditions were changed. Cunningham [5] and Meijer [14] have observed during experiments and shown with an empirical LCO prediction technique the importance of SITES in terms of propagating LCO.
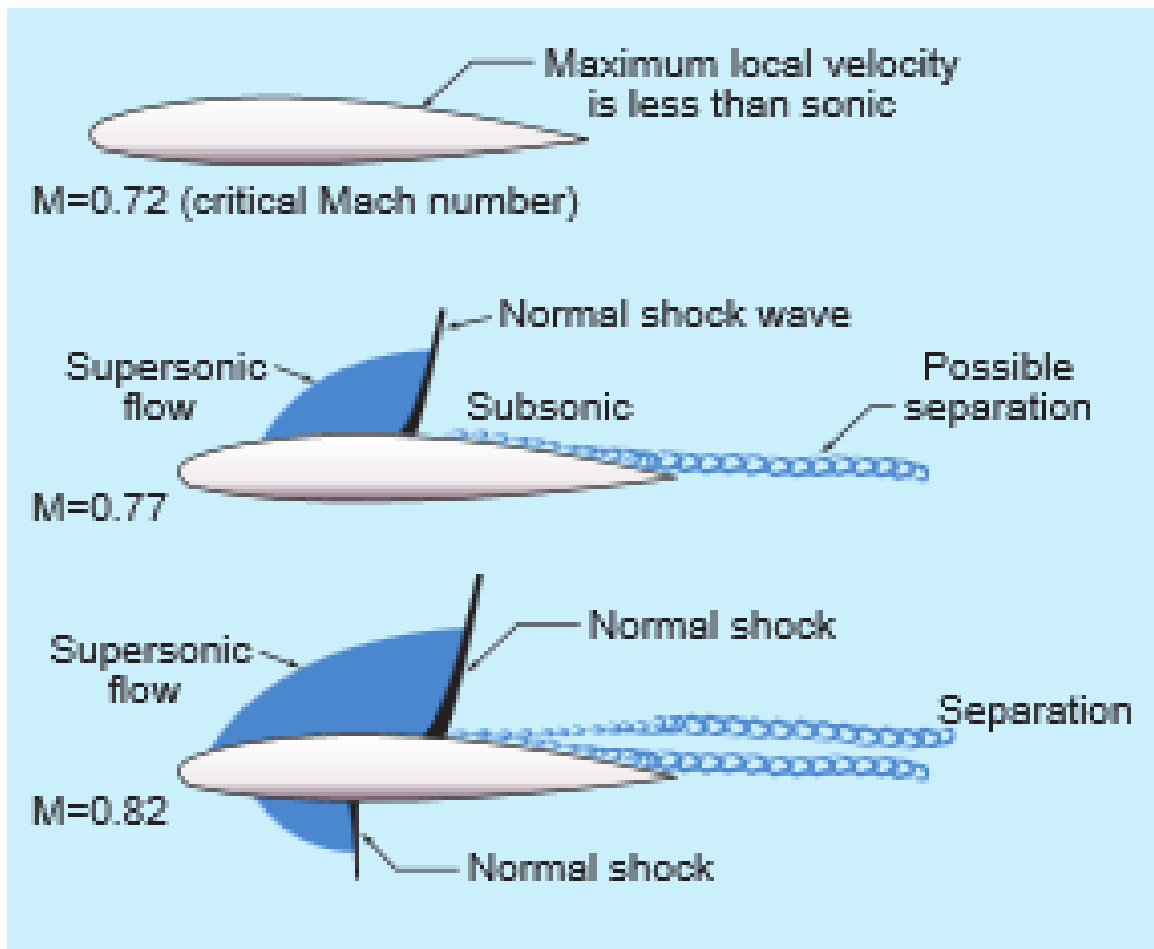
Figure 2.5: Separation can occur behind a shock, as the flow progresses towards the
trailing edge [15]

2.3 Modeling Unsteady, Separated Flows with the Navier-Stokes Equations

Due to the unsteady, separated nature of the flows examined in the Cunningham experiment, special considerations must be taken to ensure an accurate numerical solution is produced. Section 2.2.1 outlines common hybrid turbulence models and their impact on modeling separated flows. Section 2.3.2 summarizes techniques used to find the optimal time step and grid size for a unsteady flow problem. Section 2.3.3 discuses the basics of adaptive mesh refinement (AMR) and its application to unsteady problems with evolving flow features.

2.3.1 Hybrid Turbulence Models.   Hybrid turbulence models blend the computational benefit of using Reynolds-Averaged Navier-Stokes (RANS) models to compute the boundary layer behavior on a surface and the higher fidelity of Large Eddy Simulations (LES) in separated regions. One such hybrid turbulence model is the Improved, Delayed, Detached Eddy Simulation (IDDES) model [16]. This refined version of the Delayed, Detached Eddy Simulation (DDES) [17], which in turn was developed from the original Detached Eddy Simulation (DES).

The original DES turbulence model was designed for use in high Reynolds number flows that were unable to use LES because of the high computation cost [17]. LES is a turbulence modeling method in which the smallest scales of turbulence motion are modeled, while the larger scales are solved for directly. Since most of the turbulence in the computational domain is being solved directly, there is significant grid refinement requirements when applying LES [18]. The large number of cells leads to significant computational requirements to capture a solution for a given flow. The required mesh refinement increases as the Reynolds numbers increases, leading to very high computation costs for high Reynolds numbers problems. DES approaches to problem in a similar manner as LES but only solves for the turbulent motion in regions of large scale turbulence and uses RANS models in areas where small eddies dominate the flow. Typically, only regions of separated flow, where the turbulent eddies are the largest, are solved for directly; all the other length scales are modeled. Increasing the amount of modeling for a given solution decreases the fidelity but also decreases the grid refinement and computation time required, allowing for application to a wider range of problems.

A more advanced version of DES, DDES, was developed following a reported trend of DES severely under predicting the eddy viscosity in some regions of the flow. This numerical phenomenon, termed modeled-stress depletion (MSD), occurs when the switching function prematurely "turns on" the LES solver in the upper part of the boundary layer, where the turbulent length scales are still small compared to the grid resolution [17]. Since the eddies are too small to be accurately calculated,

19

a large percentage of the turbulent viscosity in the region vanishes. This can lead to problems like premature flow separation in the solution. MSD typically occurs when a grid is gradually refined while attempting to reach grid convergence or when a boundary layer thickens and nears separation. For this reason, MSD was observed to be geometry and flow condition dependent. To combat MSD, the DDES model was created.

In an attempt to reduce or eliminate the prevalence of MSD, Spalart made multiple fundamental changes to the DES model [17]. Many of these changes were adapted from work published by Menter, who also sought to remedy the MSD problem. Three variables from the original DES model were redefined for the DDES model. The ratio of the model length scale over the distance from the surface, r_d, was altered to be more universally applicable to any model that solves for the eddy viscosity:

$$r_d = \frac{\nu_t + \nu}{\sqrt{U_{i,j}U_{i,j}}\kappa^2 d^2}$$

where ν_t is the turbulent viscosity, ν is the kinematic viscosity, $U_{i,j}$ are the velocity gradients, κ is the Karman constant and d is the distance from the nearest surface. The LES switching function, f_d, was refined to better match desired shape in the boundary layer with the redefined r_d. The factor 8 and exponent 3 were selected based on testing DDES over a flat plate with the intention of mimicking the results produced by the Spalart-Allmaras (S-A) model. The new switching function:

$$f_d = 1 - \tanh\left([8r_d]^3\right)$$

The DES length scale, $\tilde{d}$, was redefined in such a way that the changed physical basis of the function changed. In the DES model, $\tilde{d}$ only depended on the grid spacing. With DDES, $\tilde{d}$ now depends on the eddy viscosity field in the region, preventing MSD:

$$\tilde{d} = d - f_d \max\left(0, d - C_{DES}\Delta\right)$$

20

where C_{DES} is the fundamental empirical constant for DES and Δ is the local grid spacing. The new definitions of the three parameters above were able to elminate MSD for a wide variety of geometries [17]. A side-effect of the more robust $\tilde{d}$ expression is the switch from wall modeling to LES happens more quickly, which is a more accurate depiction of actual flow.

More recently, additional improvements were made to the DDES model to further improve its accuracy. The IDDES model was developed to blend the Hybrid-RANS concept with another type of turbulence model, Wall-Modeled Large Eddy Simulation (WMLES). This new model was developed to better capture turbulence content when the flow is not highly separated, such as free stream turbulence, without significant user intervention [16]. By blending DDES with WMLES, a more complete and generally applicable model is created. However, this blending is also where an additional problem arose. There was an inherit error when attempting to blend RANS models to LES solutions at the edges of boundary layers. In many geometries, the blending of the RANS model and LES solution led to a mismatch, with both techniques producing differing intercepts. This error can cause up to a 20 percent under-prediction in the skin-friction coefficient, an important parameter for drag calculations [16]. In order to fix the mismatch between models, the blending functions and empirical formulations for DDES had to be altered.

To blend DDES and WMLES appropriately, three computational regions needed to be considered. First, the subgrid scale was formulated to handle turbulence smaller than the WMLES branch could solve for directly. The subgrid scale, Δ_{ss} is:

$$\Delta_{ss} = \min \left\{ \max \left[C_w d_w, C_w h_{max}, h_{wn} \right], h_{max} \right\}$$

where d_w is the distance to the wall, h_{max} is the maximum local grid spacing, h_{wn} is the grid step in the wall-normal direction and C_w is an empirical constant [16]. The constant was tuned using the Smagorinsky subgrid scale model. In order to be

21

applicable to a variety of RANS models, the DDES length scale, l_{DDES}, was redefined:

$$l_{DDES} = l_{RANS} - f_d \max \{0, (l_{RANS} - l_{LES})\}$$

where l_{RANS} is the RANS model length scale and l_{LES} is the LES length scale. The RANS length scale is defined by the length scale of the RANS model selected. The LES length scale is defined as:

$$l_{LES} = C_{DES} \Psi \Delta$$

where Ψ is a term for low Reynolds correction, if required. Finally, the WMLES length scale I_{WMLES}, used for seamless coupling of RANS and LES approaches, is defined as:

$$l_{WMLES} = f_B (1 + f_e) l_{RANS} + (1 - f_B) l_{LES}$$

where f_B is the empirical blending function and f_e is the elevating function. The empirical blending function quickens the transition between RANS and LES. The function varies from zero in RANS mode to one in LES mode. It is defined as:

$$f_B = \min \left\{ 2 \exp \left(-9 \left(0.25 - d_w/h_{max} \right)^2 \right), 1.0 \right\}$$

The elevating function is also based on empirical data and is critical in solving the log-layer mismatch problem. The function is designed to prevent the reduction of Reynolds stresses in the RANS model, a large factor in the log-layer mismatch. The elevating function is defined as:

$$f_e = \max \left\{ (f_{e1} - 1), 0 \right\} \Psi f_{e2}$$

where f_{e1} is a predefined (based on the grid, not the solution) elevating device and f_{e2} is a solution dependent device. With these definitions, IDDES smoothly transitions

between RANS, DDES and WMLES models as required by the grid spacing and flow physics.

When attempting to capture complex, unsteady flow physics, the turbulence model selection becomes one of the most important pieces of the numerical model. Hybrid turbulence models like IDDES and DDES are better suited to more accurately predict the flow than a RANS model alone [19]. More specifically, the hybrid models are capable of modeling significantly more of the temporal content of an unsteady flow than a RANS mode alone. The loss of this content can lead to large errors in a given solution. When modeling wingtip vortices, Liang and Xue observed a 40 percent underprediction in the magnitude of the vorticity when using a RANS model [20]. Menter also showed hybrid turbulence models were much more capable of modeling a separation region downstream of the Ahmed car body problem [21]. In light of this, IDDES will be used to model the turbulence of the flow over the semispan, straked delta wing.

2.3.2 Time Step/Grid Spacing Analysis. When modeling any aerodynamic problem, it is a good practice to perform a grid convergence study to show that the particular numerical solution is no longer dependent on the grid used to find it (pg 513, [19]). This is generally accomplished by having multiple versions of the grid, each with a different number of cells. As the number of cells in the computational domain increases, the solution should begin to converge to a single value. Figure 2.6 shows this type of convergence using the coefficients of lift and drag (C_L and C_D) for a blended wing body from Qin et al. [22]. As the wall spacing, y^+ is decreased, C_L and C_D begun converging to the same value, even with further grid refinement. For steady state problems, this type of analysis is important to help prove that the grid being used is of adequate quality to generate accurate solutions (pg 513, [19]). For unsteady flows, where the local features of the flow field are constantly changing, a grid study is still required but a time step analysis is also pertinent.
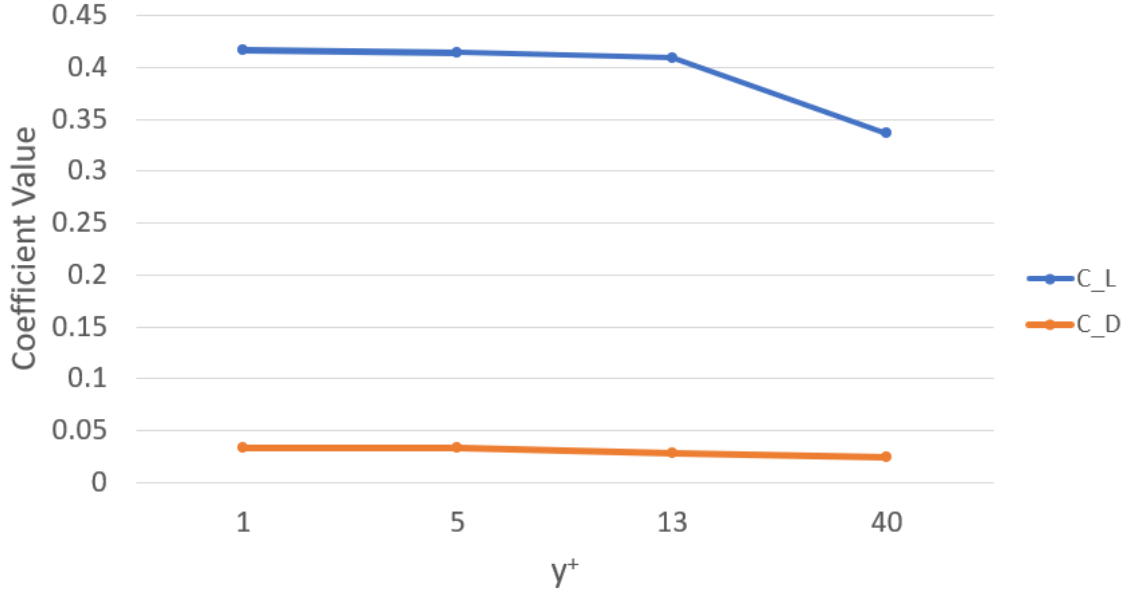
Figure 2.6: An example of a grid convergence study, examing the C_L and C_D with decreasing y^+ from Qin et al. [22]

In CFD, the size of the time step of the simulation is linked to the size of the grid spacing through the Courant-Friedriichs-Lewy (CFL) number. The CFL can be generally defined as

$$CFL = \Delta t \sum_{i=1}^{\infty} \frac{u_{x_i}}{\Delta x_i}$$

where Δt is the model time step, u_{x_i} is the magnitude of the velocity and Δx_i is the grid spacing in a given direction. In general, the smaller the grid spacing, the smaller the time step needs to be to capture gradients in the domain. Because of this linkage, it is important to conduct time step and grid spacing studies together [18], otherwise, it would be possible to reach a grid converged solution but not a time converged solution and vice-versa. Steady-state or RANS models lose this linkage because the final, converged solution no longer depends on the physical time within the model. Time-dependent or unsteady solutions require careful analysis of the flow features that dominate the flow and where they are located to achieve temporal and spatial convergence. From a temporal perspective, the time step must be short enough to render the changing flow features. In terms of frequency content, the time step

24

should be small enough to acquire a meaningful number of samples of the flow field, similar to the Nyquist sampling frequency. Spatially, a grid must not only have small enough grid spacing to capture flow features, but they must be grouped appropriately in regions of high gradients. If both of these are achieved, an accurate solution should be possible.

In order to complete a joint temporal and spatial convergence study, a method was developed by Cummings et al [18]. Just as with the grid study alone, the joint method requires multiple grids of different refinement levels to examine the spatial convergence. Then multiple solutions were generated using each grid at different global time steps, which were generally multiples of some initial time step. A non-dimensional time step of 0.006 to 0.01 has been shown to be adequate for most flows. After running the different grid levels with the multiple time steps, the power spectral density (PSD) of an integrated flow quantity, like C_L and C_D, is calculated. By moving to the frequency domain, it becomes easier to determine what frequency content is dominating the flow. A wavenumber, defined by Cummings et al. as the inverse Strouhal number, is calculated from the PSD and plotted versus the time step size, like in Figure 2.7 [18]. The Strouhal number, St, is a non-dimensional shedding frequency, often defined as:

$$St = \frac{fL}{U}$$

where f is a shedding frequency, L is a reference length and U is the freestream velocity. As the time step is reduced, and if the grid level has adequate refinement in high gradient regions, the plot will converge to the same wavenumber. This wavenumber can be reached at different time steps for different grid levels, meaning either could be used to model the same flow and would achieve similar results. The specific wavenumber the grids converge to would depends on the flow conditions being used since the dominant frequency changes with different flow features. More specifics on determining spatial and temporal convergence are discussed in Chapter 3.
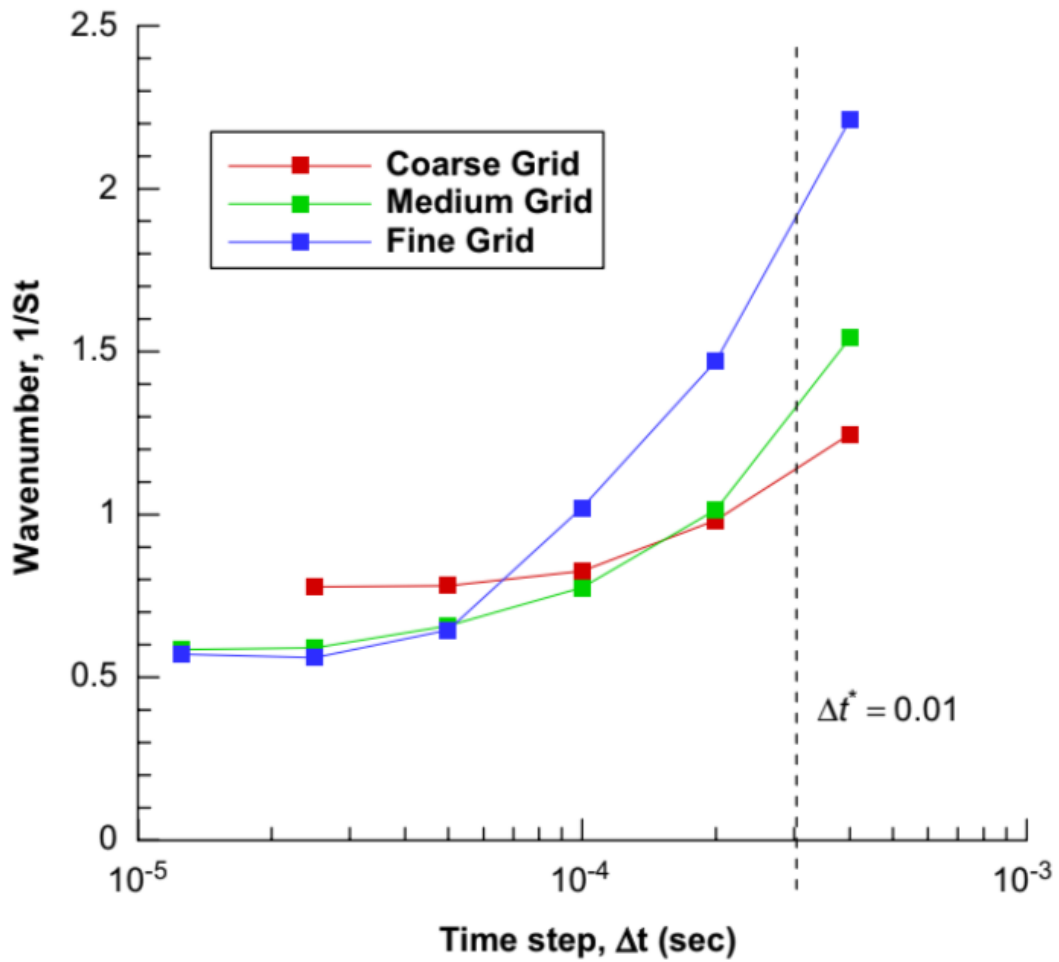
Figure 2.7: An example of joint spatial and temporal convergence study, examing the wavenumber versus the time step for different grid refinement levels [18]

2.3.3 Adaptive Mesh Refinement. When a computational domain is created for a simulation, it is often done so without prior knowledge of the solution. Complex geometries and difficult flow conditions can make surmising the dominant aerodynamic features of a given flow difficult. As a result, creating a grid without knowledge of the solution can introduce an error caused by a poor distribution of cells with respect to these strong gradients [23]. To combat this error, grid adaptation techniques have been developed to either add or reposition grid points based on predetermined parameters of the solution. One of these types of techniques is adaptive mesh refinement (AMR). The power of AMR can is shown in Figure 2.8, which shows the z-component of velocity at varying distances from a wing tip. This data was pulled from numerical solutions that were calculated using 3rd and 5th order numerical schemes as well as AMR. The higher order numerical schemes alone were not adequate to accurately compare to the experimental data, as indicated by the "default" lines on the plot. However, after two cycles of adaptive refinement, the 5th order numerical solution started to approach the experimental data.

In CFD, two types of adaptive methods are typically utilized [23]. "R methods" redistribute the grid points to reduce the error in the solution without increasing the number of cells. These types of methods are typically controlled by a distribution scheme that limits the adaptation to prevent cells from over-stretching. The overall effectiveness of these methods is limited since the number of cells is not increased but it also maintains the computational costs of the original grid. "H methods" are complete mesh refinement where additional cells are added to the computational domain and repositioned to better capture gradients in the flow. These methods can theoretically eliminate essentially all grid related error if allowed to operate uninhibited on the grid. However, this could lead to an explosion in the number of cells, greatly increasing the computational costs of the simulation. One technique to employ H methods is to limit the grid adaptation to an outer Cartesian mesh.

Cartesian meshing is a method of filling a computational domain with cells aligned with a specific Cartesian axis (pg 459, [18]). Cartesian meshes have shown to

27
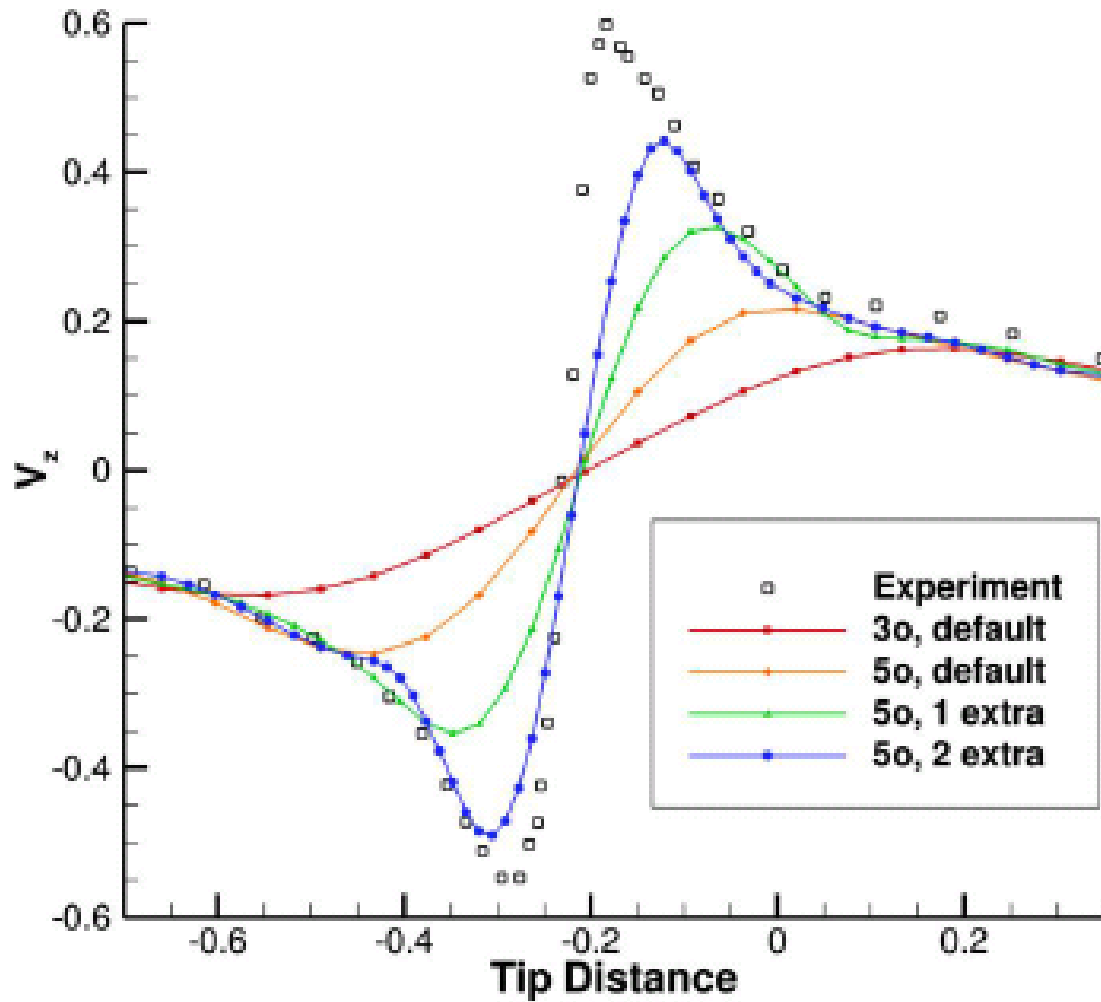
Figure 2.8: The Cartesian mesh solver provides a more accurate solution than a single mesh alone [24]. Plot shows solutions calculated with higher order schemes (3o and 5o) and solutions that utilized AMR
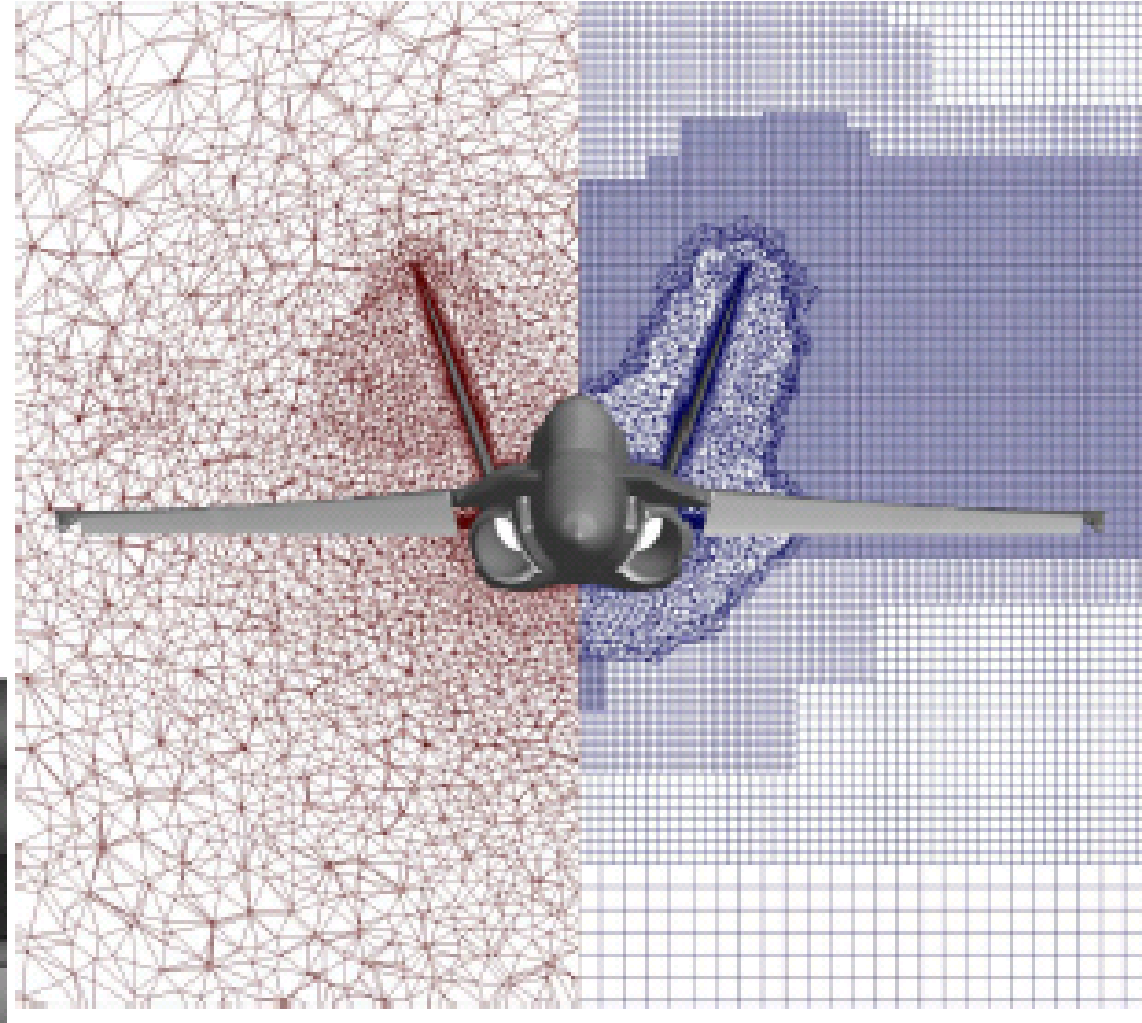
Figure 2.9: A side-by-side comparison showcasing the minimization of cells in the "dual mesh" configuration when compared to traditional unstructured meshes [24]

be relatively easy to implement around complex geometries and can be easily adapted during solving to achieve a more accurate solution. However, Cartesian grids have shown problems when applied directly to the surface of highly curved geometries. To avoid this issue, Cartesian meshes can also be used in conjunction with traditional meshing architectures where a near-body unstructured mesh is couple with an off-body Cartesian mesh. This technique is demonstrated in Figure 2.9 and contrasted with a fully unstructured domain.

Dual mesh refinement methods, like those described above, have many advantages when compared to unrefined domains. First, since structured Cartesian grids are able to implement higher order spatial schemes than unstructured meshes, the Cartesian grid can more efficiently fill a computational domain while achieving the same accuracy [24]. Second, features of the flow field, like shocks and vortical structures, can be enhanced depending on the selected refinement parameter. Lastly, the SamAir solver can lead to converged, time accurate runs in up to 2.5 times fewer iterations than without the dual-mesh simulation. Even though the dual-mesh paradigm increases the number of grid cells, the extreme reduction in convergence generally leads to large savings in computational power. All three of these benefits will be crucial in modeling the complex, unsteady flow around the straked delta wing during oscillatory maneuvers.

2.4   Oscillation of Semispan Straked Delta Wing Experiments

A series of wind tunnel experiments were performed at the Netherlands Aerospace Centre (NLR) in 1993 by Cunningham [6]. The tests consisted of oscillating a semispan straked delta wing at subsonic and transonic flight conditions. The main objectives of the experiment were to characterize the flow field around a simple straked delta wing in the transonic regime and to create a database of aerodynamic loads to validate computational models. Figure 2.10 shows the geometry of the semispan straked delta wing model. The inboard portion of the model was the strake, an aerodynamic body used to generate vortices upstream of the wing. The strake shape was

30

designed to be a simple diamond, which made it more simple to manufacture. The outboard, delta wing section consisted of a highly cambered NACA 64A204 airfoil along the entire span. The wing section had $-3°$ of linear twist, starting at the point the wing met the strake.

The tests were carried out in NLR's 1.6 m by 2.0 m high speed wind tunnel. The closed circuit tunnel was capable of Mach numbers as high as 1.35 and, through variation of the stagnation pressure, a large range of Reynolds numbers [6]. The straked delta wing model was mounted on a shaft which was in turn connected to a turntable embedded in the sidewall of the tunnel. The mounted model is shown in Figure 2.11. The turntable position could be adjusted to set a mean angle of attack for the model. The turntable was acted on by a linear actuator that drove the oscillatory pitching motion used throughout the experiment. The entire model was made of high-grade aluminum to meet the strength requirements while being light enough for the support structure. The airfoil had to be thickened on a small section on the underside of the wing to permit the mounting system to be contained by the model.

A large number of pressure taps, accelerometers and force transducers were used to gather data on the behavior of a flow around a semispan straked delta wing. The pressure taps collected unsteady pressure measurements along the surface of the model. The taps were positioned in chord-wise and span-wise rows primarily along the top surface of the model, as shown by the dashed lines in Figure 2.10. The pressure taps were intentionally grouped near the wingtip to capture the complicated flow features in that region and track any shock migration. Accelerometers and force transducers recorded the unsteady aerodynamic forces during the oscillatory motion. Additionally, the model also stored a host of cables and wires for the instrumentation used during the study.

The straked delta wing model was tested at Mach numbers of 0.225, 0.6, and 0.9 and a constant Reynolds number of 8×10^6. At each speed, data was gathered
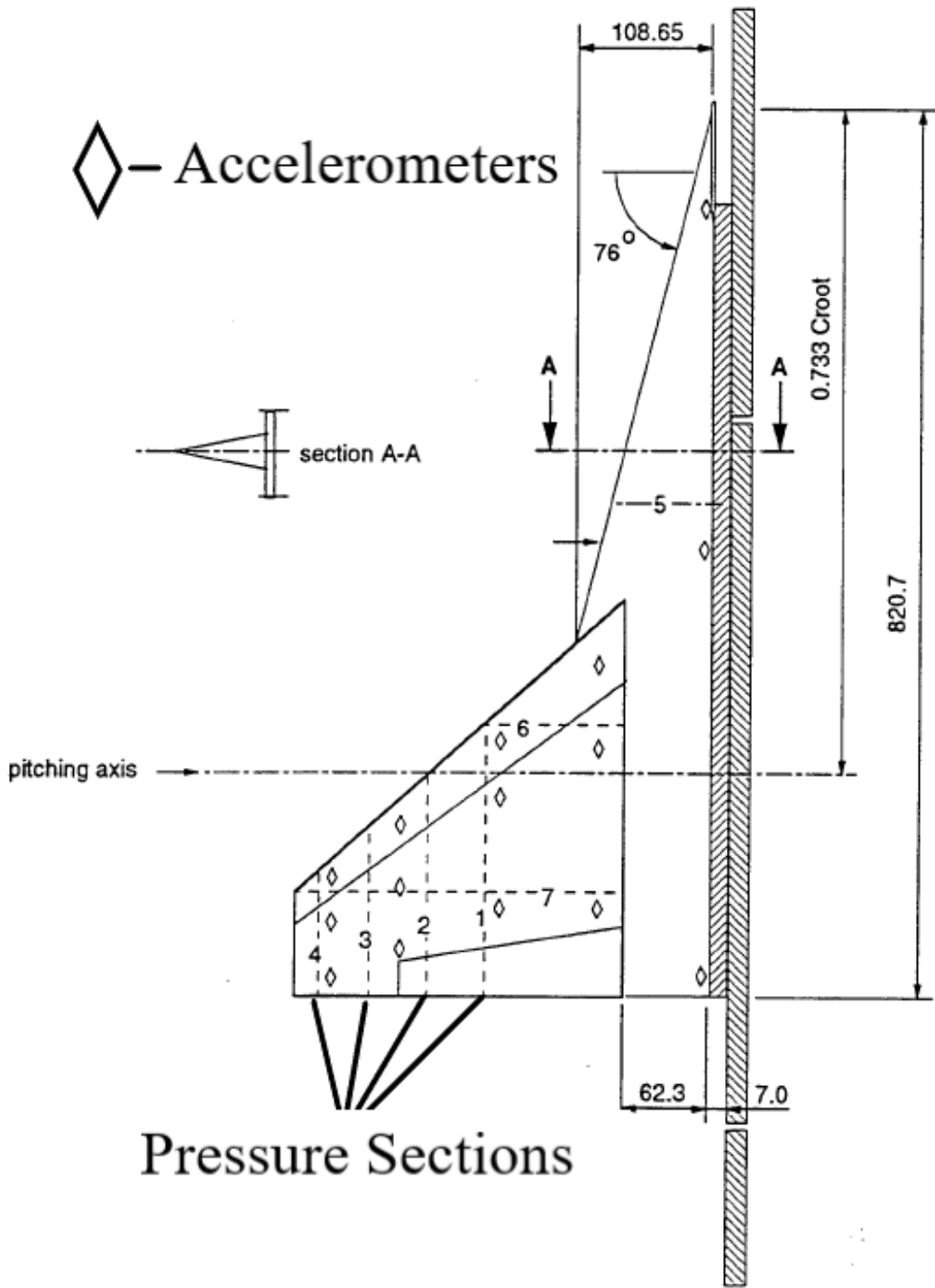
Figure 2.10: Semispan straked delta wing used during Cunningham wind tunnel tests [6]

32
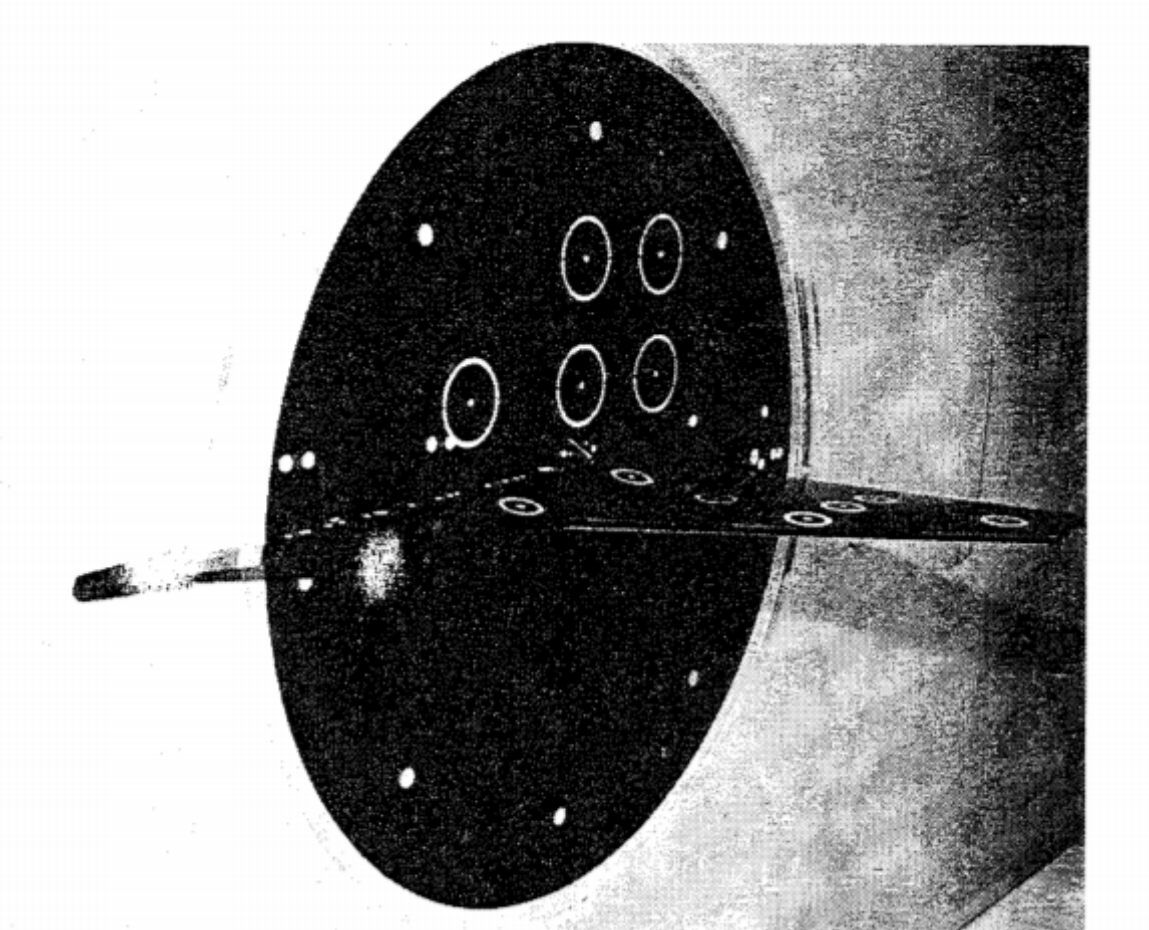
Figure 2.11: Model mounted on turntable in NLR wind tunnel [6]

33

during simple sinusoidal oscillations and during more complicated motions intended to mimic maneuvers in which real aircraft have experienced LCO. The mean angle of attack and starting position for each oscillation was varied from 6° to 48°. The amplitude and frequency of the oscillations was also varied at each starting position, with the frequency ranging from 5.7 to 15.2 Hz while the amplitude falling between 0.5° and 8.0°. All three variables were independently altered to examine the effect each component had on the flow field.

The flow features over the straked semispan at transonic flow conditions were shown to be very dependent on the trim angle [6]. At low trim angles, a two shock system appeared on the top surface, one forward shock and one aft close to the trailing edge. As the trim angle was increased, the forward shock moved toward the trailing edge, merging with the aft shock. At these lower trim angles, a high lift force were recorded at the wingtip, indicating the possible presence of wingtip vortices. At trim angles approaching 10°, the remaining shock on the top surface began to cause separation downstream from its location. As the trim angle was further increased, the flow on the top surface was dominated large vortices and separation. These types of features provide opportunities for qualitative comparison with a N-S model. The recorded C_p values along the surface of the wing provide an avenue for quantitative comparisons to the experiment.

2.5 Predicting Shock Migration with an Euler Solver

Data from the Cunningham wind tunnel experiments was recently used to validate a joint computational fluid dynamics (CFD) and fluid strucuture interaction (FSI) solver. The effort undertaken by Hope [8] centered on demonstrating the predictive capabilities of the ZONA Euler Unsteady Solver or ZEUS, an efficient Euler solver [25]. The high level of computational efficiency demonstrated by Euler-based methods make them favorable candidates for sweeping through many different operating conditions, like during flutter/LCO testing. By showing that Zeus could model

the shock migration observed by Cunningham [7], ZEUS could then be a candidate for modeling flutter/LCO with full structural models.

The computational mesh and finite-element models (FEM) used by ZEUS are internally generated based on main geometry features specified by the user. The fluid and structural meshes are assumed stationary to simplify the relationship between the two, which makes coupling the solutions more straightforward. Due to limitations in the mesh generation capabilities of ZEUS, the model geometry was altered slightly from the original, as seen in Figure 2.12. While the overall span and strake length were maintained, the point where the wing and strake meet was moved 46.35 mm outboard. The fluid solution was calculated using a central difference method which employs the Jameson-Schmidt-Turkel scheme for artificial dissipation and flux reconstruction. While an Euler code, ZEUS has the capability to add viscous effects to the inviscid solution using a boundary layer coupling technique. By breaking the computational domain into an off-body inviscid region and a near-body viscous region, the boundary layer equations can be solved in the thin area near a surface rather than the entire domain. Restricting the size of the viscous region to the boundary layer thickness the complexity of the model is reduced, saving computational effort.

In order to compare results from Zeus to the Cunningham experiments, the location of the shock on the top surface of the outboard wing was tracked while the model was pitched in a sinusoidal motion. These forced rigid body oscillations were used to match the same motion used by Cunningham. The shock location was determined by identifying the location along the chord at which the coefficient of pressure (C_P) was at a minimum, like in Figure 2.13. Large drops in pressure coefficients in the chordwise direction over a wing generally indicate a shock has formed. By tracking the location of minimum C_P throughout the oscillation, the location of the shock can also be determined. The C_P was tracked in the same spanwise locations as the unsteady pressure taps on the Cunningham model. Hope examined the sensitivity of the flow solution to the same parameters as Cunningham, varying the Mach number (0.9 and 0.95), trim location ($4°, 7°$ and $10°$), oscillation

35
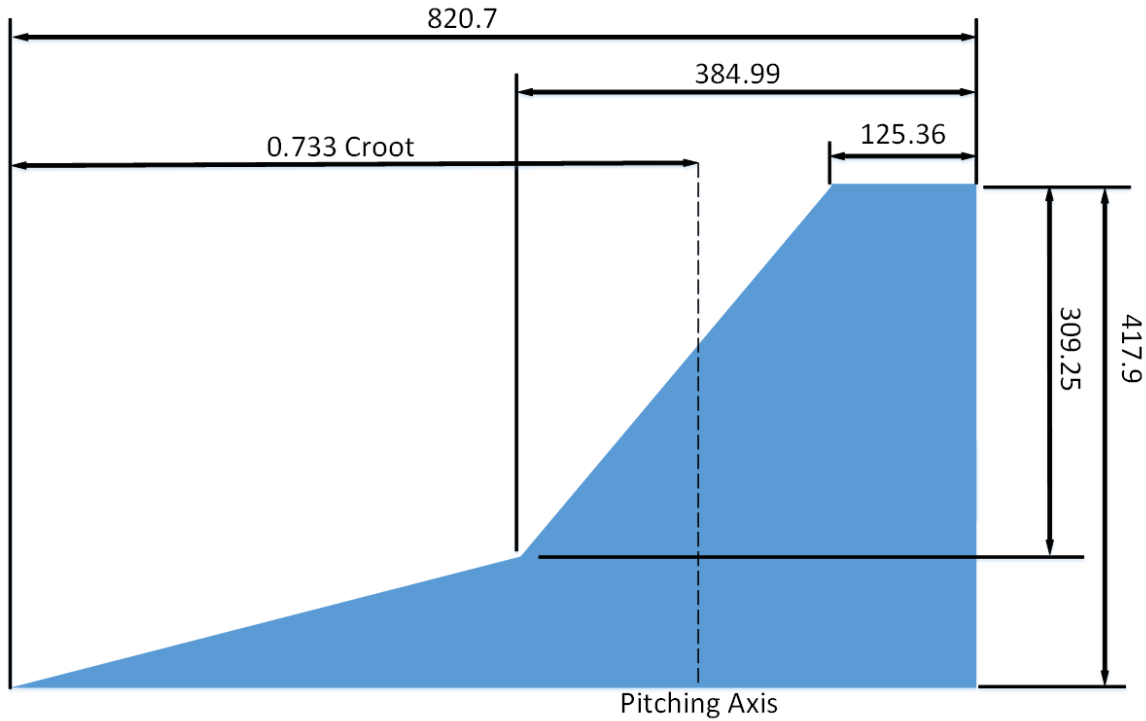
Figure 2.12: Geometry used by Hope in validation effort, measurements in mm. Strake/wing mesh point moved 46.35 mm torwards the wingtip, when compared to the original Cunningham geometry [8]

frequency (5.7 and $7.4Hz$) and oscillation amplitude, A ($2°$ and $4°$). The effect of the boundary layer coupling model was also investigated by solving some repeat conditions as completely inviscid flows.

Hope observed varied effects on the magnitude of the shock migration when different flow and oscillation parameters were altered. At $M = 0.9$, increasing the trim angle and oscillation amplitude showed increased shock migration [8]. In contrast, increasing the same two parameters had either no effect on the shock migration or actually reduced the amount of movement at $M = 0.95$. Similarly, the frequency of the oscillation had little to no impact on the shock location during the oscillation. Finally, the inviscid solution without the coupled boundary layer had two to three times less shock movement than the boundary layer coupled model. While from a qualitative perspective the Euler results seem to follow similar trends as observed by Cunningham, a quantitative comparison was not accomplished.

36
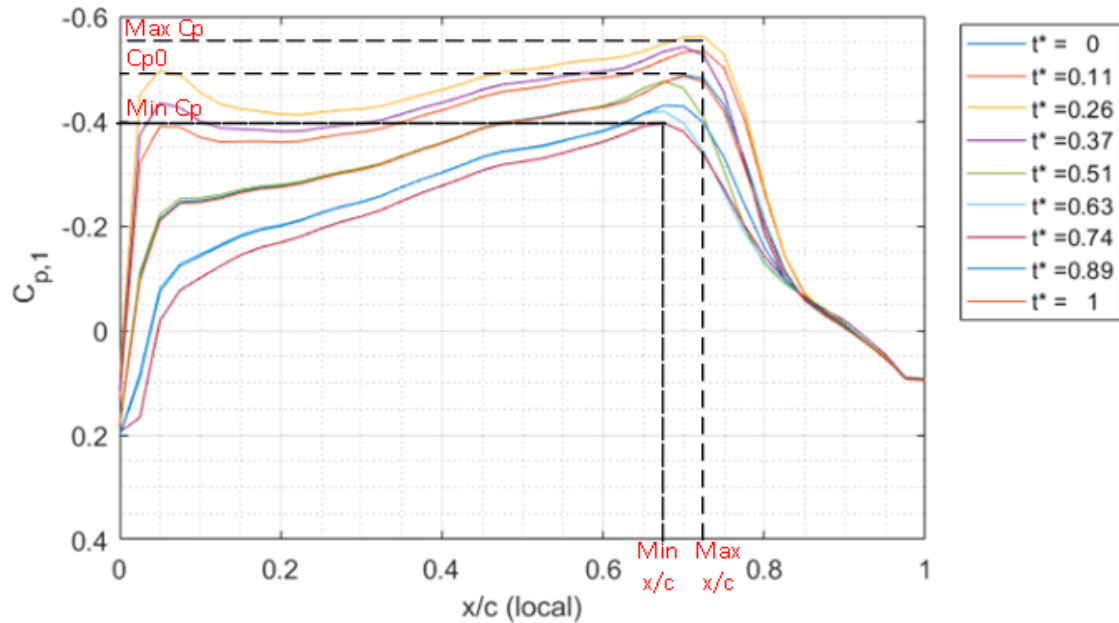
Figure 2.13: Example plot examining the migration of a shock on the top surface of the model. $M = 0.9, f = 5.7Hz$, trim= $4°$, A = $2°$ [8]

Hope was able to compare his results to F-16 flight tests conducted by Tauer [26]. The flight tests showed almost no shock movement during the plunging motion of the F-16 in flight. However, due to the experimental setup, only a small portion of the flow was analyzed near the wingtip, leaving the behavior of the inboard region a mystery. The Euler results provided an important starting point for the N-S solutions, allowing for an even comparison between the two solvers.

2.6 Chapter Summary

In summary, the driving force behind the LCO motion is a relative unknown. One possible cause of LCO is SITES, which can cause shock movement and act as the aerodynamic "spring" that maintains the oscillation. Modeling unsteady, separated flows was shown to require hybrid turbulence models and AMR to achieve accurate results. Unsteady flows require joint spatial and temporal analysis to show convergence for the computational domain. The Cunningham experiments examined the

37

flow features around a straked, delta wing while varying a number of flow parameters and oscillatory maneuvers. Hope modeled the Cunningham experiments using an Euler solver coupled with a boundary layer solver and varied many of the same parameters tested in the wind tunnel. All of this information was incorporated into the research methodology employed during the research.

III. Methodology

Since LCO has been shown to effect multiple high performance aircraft, properly modeling the phenomenon is an important goal. Understanding the specific flow features that appear in transonic flight around highly cambered, thin, delta wings can lead to better knowledge of the drivers of LCO. In order to characterize the flow field around the straked delta wing, a computational model needed to be developed. The model was designed to accurately capture the dominating flow features and predict the movement of the shocks along the top surface of the semispan. This chapter will describe the creation of the computational model as well as the tools used to find an accurate solution. Section 3.1 presents an overview of the CFD software package, Kestrel. This DoD code is the fixed-wing numerical solver owned and maintained by the Computational Research and Engineering Acquisition Tools and Environments (CREATE) Air Vehicles™(AV) team. Several features of Kestrel were utilized including the near-body unstructured solver, the off-body Cartesian solver and Kestrel's ability to prescribe a rigid body motion to a model. Section 3.2 summarizes the steps completed to define the computational domain. This includes replicating the geometry of the model used by Hope and forming the near-body mesh around it as well as the results of the temporal and spatial grid convergence study. The complete test matrix used for the effort is laid out in Section 3.3.

3.1 CREATE-AV Kestrel

The Kestrel program is one of the products born out of a 2008 initiative by the Department of Defense High Performance Computing Modernization Program (HPCMP) to improve the acquisition process through decreased costs, increased performance and shortened timelines [27]. To accomplish this task for fixed-wing aircraft, CREATE AV™sought to assemble a multi-physics, computational environment capable of evolving as the needs of the user base changed. This section describes the main components of the Kestrel software that were utilized for research. Section 3.1.1 provides an overview of the inner workings of the CFD solver. The Kestrel Computa-

39

tional Fluid Dynamics Solver (KCFD), the program's unstructured, near body solver and the off-body Cartesian solver SAMAir are summarized in Section 3.1.2. Finally, the steps taken to force prescribed motion of the near-body mesh within the Cartesian extents is presented in Section 3.1.3.

3.1.1 Program Overview. Kestrel is a modular, multidisciplinary computational modeling environment intended to model the flow field around fixed-wing aircraft and closely related phenomena. Since its inception, Kestrel development has focused on two important themes. The first is improving the acquisition process by providing advanced modeling capabilities to lower costs, increase performance and speed up timelines for new technologies [27]. The second was constructing a software package capable of adapting to new requirements as technology continues to develop and making it accessible to a large user base. To accomplish these goals, the core infrastructure and physics solving components of Kestrel were constructed around a central communication module. The Common Scalable Infrastructure (CSI) connects the different modules of Kestrel together and manages the work flow of the simulation. Figure 3.1 shows a simplified version of this work flow. CSI maintains an event-based architecture and allows for simple testing of new modules without overhauling the entire code. In order to allow for data to be passed between in each module, CSI manages a data "warehouse". The data warehouse facilitates different modules to add certain data and grab required data that has been contributed by a different module. The warehouse construction allows for modules that require different data formats or even different coding languages to seamlessly pass information to one another, with the data warehouse acting as the go between. Kestrel's modular setup also allows it to adapt to ever evolving high performance computing (HPC) requirements and capabilities.

The ever increasing complexity of state-of-the-art CFD codes has pushed many towards utilizing HPCs to provide solutions more quickly. Kestrel was designed with this in mind to efficiently utilize the HPC resources available to DoD users. Kestrel

40
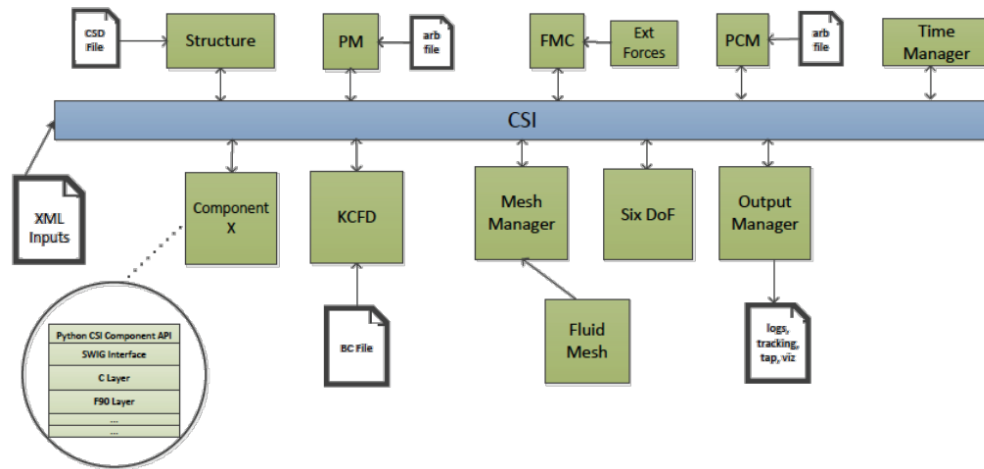
Figure 3.1: CSI connects the many modules of Kestrel together [27]

allows for jobs to be partitioned over individual cores or entire computing nodes. The current communication structure assigns each defined body its own group of processors. Each of these nodes runs its own instance of CSI. This design minimizes the amount of information that must be passed between nodes, decreasing the overhead involved in operating on a HPC. All of these different instances of Kestrel work together to solve the discretized Navier-Stokes equations over the entire computational domain. Since Kestrel is a CREATE-AV™product, it has been integrated with all of the DoD-HPC systems. The ever increasing size of computational meshes used for numerical modeling has lead to a reliance on HPC systems to complete simulations in a reasonable amount of time. Kestrel's integration with DoD HPC systems allows for it to be used to model complex, large geometries without sacrificing numerical accuracy. A variety solver components present within Kestrel also help maintain numerical accuracy for a wide variety of problem types.

3.1.2 Numerical Solver Components. As stated in Section 3.1.1, there are two numerical solver components present in Kestrel. The first is the primary numerical solver, KCFD. This unstructured, finite-volume, numerical solver is capable of solving the discretized N-S equations with various turbulence models. The KCFD solver was

41

developed from the Air Vehicle Unstructured Solver (AVUS) which was a component of the Air Force Research Laboratory (AFRL) code Cobalt60. The numerical schemes that existed in AVUS were heavily overhauled to arrive at the KCFD solver. The viscous and inviscid fluxes can be solved with different numerical schemes, like the Harten, Lax, van Leer and Eifeldt (HLLE) method. Seven different flux limiters are available in KCFD, with the in-house formulated "Kestrel" limiter as the default. While KCFD is the primary flow solver for Kestrel, it also acts as the solver for any near-body mesh used in conjunction with the Cartesian, off-body grid.

SAMAir is Kestrel's off-body, higher-order Cartesian solver that can be used in partnership with KCFD. SAMAir was originally developed from SAMCart, the off-body solver from Helios, the CREATE-AV rotary aircraft CFD software [27]. SAM-Cart was then augmented with the SAMRAI Cartesian mesh library from Lawrence Livermore National Laboratory and renamed SAMAir to reflect this integration. SAMAir is capable of higher order spatial solutions, up to 5th order using a weighted, essentially non-oscillatory (WENO) scheme. This means an accurate solution can be achieved in the off-body mesh while using fewer cells than required in the near-body mesh. The SAMAir solver automatically utilizes adaptive mesh refinement on the Cartesian portion of the mesh. This is done initially to match the inner boundary of the Cartesian mesh to the outer boundary of the near body mesh and prepare the Cartesian mesh for the simulation. After the initial refinement is complete, the numerical solution can then be checked to see if any cells meet an established refinement criterion. Different refinement criteria can be selected to improve the solution quality near different features of a flow, this includes a shock sensor and the Q-Criterion, which focuses on regions of high vorticity. The partnering of the AMR capability with the higher order numerical methods available to the Cartesian solver make it a powerful tool for generating accurate but computationally efficient numerical solutions. While the two solver components within Kestrel have a variety of unique features and settings, they also share a number of important parameters during a simulation.

Table 3.1: Values used for important numerical solver settings within Kestrel

Global/Reference	
Mach Number	0.90
Reynolds Number	1.55×10^7
Static Temperature [K]	264.55
Global Time-step [s]	1.4×10^{-5}
Reference Length [m]	0.8207
Newton Sub-iterations	5
Turbulence Model	IDDES with S-A
KCFD	
Inviscid Fluxes	HLLE++
Viscous Fluxes	LDD+
Spatial/Temporal Accuracy	$2^{nd}/2^{nd}$
Wall Accuracy	1st
Advective Temporal Damping	0.1
SAMAir	
Inviscid Fluxes	HLLE++
Convective Fluxes	VanLeer
Spatial and Temporal Accuracy	3rd and 2nd
Advective Temporal Damping	0.1
AMR Refinement Parameter	Raw Shock Sensor
Refinement Frequency	200 Iterations

Every Kestrel simulation uses a number of global setting regardless of which numerical solver component is being used. For time accurate simulations, a global time step is set before the start of each simulation and used throughout the entire flow field. Free-stream reference conditions are also set at the onset of each new run. The reference conditions are calculated based on three user inputs that provide enough information for the other parameters to be calculated. There are a number of combinations of parameters that can be selected by the user depending on what information the user has available. Another important piece of the numerical solution that is universal across the simulation is the turbulence model. The user can select between two different RANS models (Spalart-Allmaras or Menter Shear Stress Transport) and also a number of settings that can be useful for certain flow types, such as a curvature correction. Also, the IDDES model can be turned on to provide unsteady turbulent information as well. The values used for these global settings, as

43

well as the settings for KCFD and SAMAir, are in Table 3.1. All of these options and values are important pieces to the numerical model, just like the prescribed motion of the model.

3.1.3 Prescribed Motion of Body.   Kestrel is capable of forcing several different prescribed motions on defined bodies during a simulation. These motions can be used to mimic many real world situations including munition release and advanced aircraft maneuvers. The available motions include a step (quick change in parameter), a ramp (gradual change in parameter over time), a pulse (a Gaussian profile over time) and a sinusoidal motion. Each of these motions is capable of changing the both the angle of attack and translate a body within the computational region. Because of its oscillatory nature, the sinusoidal motion was used for the simulations to change the angle of attack over time. The sinusoidal motion position, S, is dictated by the equation:

$$S\left(t\right) = \tilde{s}\left(\hat{t}\right)\cos\left[2\pi\left(\beta_f\hat{t}^{1+\lambda_f} + f_1\hat{t} + \frac{\Phi}{360}\right)\right]$$

where:

$$\tilde{s}\left(\hat{t}\right) = \beta_a\hat{t}^{1+\lambda_a}, \ \beta_a = \frac{a_2 - a_1}{(t_{max} - t_0)^{\lambda_a}}, \ \hat{t} = (t - t_0), \ \beta_f = \frac{f_2 - f_1}{(t_{max} - t_0)^{\lambda_f}}$$

In the previous equations, t is the actual time, t_{max} is the maximum time of the maneuver, t_0 is the start of the maneuver, a_1 and f_1 are the initial amplitude and frequency, a_2 and f_2 are the final amplitude and frequency, λ_f and λ_a are the frequency and amplitude shift parameters and Φ is the phase shift in degrees. For all of the simulations with motion, the start time was set 100 iterations ($1.4\mathrm{x}10^{-3}$ seconds) after the start of the simulation. There was no shift in the frequency, amplitude or phase of the oscillation during the simulations so these parameters were set to zero. The oscillation amplitude and frequency were dependent on the simulation.

44

3.2 *Computational Model*

The goal of the computational model is to accurately solve the N-S equations to examine the flow field around a straked delta wing. The computational model was created based on the geometry of the model used by Cunningham and Hope. Section 3.2.1 discusses the development of the computational model, including the model geometry, the near-body and off-body meshes and construction of the data collection files. Spatial and temporal convergence were demonstrated to show the solution is independent of the grid spacing and time step size and the results are shown in Section 3.2.2. Finally, Section 3.2.3 outlines the uncertainty analysis that was conducted to determine the amount of error introduced by the computational model.

3.2.1 Computational Model Design. To create the computational model, the model geometry had to be created using SolidWorks®2017. Figure 3.2 shows the geometry of the SolidWorks model that was used to create the near-body mesh. The model was based on the geometry used by Hope in his development of an Euler model [8]. This was done for two reasons. The first is there was not adequate information to perfectly match the geometry used in the Cunningham experiments. The engineering drawings that were provided in the literature do not have a number of measurements needed to create a model. The second is that by using the same geometry as Hope, a clear comparison could be drawn between the N-S and Euler models and also any errors introduced by the different geometry would be shared between both numerical models. The outboard wing section of the model is a NACA 64A204, a highly cambered airfoil shape that is used on the F-16. The inboard section of the model is a diamond shape that was linearly extrapolated to the wing section. Like the Hope model, the point at which the strake and wing sections meet was moved 46.35 mm outboard. The one difference between the geometry used for the N-S model when compared to the Euler model is that small fillets, with a radius of 0.1mm, were added to the sharp model edges. The sharp edges along the leading edge of the strake and the entire trailing edge of the model, without the fillets, caused problems when

45

attempting to extrude the near-body mesh. The small size of the fillets should have little to no effect on the flow field.
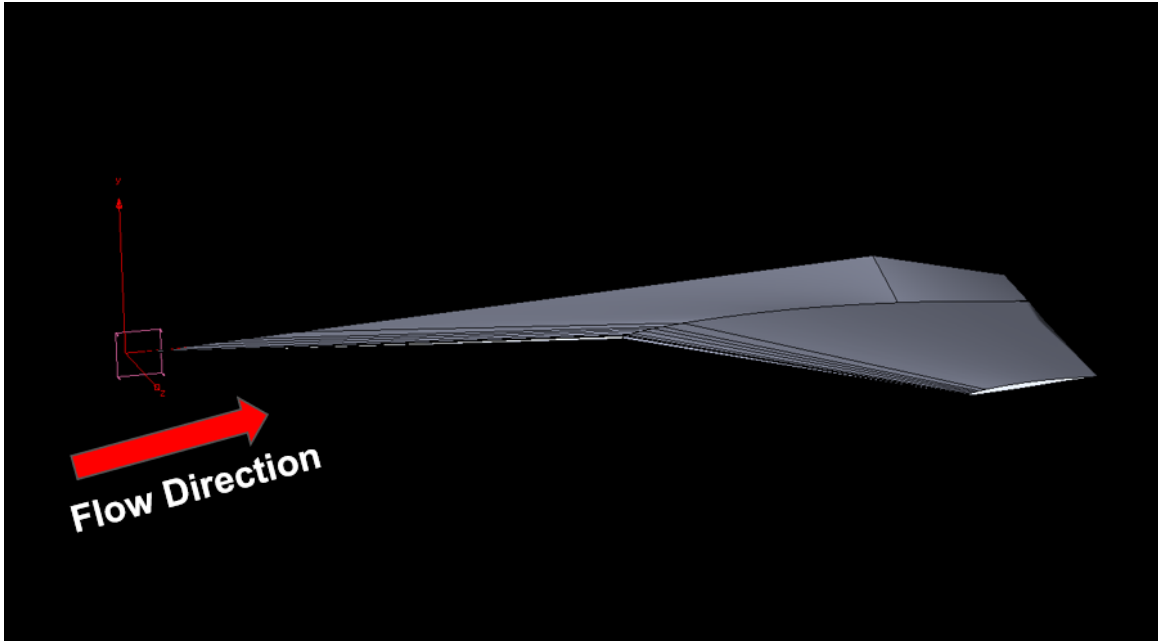
Figure 3.2: Model generated to match the Hope straked, delta wing geometry, imported into Pointwise

Pointwise®v18.1 was used to create the near-body mesh which wrapped around the SolidWorks model. The first step in the process was to form a surface mesh on the straked delta wing. To test for spatial convergence, three different surface meshes were created with varying levels of grid spacing. Spatial and temporal convergence analysis of the computational model is discussed in Section 3.2.2, where more details are provided on the creation of the different grid refinement levels. Next, the surface mesh was extruded from the model. The initial extrusion spacing (Δy) was calculated to establish a wall spacing (y^+) value around 1.0. The equation used for Δy was:

$$\Delta y = \frac{y^+ \mu}{\rho U_\tau}$$

where μ is the dynamic viscosity, ρ is the density and U_τ is the friction velocity. The viscosity and density were calculated from the total temperature, Reynolds number and Mach number that were measured during the experiment using basic fluids

relations. The friction velocity is defined as:

$$U_\tau = \sqrt{\frac{0.5 C_f \rho U_\infty^2}{\rho}}$$

where C_f is the local coefficient of friction and U_∞ is the reference velocity, which was also calculated from parameters measured during the experiments. A basic relationship between the C_f and the Reynolds number, based on empirical results, for turbulent flows can be used to estimate the value of the former where

$$C_f = 0.027 Re_x^{\frac{-1}{7}}$$

and the Reynolds number is 1.55×10^7 [10]. This was a different value than used by Cunningham because a different reference length was used. Cunningham used the chord length at the beginning of the wing section. This effort used the length of the strake at the wall since it is the largest dimension of the model. Cunningham likely used the wing chord length since the strake was added to an existing delta wing model. The spacing of the finest surface mesh was made sufficiently small to match the fillets that were added to the model at the leading and trailing edge. The surface mesh is shown in Figure 3.3. The surface mesh was extruded an average distance of two boundary layer thicknesses away from the model. This is the distance that was recommended by the developers of Kestrel to best implement the overset, Cartesian off-body mesh. The extrusion utilized a 20% growth rate from the initial spacing to ensure an adequate number of cells were present in the viscous sub-layer of the boundary layer. Three boundary conditions were used with the near-body mesh. The model surface was set to a no-slip wall, the boundary along the tunnel wall was set to a symmetry condition and an overset boundary was used for the outer extents of the near-body mesh. An overset boundary will communicate with the off-body Cartesian mesh and enables the use of the dual-mesh model.
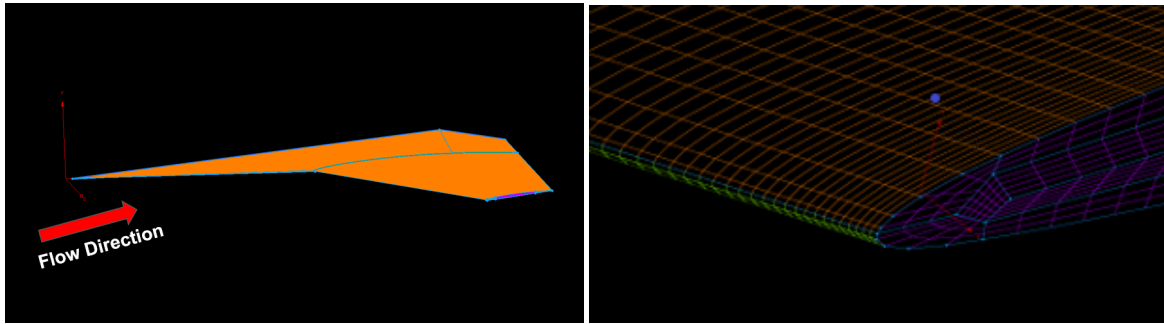
(a) Surface mesh

(b) Surface mesh, zoomed on wingtip region
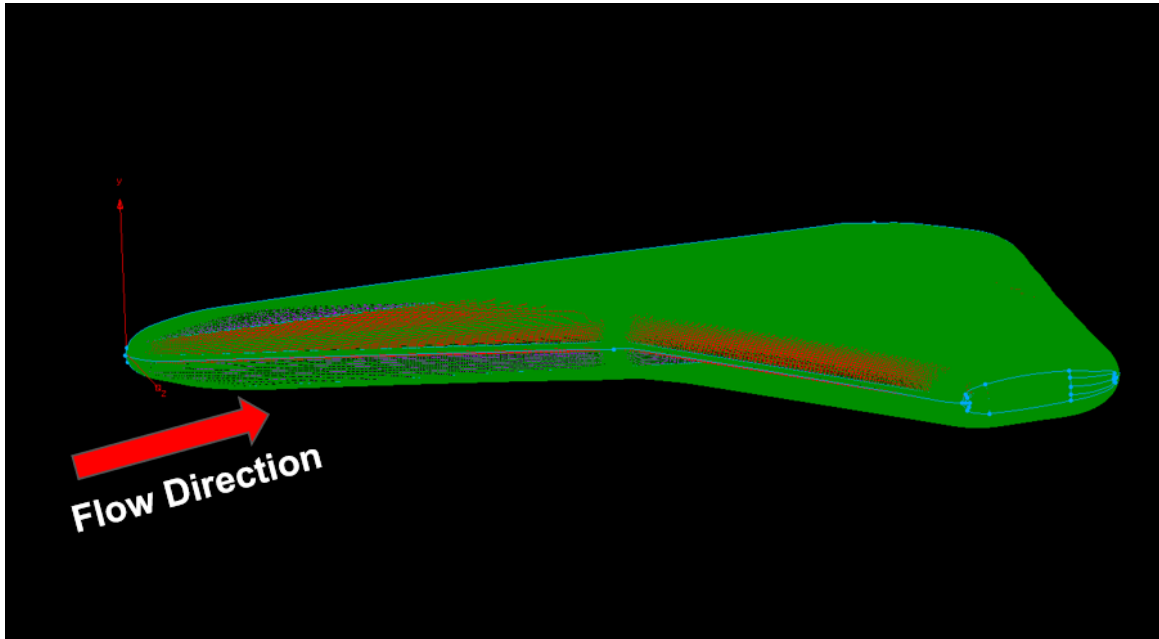
(c) Extruded Near-body mesh

Figure 3.3: Two stages of creating the near-body mesh

The outer extents of the Cartesian mesh were established within Kestrel. Using the root chord of the strake as the reference length, the extents of the model are set around the model. Table 3.2 shows the value used for each of these extents as well as other important figures used to create the computational model. The terms left, right, up, down, forward and backward are in relation to what a pilot would experience if placed inside the model. The "right" direction extent was set to zero since it would be acting as a symmetry boundary. The values for other extents were set based on literature recommendation [18]. Also set in Kestrel is the amount of the

48

Cartesian mesh that is subjected to refinement. These values were initially estimated based on past experience and tested during the convergence runs. The percentages from Table 3.2 were selected since they maintained a smooth transition between the near-body and off-body meshes while keeping the additional computational effort at a reasonable value. The Cartesian mesh was set to refine in the presence of shocks in the flow field using the "shock sensor" parameter in Kestrel. Figure 3.4 shows a slice of the computational mesh at pressure station three where some shock refinement has occurred. The red arrow points to a region with a shock present where a large amount of refinement has occurred to capture the shock. All of the Cartesian boundaries were set to farfield boundary conditions except the right wall, which was set to a symmetry boundary.

Table 3.2: Important parameters used to create the computational model. The off-body mesh numbers represent the number of reference lengths away from the front of the strake and the percentage of the Cartesian extents that were refined around the model

Near-body Mesh	
Initial Spacing	$1.2 * 10^{-6}$ m
Growth Rate	20%
Extrusion Distance	0.013 m
Off-body Mesh	
Forward	10, 25%
Backward	20, 25%
Left	5, 25%
Right	0, 0%
Top	5, 50%
Bottom	5, 50%

The final piece of the model was to create the "tap" files used by Kestrel to specify points of data collection during the simulation. These virtual taps act in the same fashion as their physical counterparts, probing the flow field for specific quantities selected prior to the start of the run. Carpenter is a command-line computational mesh creation tool that is an available component within Kestrel. Besides mesh creation and refinement, Carpenter is also capable of formulating tap files based on an existing mesh. Slices of the domain can be taken at different positions while
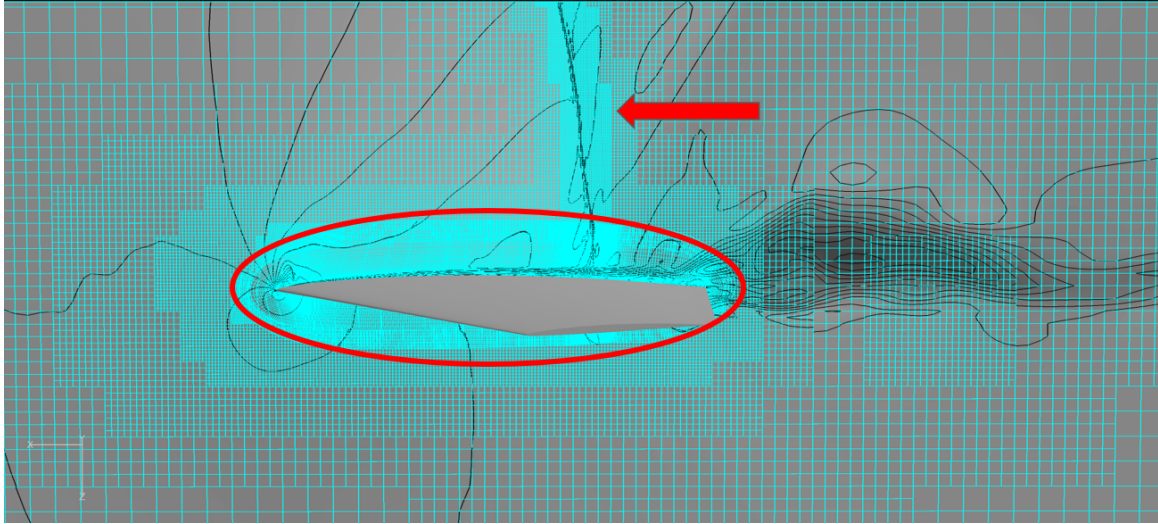
Figure 3.4: Slice of near-body (red oval) and off-body meshes at pressure station three. Refinement using shock sensor, as shown by Mach contours

also selecting different boundary conditions to pull points from. Using these two features, taps were positioned at four different spanwise positions along the surface of the straked semispan. Figure 3.5 shows the taps along the surface of the model. The four positions selected were based on the locations of the pressure tap rows in the Cunningham experiment, ensuring the same spanwise location was maintained along the model. The percent span of each pressure tap location, with respect to the total span length from the symmetry plane to the wing tip, was also calculated for reference. Pressure station one was located at 50.0% span, two was at 65.6%, three was at 80.4% and four was at 94.6%. With the computational model created, the mesh had to be tested for spatial and temporal convergence.

3.2.2   Temporal and Spatial Convergence Study.   As discussed in Chapter 2, achieving spatial and temporal convergence for the computational model is an important step to minimize the error within the model. Also, since the transonic, oscillating flow problem under investigation was to be modeled in an unsteady fashion, temporal and spatial convergence had to be checked simultaneously. To accomplish this task, the original idea was to use the wavenumber method created by Cummings [19]. However, after a number of attempts, no meaningful frequency content could be

50
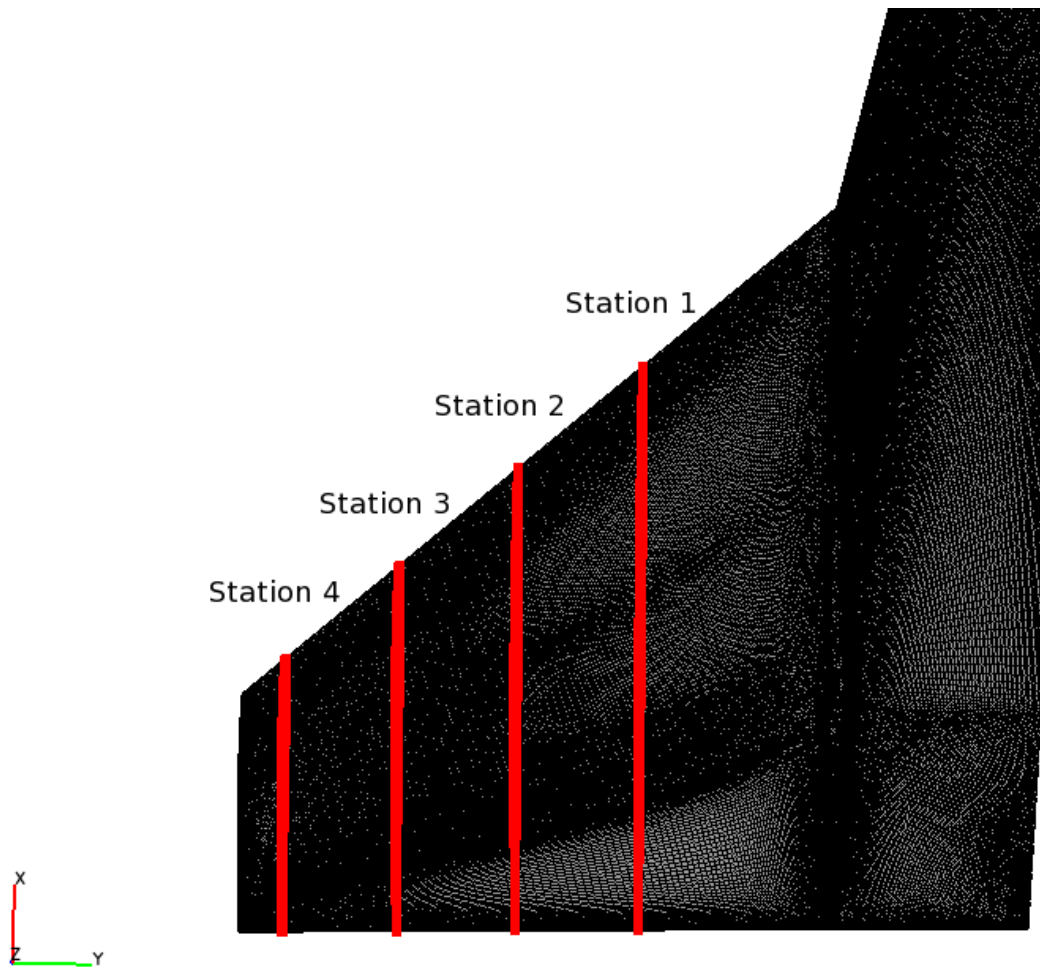
Figure 3.5: Location of taps along surface of straked, semispan model; Pressure station one at 50.0% span, two at 65.6%, three at 80.4% and four at 94.6%

pulled from the data. This lead to a different method being utilized to test for spatial and temporal convergence.

Three different grid refinement levels were created to gather additional data for the spatial convergence study. This was accomplished by systematically altering the number of cells in the surface mesh before the extrusion process. The finest surface mesh was created first and then the number of cells were reduced by the square root of two in the chordwise and spanwise directions to create the medium mesh. The same process was applied to the medium mesh to create the coarse mesh. Each surface mesh was then extruded in the same manner as described in Section 3.2.1. This method resulted in three different meshes of 16 million, 7 million and 3.4 million cells. Each refinement level was then simulated using a number of global time steps to gather the data required to test for spatial and temporal convergence. Four time steps were used for a simulation at 10° angle of attack with each grid refinement level. First, the Cummings method was attempted using the collected data.

Following the method that was laid out in Section 2.3.2, the wavenumber was calculated using the fast Fourier transform function available within MATLAB. The wavenumber was determined from a number of integrated quantities (C_L, C_D and C_N) as well as unsteady pressures pulled from individual tap locations. A PSD was calculated for each quantity and used to find the dominant frequency for that grid refinement level and time step combination. The frequency was then used to calculate the wavenumber for each combination. An example of these results can be seen in Figure 3.6. The PSD plot shows that there is no dominant frequency for any of the time steps tested with the finest grid level. This is indicated by the lack of a large "spike" at a given frequency. The plot of wavenumber versus non-dimensional time step indicated similar behavior for all three grid refinement levels. The wavenumber should have begun converging to singular value as the grid refinement was increased and the time step size was decreased. Instead, no particular pattern could be pulled from the plot. Because of this, it was not possible to determine spatial or temporal

52
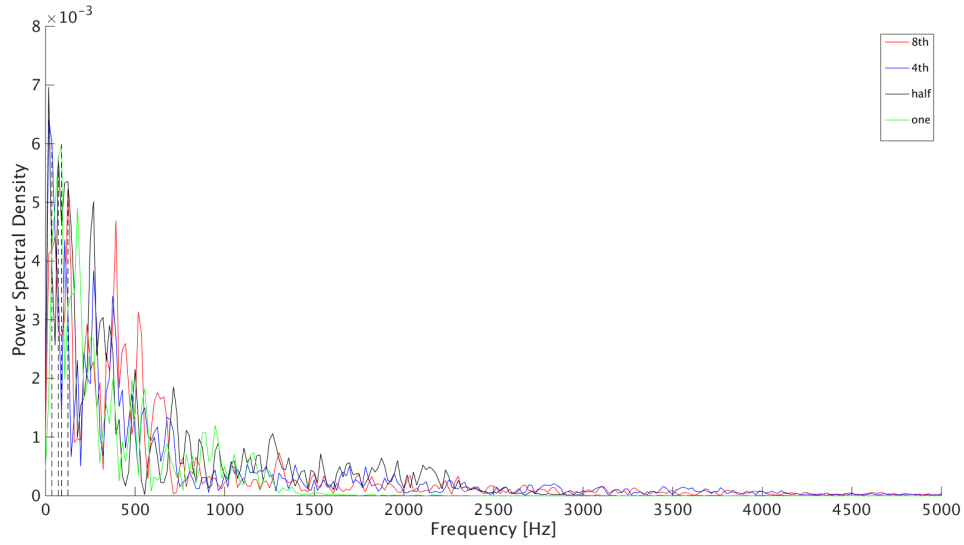
(a) PSD of unsteady C_P on Medium grid with four time steps
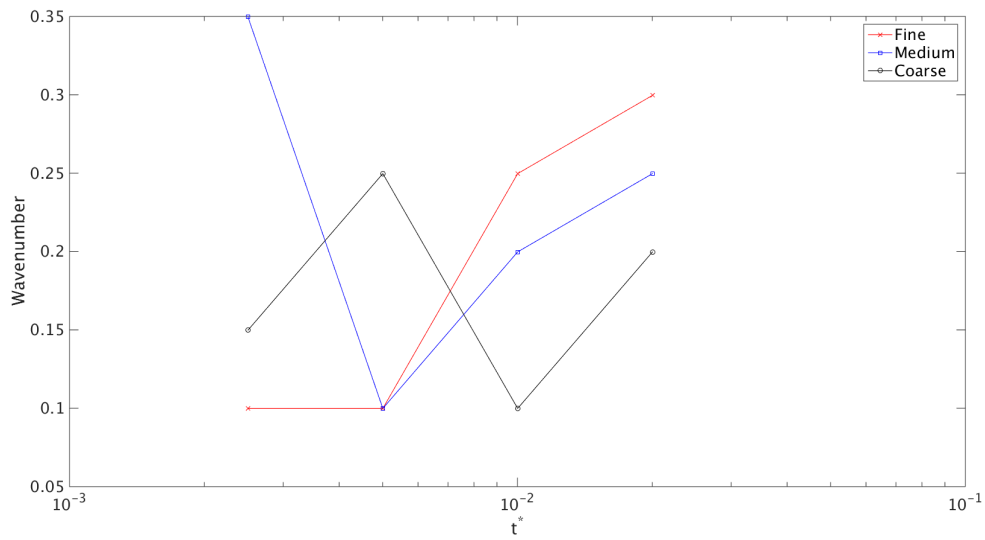
(b) Wavenumber versus non-dimensional time step for all three grid refinement levels

Figure 3.6: Results of wavenumber convergence analysis

53

convergence using this method. Instead, a different path had to be taken in order to the determine which grid to use for the primary simulations and at what time step.

Since the wavenumber method was not effective for this model, a more traditional approach was applied to determine convergence. Figure 3.7a shows C_N for each of the three grid levels at four different time steps. The solutions were captured at a Mach number of 0.9, trim angle of $10°$ and Reynolds number of 1.55×10^7 based on the length of the strake at the symmetry plane. In general, all of the tested grids show the same trend of a decreasing C_N value as the time step is decreased. The only exception to this trend appeared at the smallest time step on the coarse grid, which slightly increased compared to the previous time step. The most important trend from the plot is that the difference between each time step decreases as the size of the time step decreases. This indicates that each grid was moving towards a solution that was no longer significantly impacted by the size of the time step. Specifically, the difference between the smallest time step (7E-6) and the second smallest time step (1.4E-5) was less than 1.5%. This indicated that the second smallest time step was adequate for the bulk of the simulations. Next, the grid refinement level needed for the simulations of interest was determined.

The percent difference between the fine/medium grids and fine/coarse grids versus global time step is shown in Figure 3.7b. The percent difference was calculated using the equation:

$$\Delta_\% = \frac{|C_{N_f} - C_{N_m}|}{C_{N_f}}$$

The plot shows the value of C_N, in general, moves towards a common number as the time step is decreased. The percent difference between the fine and medium grid, at the selected time step, is just below 3%. As a rule of thumb, to ensure the discretization error falls within the 95% confidence interval, a percent difference of 2.5% or less is desired. Since the difference between the fine and medium grid is greater than 2.5%, the fine grid was selected to push the error closer to the desired value. The results of the percent difference in C_N analysis indicated that the addition of an even

54
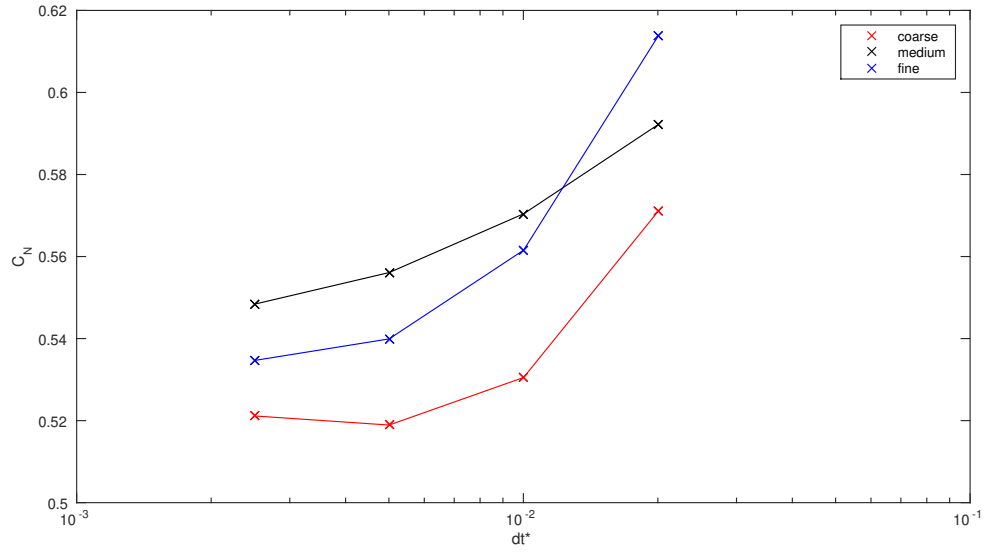
(a) C_N for three grid refinement levels and four global time steps
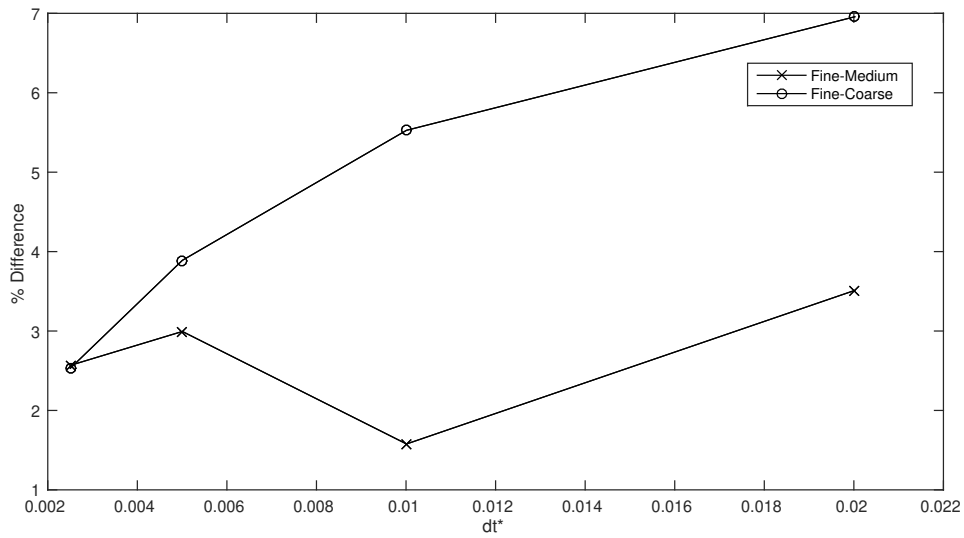
(b) Percent difference of C_N at four global time steps

Figure 3.7: Plots used to determine temporal and spatial convergence

finer grid might have been advantageous to add robustness to the convergence process. However, the creation of a finer grid presented two problems. First, the Kestrel solver has a limit on how small a cell volume can be, which was nearly achieved by the fine grid. Second, an even finer grid would have pushed the x^+ and z^+ values to a similar magnitude as the y^+ value. This is scenario can possibly cause the onset of modeled stress depletion, which severely limits the amount of turbulent viscosity present in the simulation. Because of these factors, the convergence results were used as they were, with the selection of the time step of 1.4E-5 seconds on the fine grid.

3.2.3 Uncertainty Analysis.   Quantifying the uncertainty in experimental measurements is a common practice and an important step to understand the data that was collected. Different measurements techniques, instruments and testing facilities can all have a significant impact on a given experiment. Prescribing values to these error sources gives a range of applicability for the data. Numerical modeling efforts require a similar uncertainty quantification analysis as experimental research. Instead of physical errors that occur during the data acquisition process, numerical uncertainty is introduced by the discretization of the N-S equations and the creation of the computational model. Using the results from the convergence study in Section 3.2.2, the total error from multiple numerical sources can be estimated.

The wind tunnel experiments conducted by Cunningham utilized a wide range of pressure sensors, accelerometers and strain gauges to measure the flow field around the straked delta wing. The exact position of the straked delta wing was also tracked as the model was oscillated in the tunnel. Using the accuracy of these measurement tools and an understanding of the measurement procedures, Cunningham calculated the approximate uncertainty for many of the parameters discussed in the report [6]. Table 3.3 summarizes the uncertainty for the parameters that were utilized to compare the experimental results to the numerical models. The method that was used to arrive at the estimated values were calculated was not included in any of the available doc-

56

umentation on the experiments. While the error of the experiments was provided in the documentation, the uncertainty of the numerical solutions had to be determined.

Table 3.3: Important experimental uncertainty values for comparing to modeling results [6]

Parameter	Uncertainty
Mach Number	+/- 0.001
Reynolds Number	+/- 0.1%
Steady C_P	+/- 0.3%
Unsteady C_P	+/- 0.5%
Turntable Position	+/- 0.002 + 0.0004*α (deg)

To estimate the numerical error present in the simulation, the results of the convergence study were utilized. Again, Figure 3.7 shows the percent difference in C_N between the fine/medium grids and the fine/coarse grids. As discussed in Section 3.2.2, the fine grid was selected for the primary simulations, along with a time step size of 1.4E-5 seconds. Based on the plot, the selected time step would indicate an error of at least 3%. However, since the fine grid is being used, it could be reasonably assumed that the discretization and other types of numerical error present should be lower than 3%. Based on the percent difference at the smallest time step tested, the uncertainty in the numerical solution could be estimated around 2.6%, just over the desired value of 2.5%. Even though the target uncertainty was not reached with this selection, a smaller time step or finer grid could not be used because of the reasons discussed in Section 3.2.2. With the numerical model completed, a test matrix was required that would maximize the amount of data collected across the different flow parameters.

3.3 Test Matrix

The previous efforts focused on examining the flow field around the straked, semispan model, as described in Section 2.4 and 2.5, varied a wide number of parameters to investigate the effect on SITES. Different maneuvers were also employed during the Cunningham testing in order to ascertain the impact of how "flight-like"

57

maneuvers could change the position of the shock on the top surface of the semispan. With those pieces in mind, a test matrix was constructed for the research which is shown in Table 3.4. The basis of the test matrix was taken from the test matrix used by Hope [8], in which he used many of the same parameters as Cunningham. In addition to the tests conducted by Hope, a number of high angle of attack cases were added for this numerical investigation. These cases involved an additional oscillation maneuver besides the basic pitching maneuver used by Hope.

Table 3.4: Summary of maneuvers and variable parameters tested during modeling effort

ID Number	Maneuver	Mach	Trim (°)	Amplitude (°)	Frequency (Hz)
101	Sin	0.90	4	2	5.7
103	Sin	0.90	4	2	7.6
107	Sin	0.90	4	4	7.6
117	Sin	0.90	7	4	5.7
119	Sin	0.90	7	4	7.6
120	Sin	0.95	7	4	76
123	Sin	0.90	7	8	7.6
131	Sin	0.90	10	4	7.6
201	1 - Cos	0.90	6	32	3.8

The two different styles of maneuvers can be seen in Figure 3.8. The first, termed the "sine" maneuver, was used by Cunningham and Hope. the sine maneuver simply changes the pitch of the model in an oscillatory manner, at a set frequency and amplitude. The maneuver begins and ends at the selected trim angle. The first of these maneuvers that was simulated was allowed to run for two complete periods to allow for any numerical transients dissipate. When it was determined there was no significant difference in the solution between the first and second period, only one period was run for the rest of the solutions. The second style of oscillation is the "cosine" maneuver which was tested by Cunningham but not modeled by Hope. This is because an Euler solver like Zeus is not suited to model the highly separated flow likely to be produced at the high α used in the cosine maneuvers. The cosine style was implemented in four different manners by changing the starting and ending point of the maneuver during the Cunningham experiments. The oscillation either

58
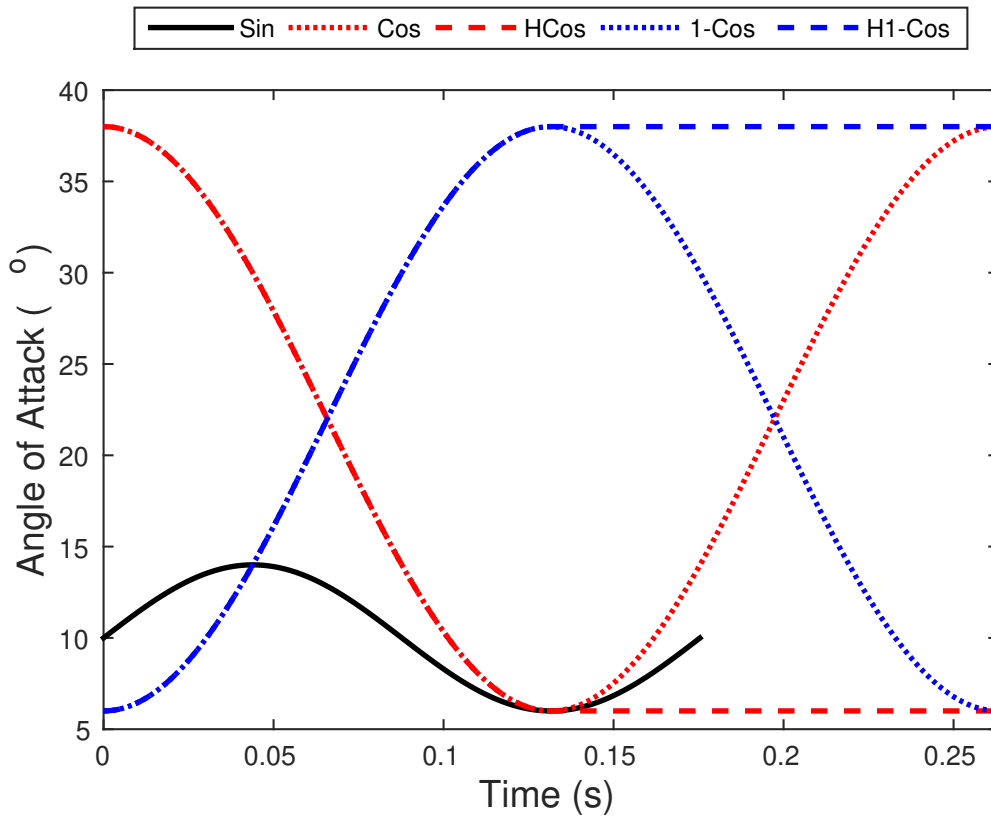
Figure 3.8: Examples of the sine and cosine maneuvers used to investigate the flow field around the straked semispan model. Only the sine and 1 - cos maneuvers were tested in numerical effort.

started at a peak or minimum value and the quickly pitches to the next minimum or peak. From there, a full maneuver would continue back the starting position while a half maneuver holds at the local minimum/maximum. These "pitch and hold" type maneuvers are more representative of actual flight conditions. Due to the computational requirements of simulating the very high angle of attack cases, only one maneuver was finished during the research effort.

3.4 Chapter Summary

Building a computational model of the Cunningham wind tunnel experiments was a multi-step process. First, the computational solver Kestrel was selected because

of capability to utilize overset meshing techniques and its integration with the DoD HPC systems. Next, three different meshes were created based on the geometry used by Hope during another numerical study. The three grids of differing refinement were then used to conduct a spatial and temporal convergence study to select the appropriate grid and time step for the primary simulations. The results of the convergence study were used to estimate the numerical uncertainty of the computational model. Finally, a number of flow parameter combinations were selected to be simulated which provided an efficient path to investigate solutions sensitivity to a number of parameters. Following the completion of the test matrix, the computational models were then solved using the DoD HPC system Onyx and the solutions were analyzed.

IV. Results and Analysis

After building a numerical model of the semispan used in the Cunningham experiments and obtaining a series of solutions, the data were analyzed. The analysis process focused on achieving a better understanding of the flow field around an oscillating, straked, delta wing while also comparing the new results to previous research efforts. The following sections describe the analysis process and the results of the numerical model that were constructed from it. First, a brief introduction into the types of figures and data used for a majority of the data analysis in Section 4.1. Section 4.2 contains the results of the sine type maneuvers, where are most of the analysis is focused. The data and figures showing the results of the cosine maneuver are in Section 4.3.

4.1 Introduction

The solutions of the numerical model of the Cunningham experiment generated a large amount of data to explore the flow field around a straked delta wing. The data generally fell into two distinct but interwoven categories: qualitative and quantitative. Qualitative data and figures utilize the power of CFD to probe the flow field at any point and gain insight into the physics in that area. The visualizations of qualitative data, like the slice of Mach contours shown in Figure 4.1, were used to identify dominate flow features and understand the "global" effects of the oscillation. Different surface plots, pressure and a visualization that showed points of separation and reattachment, were displayed simultaneously to tell a more complete story. Quantitative data and figures made up the other piece of the narrative. Quantitative analysis focused on the tracking the changes in the C_P along the surface throughout the oscillation, using plots like Figure 4.2. The data is pulled from the tap file locations that were discussed in Chapter 3, specifically at 50.0, 65.6, 80.4 and 94.6 percent of the span. The ability to use both types of analysis greatly increased the amount of insight that could be pulled from each simulation. In particular, the quantitative

results provided a tool that allowed for a direct comparison to the experiment and Euler model data.
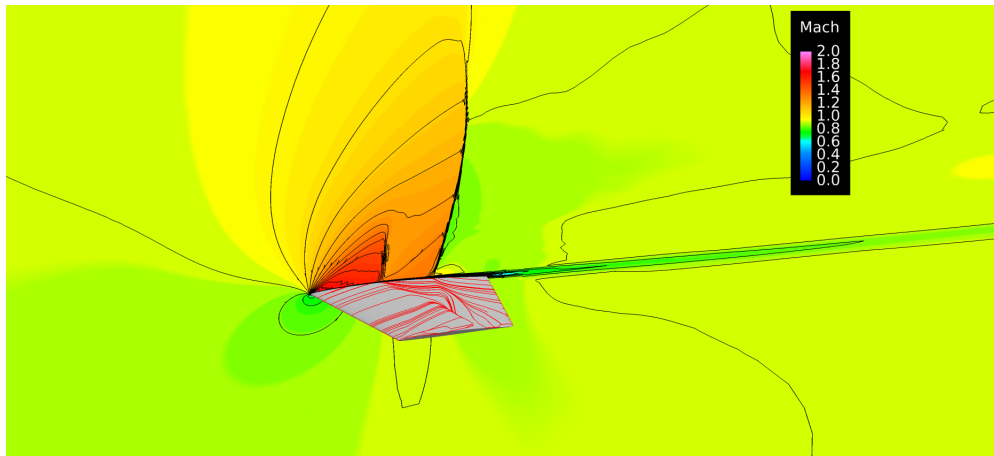
Figure 4.1: Example of qualitative figure showing Mach contour slice at pressure tap location 3 with separation visualization on the model surface
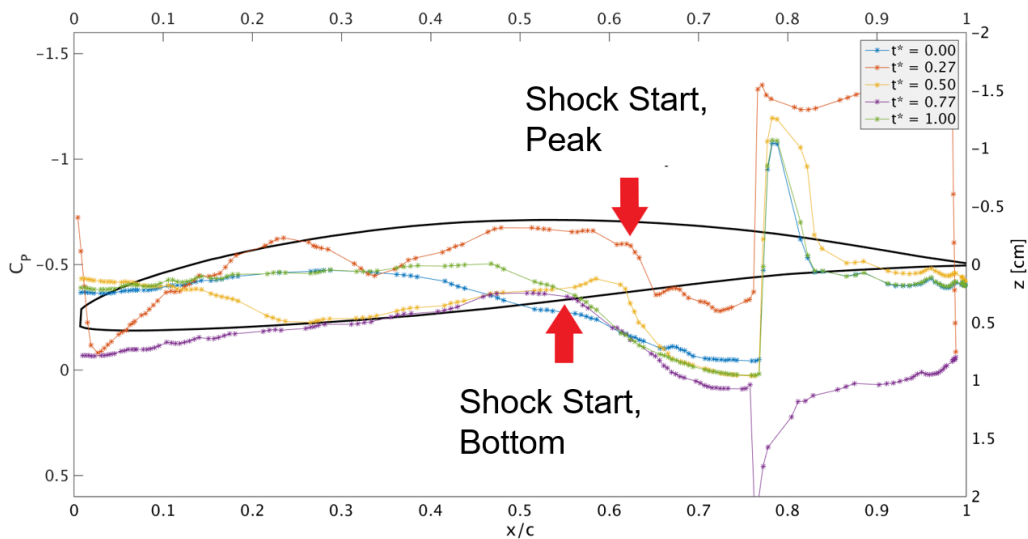
Figure 4.2: Example of quantitative plot showing C_P along the surface of the model versus x-location normalized by local chord length

Determining the amount of shock movement during an oscillatory maneuver would have been difficult to achieve using just the qualitative data. Instead, the C_P surface data was examined using the same method Hope applied to the Euler solutions [8]. Two figures were calculated using information from the C_P plots, the

62

percentage of the chord length the shock translated during the motion and the percent change in C_P during the translation. Calculating the translation of the shock during the motion involved determining the most forward and aft locations of the shock. Figure 4.2 shows an example C_P plot while highlight the forward and aft location of the shock during the oscillation. It is important to note that this percentage is based off the local chord length at each pressure station, which reduces in size with increasing pressure station number. Each C_P plot has plot of the local airfoil shape, which is pulled from the tap locations that collected the data, shown behind the pressure data. The lines plotted are based on a non-dimensional time t^* to allow for easy comparison between cases. The non-dimensional time was calculated with the equation:

$$t^* = \frac{t}{t_{end} - t_{start}} \tag{4.1}$$

where t is the current actual time, t_{end} is the length of the maneuver in seconds and t_{start} is the time the starting point of the maneuver. Equivalent t^* values mean two pieces of data are the same percentage of the way through their individual motions. Also, since the start and end of the motion occurred at the same trim angle, $t^* = 0.00$ and $t^* = 1.00$ are showing the same position. The $t^* = 0.50$ line also occurred at the starting trim angle, however, at this point in the motion the model was pitching downwards instead of upwards.

Calculating the change in C_P across the shock was important since it could be related to the change in forces applied to the surface of the semispan. The location of the maximum and minimum C_P during the maneuver were determined and input into the equation:

$$\Delta_\% = \frac{C_{P_{max}} - C_{P_{min}}}{C_{P_0}} \tag{4.2}$$

so the percent change in the coefficient of pressure $\Delta_\%$ could be calculated, where C_{P_0} is the coefficient of pressure at the starting trim angle when the motion began. Both of the calculations detailed above were vital comparison tools to determine the impact of various model parameters and compare to the previous Euler solutions.

63

4.2 Sine Maneuver

The following sections discuss the data trends observed during the analysis of the "sine" maneuvers and any conclusions that could be drawn from these results. The sine type maneuver was the focus of a majority of the computational effort for this research since it was used for most of the runs during Cunningham's original wind tunnel tests and the sine maneuver was the only one tested on Euler model. Four different parameters varied during the simulations: trim angle (Section 4.2.1), oscillation amplitude (Section 4.2.3), oscillation frequency (Section 4.2.4) and free-stream Mach number (Section 4.2.5). Not every possible combination of the variable flow parameters could be simulated due to the size of the computational mesh and the amount of resources available. Instead, each case of the sine maneuver that was simulated was specifically selected to test the sensitivity of shock translation to multiple parameters. The effect of span-wise position on the semispan was also investigated and the results are shown in Section 4.2.2.

4.2.1 Trim Angle Sensitivity. Three different starting trim angles were tested during the research, 4°, 7° and 10°. The primary focus of this section was to examine the changes in the flow field as the angle of attack is increased but before the motion was started. Each of the three cases examined were simulated at a Mach number of 0.9, oscillation amplitude of 4° and a frequency of 7.6 Hz. The flow field at the beginning of the maneuver for each case is shown in Figure 4.3. Each plot shows the Mach contours at pressure station 3 off the model surface and a visualization of separation and reattachment points on the surface.

Starting at a trim angle of 4° (Figure 4.3a), the Mach contours indicated a relatively typical profile over the top surface of the semispan for a highly chambered airfoil. The free stream flow was accelerated as it passes over the leading edge of the semispan, eventually causing a weak shock to appear at about 20% of the local chord length. After being slowed by the shock, flow again accelerated over the model until another shock occurred at about 60% of the local chord length. The shock

64
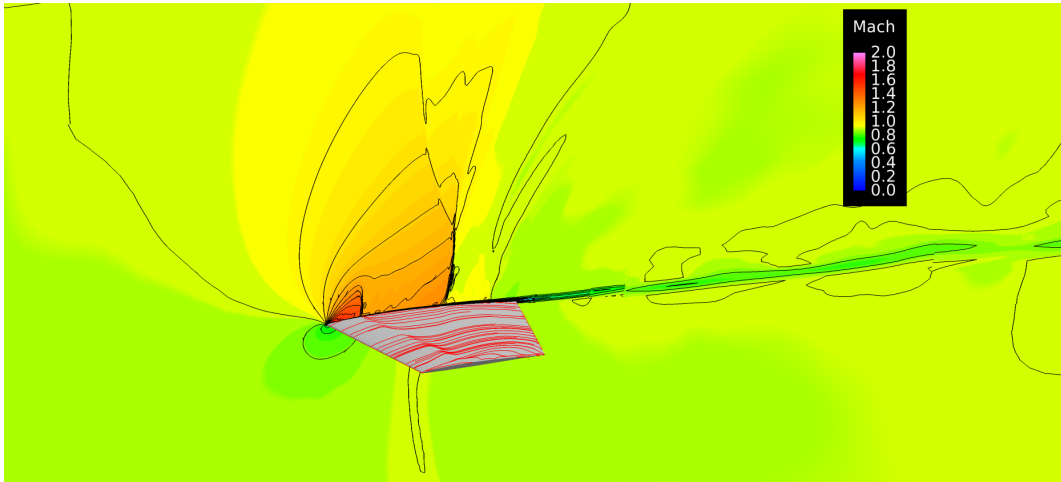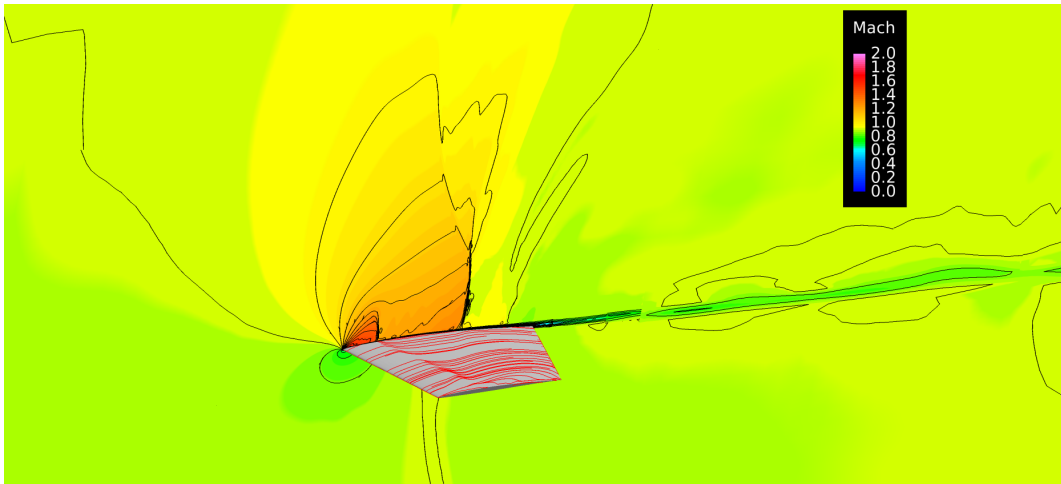
(a) Trim Angle = 4°

(b) Trim Angle = 7°
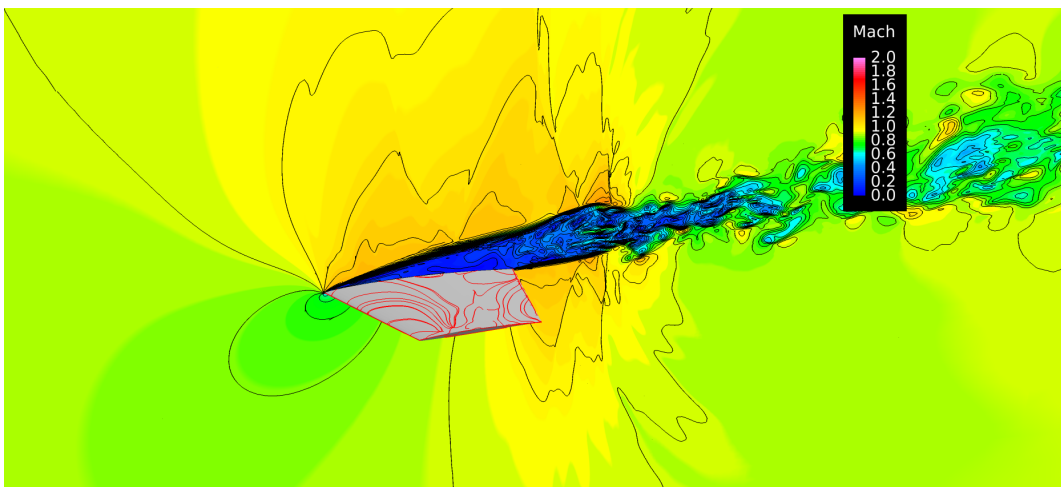
(c) Trim Angle = 10°

Figure 4.3: $t^* = 0.0$ for the three trim angles tested during the research; simulated at Mach of 0.9, amplitude of 4° and frequency 7.6 Hz

65

caused the flow to decelerate back to a subsonic speed and almost separate from the airfoil. This was determined by the region of near separation aft of the second shock and further supported by the surface visualization lines. The visualization lines ran unbroken from the leading edge to the trailing edge showed the lack of separated flow on the surface of the model. Similar trends to these were witnessed on the 7° case. Figure 4.3b showed the flow field around the model at a 7° trim angle. Many of the trends present in the flow field at 4° were also seen at 7°. However, due to the increased angle of attack, the acceleration around the leading edge of the model has been increased. This could be observed by the slightly increased Mach number between the two shocks on the top surface. Also, the near separation region following the aft most shock is larger at the higher angle of attack. This impacted the size of the wake region downstream of the model, increasing its size. The size and severity of the wake region continued to grow as the trim angle was further increased. The flow field at a trim angle of 10°, shown in Figure 4.3c, had completely separated from the top of the semispan. The flow essentially separated immediately upon contacting the leading edge of the model. This behavior could be observed by the large region of low Mach number flow and as well as the surface visualization lines running span-wise along the semispan. This observed behavior in the numerical solution is supported by the experimental work which indicated that separated flow dominates the flow field at a trim angle of 10° and greater [6]. Matching the qualitative results of the wind tunnel experiments with the numerical solutions was a good, first indication that the computational model was matching the physics of the problem to a reasonable degree. For a more quantitative look at the flow field, the C_P values of each trim angle were also examined.

Figure 4.4 shows the surface C_P at the each trim angle, just before the maneuver begins. The lowest trim angle (solid line), the medium trim angle (dashed line) and the highest trim angle (dashed-dot) are all shown just before the start of the maneuver. Upon first glance, the low and medium angles cases both showed evidence of a shock impacting the surface pressure. The could be observed by the increase in C_P over the

66
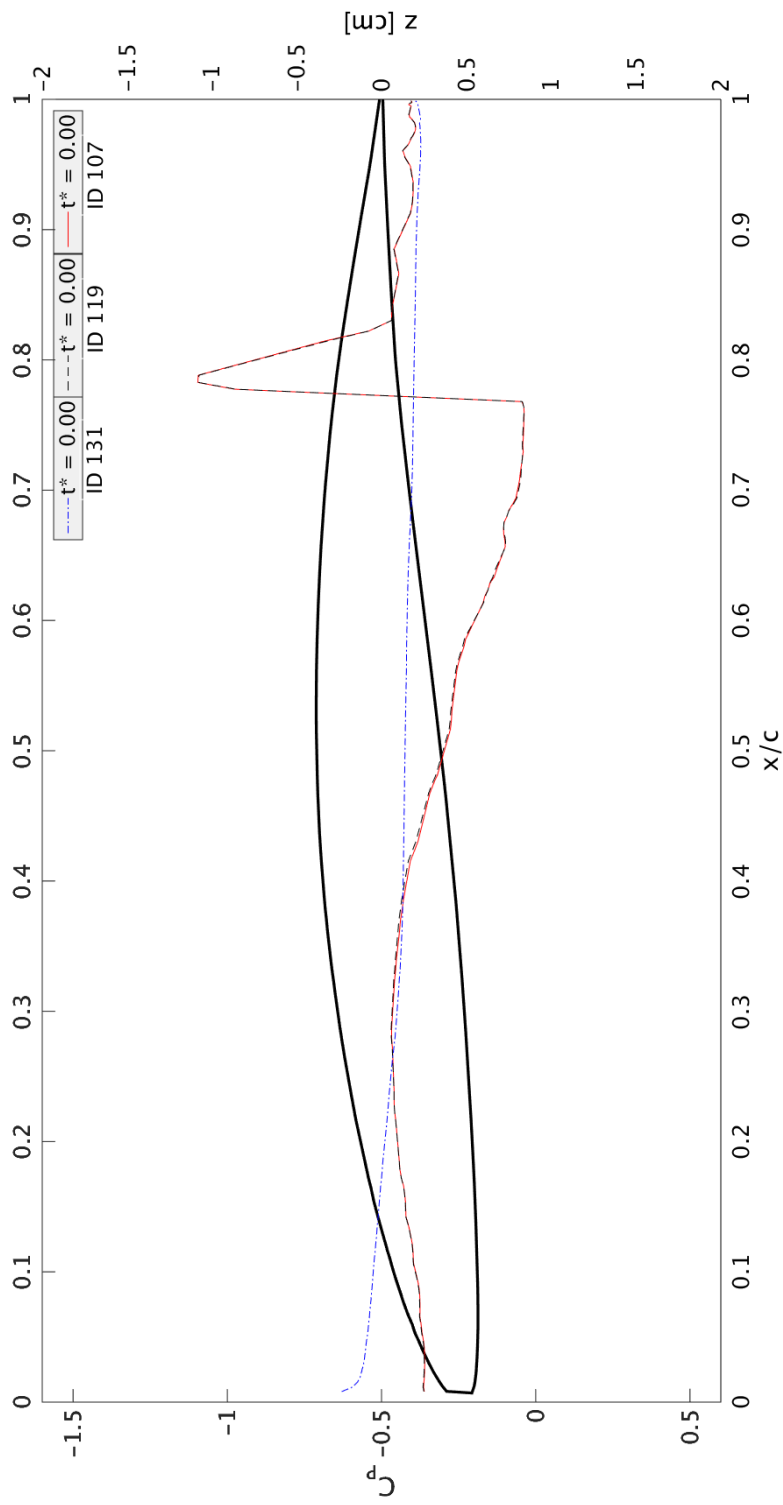
Figure 4.4: Plot of C_P on the upper surface along the chord length at pressure station 3 (80.4%) for each trim angle before the oscillatory motion began. Simulated at Mach of 0.9, amplitude of 4°, frequency 7.6 Hz and trim angles of 4°, 7° and 10°

67

middle of the local chord length. Also, the low and medium cases have nearly identical C_P behavior before the start of the motion. This agrees with the observation made using the Mach contours, which indicated the flow field in each case was very similar. As expected based on the Mach contours, the high trim angle case was completely separated across the entire chord length. The separation could be observed because of the flat nature of the C_P plot. Following the shock for the low and medium trim angle cases, a large spike in negative C_P occurred. This spike is likely representative of a flow phenomenon called a separation bubble. In cases of shocks interacting with turbulent boundary layers, separation bubbles have been found just down stream of these shocks. The small bubble has been shown to cause localized negative jumps in the C_P [28]. No evidence of a separation bubble was observed in the Euler solution but, since it is primarily a viscous, unsteady phenomenon, it would be unlikely for an Euler code to detect it. Based on the available reports, the separation bubble was not detected by Cunningham during the wind tunnel tests. However, due to the small size of the feature, it would have been difficult to detect in an experiment if it was not being looked for directly. Also, the bubble could have been caused by the changes made to the model geometry. This potentially important difference between the models and the experiments was noted before the rest of the analysis began.

4.2.2 Span-wise Location Sensitivity. A majority of the analysis presented in the thesis focuses on pressure station 3, the second most outboard (80.4% span) row of pressure taps on the semispan. This section was selected for two reasons. First, since the mesh point of the wing and strake sections had to be moved toward the wing tip, using data from further away from the mesh point should have a smaller amount of influence from the change in geometry. Second, pressure station four is close to wing tip region and the data there could be heavily impacted by vortices ejecting from the tip. With this in mind, understanding the effect spanwise position had on the surface C_P was an important to verify this choice was correct. The comparison of

68

span-wise position was made at a Mach number of 0.9, the trim angle 7°, oscillation amplitude of 4° and oscillation frequency of 7.6 Hz (ID 119).

Figure 4.5 shows three Mach contour plots at pressure stations one, two and four. The Mach contour at pressure station three can be located in Figure 4.3. There were some stark differences between each span-wise location. First, while all four locations had a clear forward shock near the leading the edge, the aft shock at pressure station four could not be easily located. Also, the length from the leading edge to the forward shock increased as the the Mach contour slice was moved outboard. The aft movement of the leading edge shock could explain the apparent absence of the rear shock at pressure station four, with the possibility the leading shock slid back far enough to effectively merge with the aft shock. The vortical nature of the flow at the tip of the semispan, made apparent by the altered wake region in Figure 4.5c, could have also played a part. Also of note, the surface visualization lines indicated a bit of cross-flow at the same chord location of the forward shock. This was likely caused by flow from the strake spilling out over the wing section and tapering back as the chord length diminished. Based on the qualitative results, the C_P plots of the first three pressure stations could have been expected to by similar to one another, however, that was not quite the case.

Figure 4.6 show the surface C_P at the three pressure stations for case ID 119. The focus of this analysis was on the $t^* = 0.0$ lines of each plot to examine the flow behavior before the start of the motion. The large jump in C_P values on all three plots indicated the presence of a separation bubble across the majority of the outboard wing section. However, the percent chord location of this bubble "slid" aft as the data collection moved outboard. The noticeable shock in the C_P data at pressure station one is between 40 and 60% of the local chord length while the shock at pressure station four is further aft of the leading edge. The position change of the shock was likely caused by the delta shape of the wing and the -3° of twist at the wing tip. Also, the camber of the airfoil and the increased slope in trailing edge region inboard could cause the shock to occur sooner. The strength of the shock at pressure station one

69
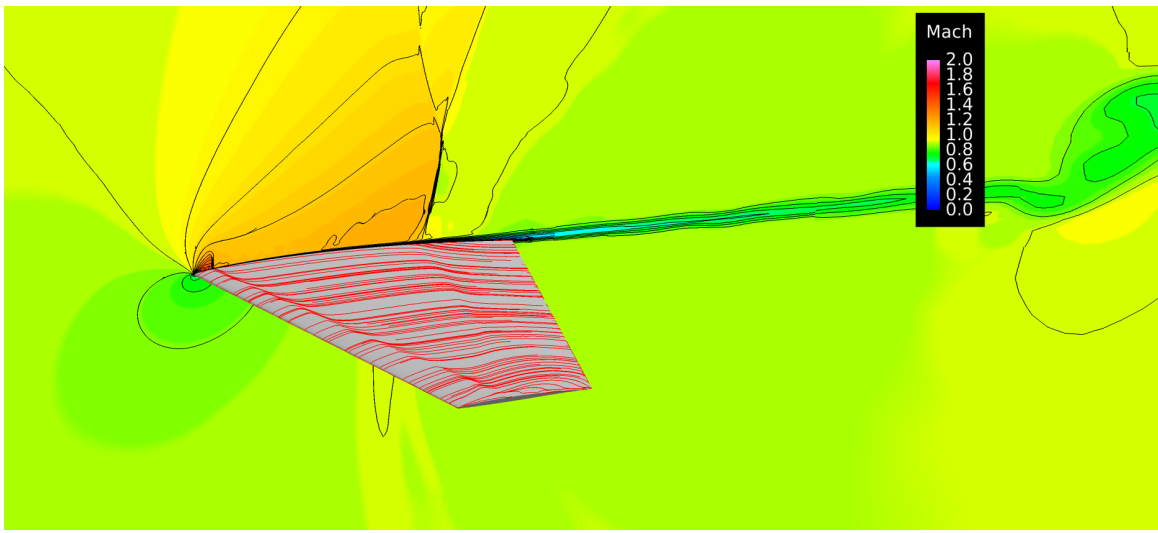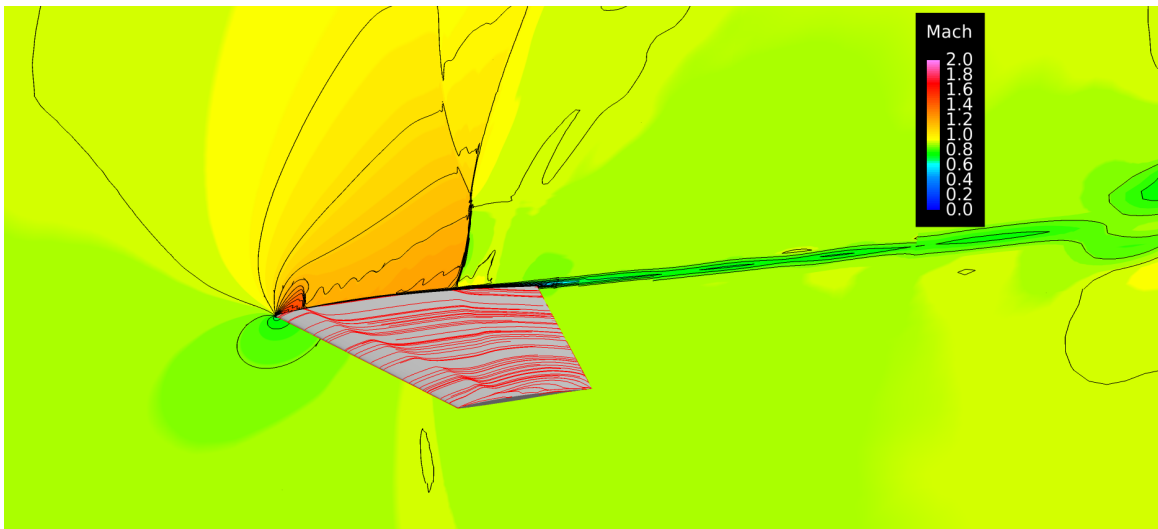
(a) Station 1
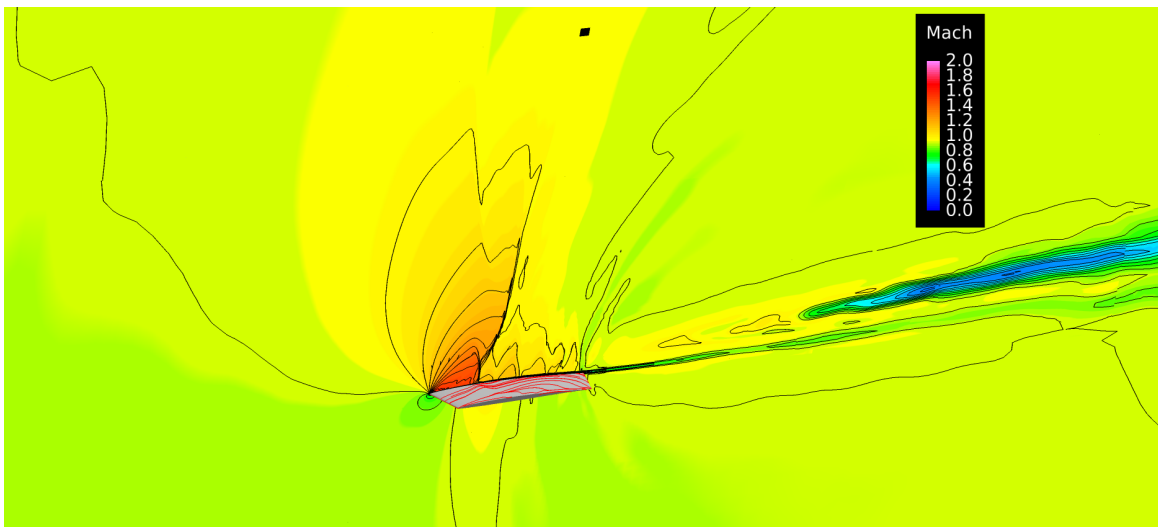
(b) Station 2

(c) Station 4

Figure 4.5: Mach contour slices at $t^* = 0.0$ for pressure station one (50.0%), two (65.6%) and four (94.6%) at Mach of 0.9, trim of 7°, amplitude of 4° and frequency of 7.6 Hz

70

and two appeared to have roughly the same effect on surface pressure, which indicated the shocks present were similar in strength. Figure 4.6 shows the effect of the two shocks was diminished at pressure station four. The effect of the forward shock at the outboard location could have been caused by the flow having less airfoil between the two shock locations compared to the inboard locations. Also, the presence of strong wing tip vortices was likely in this region, which would have had a large impact on the surface C_P. These two differences could have combined to cover-up some of the effect of the forward shock on the flow. As mentioned at the beginning of the section, the pressure station three will be the focus of the remainder of the work presented here. The justification provided in the opening of the section (collect data away from the mesh point and away from the wing tip) was proven by the numerical solutions. However, the C_P plots at all four stations were examined for each simulated case to ensure no interesting or important physics were neglected. Just as with the trim angle sensitivity analysis, the trends observed when investigating the span-wise location of the data collection point were important reference points for the remainder of the flow field analysis.

4.2.3 Oscillation Amplitude Sensitivity.   Three different oscillation amplitudes were used during the simulations. Only certain ones were used at particular trim angles, 2° at a trim angle of 4°, 4° at a trim angle of 4°, 7° and 10° and an amplitude of 8° at a trim angle of 7°. Each of these cases was simulated with a free-stream Mach number of 0.9 and oscillation frequency of 7.6 Hz. Since the trim angle has already been shown to have a significant impact on the flow field (Section 4.2.1), the following cases were compared to other simulations with the same starting trim angle. Figure 4.7 shows Mach contour slices at pressure station three for two run cases with a trim angle of 4°. ID 103 (left column) used an oscillation amplitude of 2° and ID 107 (right column) used an oscillation amplitude of 4°. Each row of the figure steps through the maneuver, starting from the trim angle at $t^* = 0.0$ and going

71
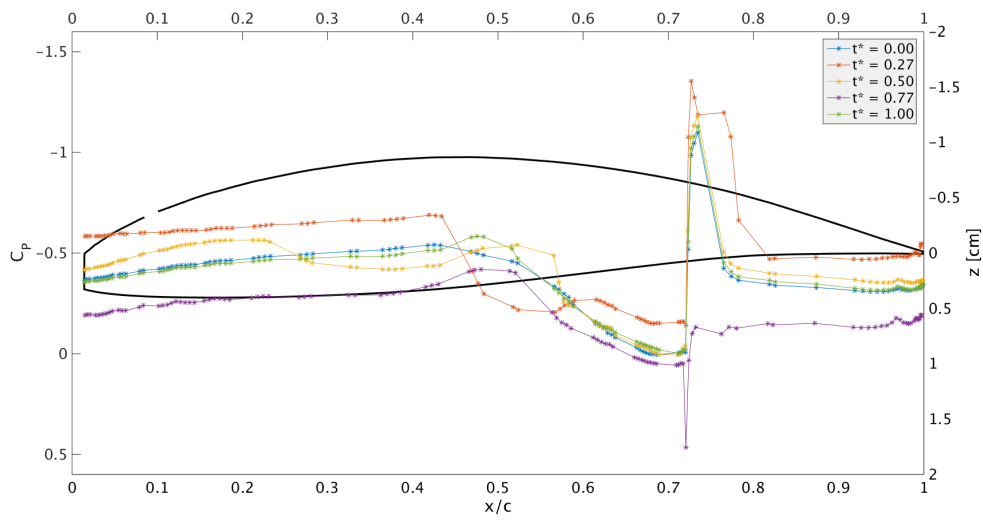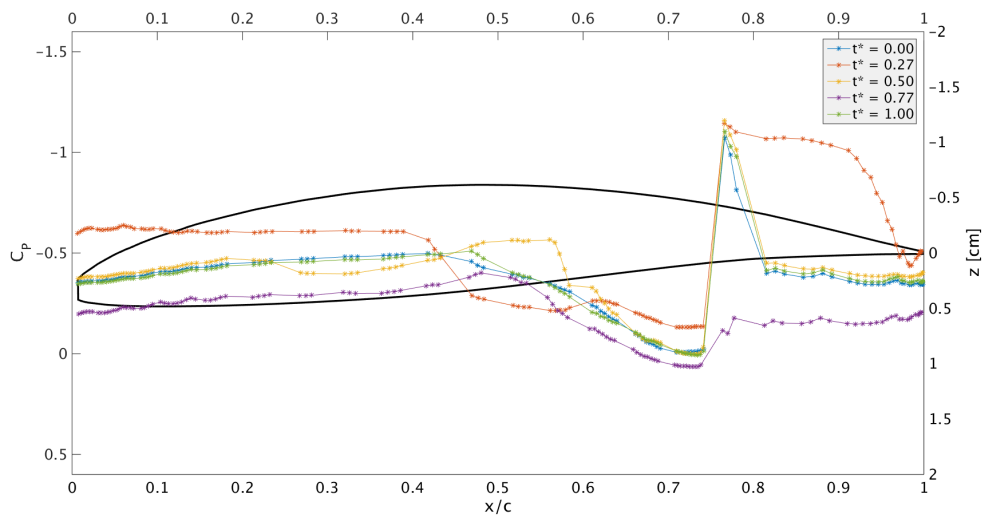
(a) Station 1
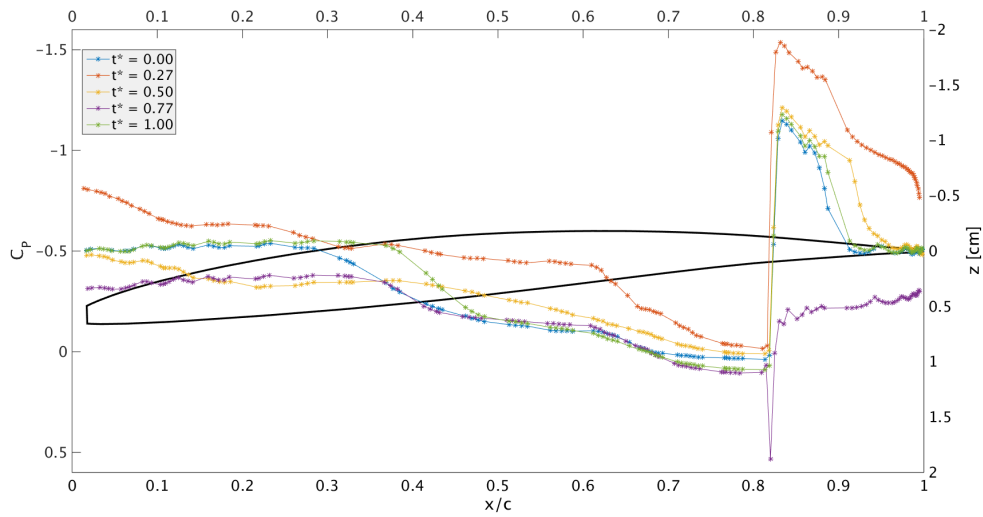
(b) Station 2

(c) Station 4

Figure 4.6: C_P on the surface at Mach of 0.9, trim of 7°, amplitude of 4° and frequency of 7.6 Hz at different spanwise locations

72

the bottom of the motion at $t^* = 0.77$. The Mach contours at $t^* = 1.0$ were nearly identical to the $t^* = 0.0$ case, as expected, so they were omitted from the figure.

Figures 4.7a and 4.7b showed essentially the same solution with minor differences in the wake region aft of the model. Since each case was started from the same static solution, this comparison provided a good sanity check to ensure the model was behaving correctly. Also, it that the hitch motion was not having a significant impact on the flow field. The extensive similarities in the plots confirmed these facts. At the top of the motion (Figures 4.7c and 4.7d), the two cases were quite different. The lower amplitude case still showed two distinct shocks, one forward and one aft. While difficult to observe on the Mach contours, the surface visualization indicated the presence of separation and reattachment after each shock on the top surface. Specifically, the separation following the aft shock showed the SITES phenomenon, with the flow becoming separated immediately following the shock. The Mach contours and surface visualization of the higher amplitude case also indicated the presence of SITES at the top of the motion. In that case, the separation region was large enough to observe just downstream of the shock, as indicated by the bubble-like region of very low Mach number flow. The shock structure of the high amplitude case was more complex than the low amplitude case. A single shock could be seen on the surface, which was a result of the forward and aft shocks merging during the motion. The result was a larger region of acceleration prior to the shock, causing a more abrupt change in velocity over the surface of the model. This additional speed and then deceleration through the shock likely caused the larger separation region compared to the low amplitude case.

Figures 4.7e and 4.7f show the model as it returned to the original trim position on the way to the low point of the maneuver. The flow of low amplitude case reattached to the surface of the semispan, as observed by the surface visualization lines again running from the leading edge to the trailing edge. The Mach contours had a similar appearance to the $t^* = 0.0$ plot, with the forward shock moving back towards the leading edge of the semispan. The same could not be said about the high

73

(a) 2°: $t^* = 0.00$

(b) 4°: $t^* = 0.00$

(c) 2°: $t^* = 0.27$

(d) 4°: $t^* = 0.27$

(e) 2°: $t^* = 0.50$

(f) 4°: $t^* = 0.50$

(g) 2°: $t^* = 0.77$

(h) 4°: $t^* = 0.77$
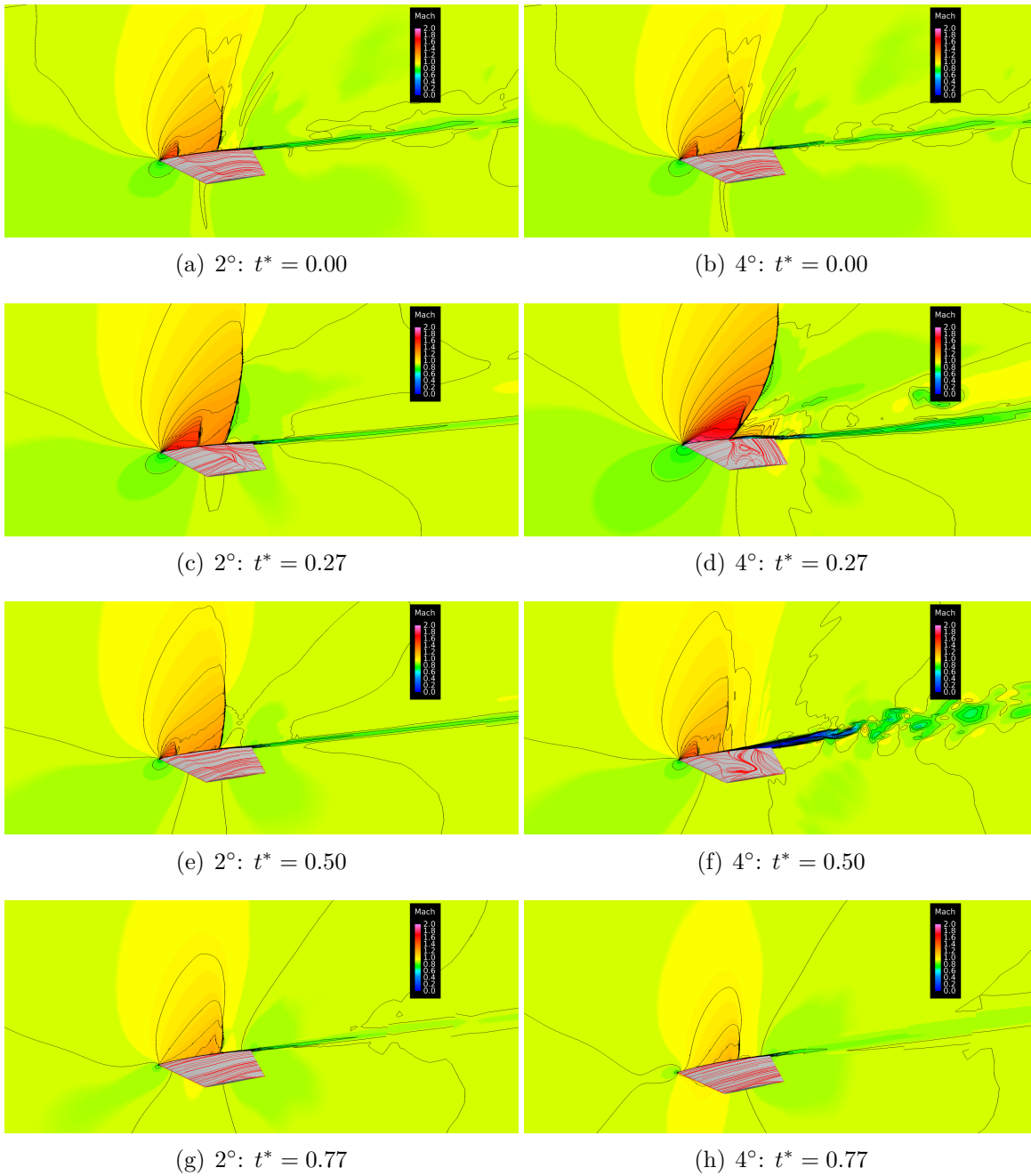
Figure 4.7: Mach contours comparison at pressure station three with a Mach of 0.9, trim of 4°, frequency of 7.6 Hz and varying oscillation amplitude

amplitude case at $t^* = 0.5$, which still had a region of separation aft of the rear shock. The Mach contours showed that the leading and trailing edge shocks had moved apart however, the flow was unable to completely reattach during the motion from the top of the maneuver. Also of note, the aft shock on the high amplitude case seemed to have visibly moved towards the leading edge during the pitch downward. The surface visualization also shows the presence a vortex core closer to the tip of the wing. At the bottom of the motion, as shown in Figures 4.7g and 4.7h, the flow over the top of the model was attached for both cases. Another similarity between both cases was that only one shock was present at the bottom of the motion. The high amplitude case had a less pronounced shock than the low amplitude case due to the small angle of attack (about 0°) at that point of the maneuver.

The first two cases revealed important information about the flow field during an oscillatory maneuver. First, the presence of SITES was confirmed in both ID 103 and 107. This finding at least supports the idea that SITES could be an important aerodynamic phenomenon in the onset of LCO. Another significant finding was that, if the oscillation is large enough, it can cause the flow to remain separated at angles of attack that it was previously attached. This behavior could be important in causing an oscillation to continue if the forces generated by the separated flow are significantly different from the original flow conditions. Finally, the high amplitude case had visible aft shock movement during the oscillation, showing that the shock could translate enough to alter the pitching moment of a given wing. To get a more concrete understanding of the translation of the shock during the movement, the C_P plots for each case were analyzed.

The surface C_P for each trim angle of 4° case is plotted in Figure 4.8. The lower amplitude case (solid lines) and the higher amplitude case (dashed lines) each have five non-dimensional times plotted at pressure station three. Starting the analysis at the moment the maneuver began, a difference between the two cases could be observed. The difference was caused by a small hitch at the beginning of each motion, just before this data was captured. The hitch was an artifact within Kestrel, likely to

75
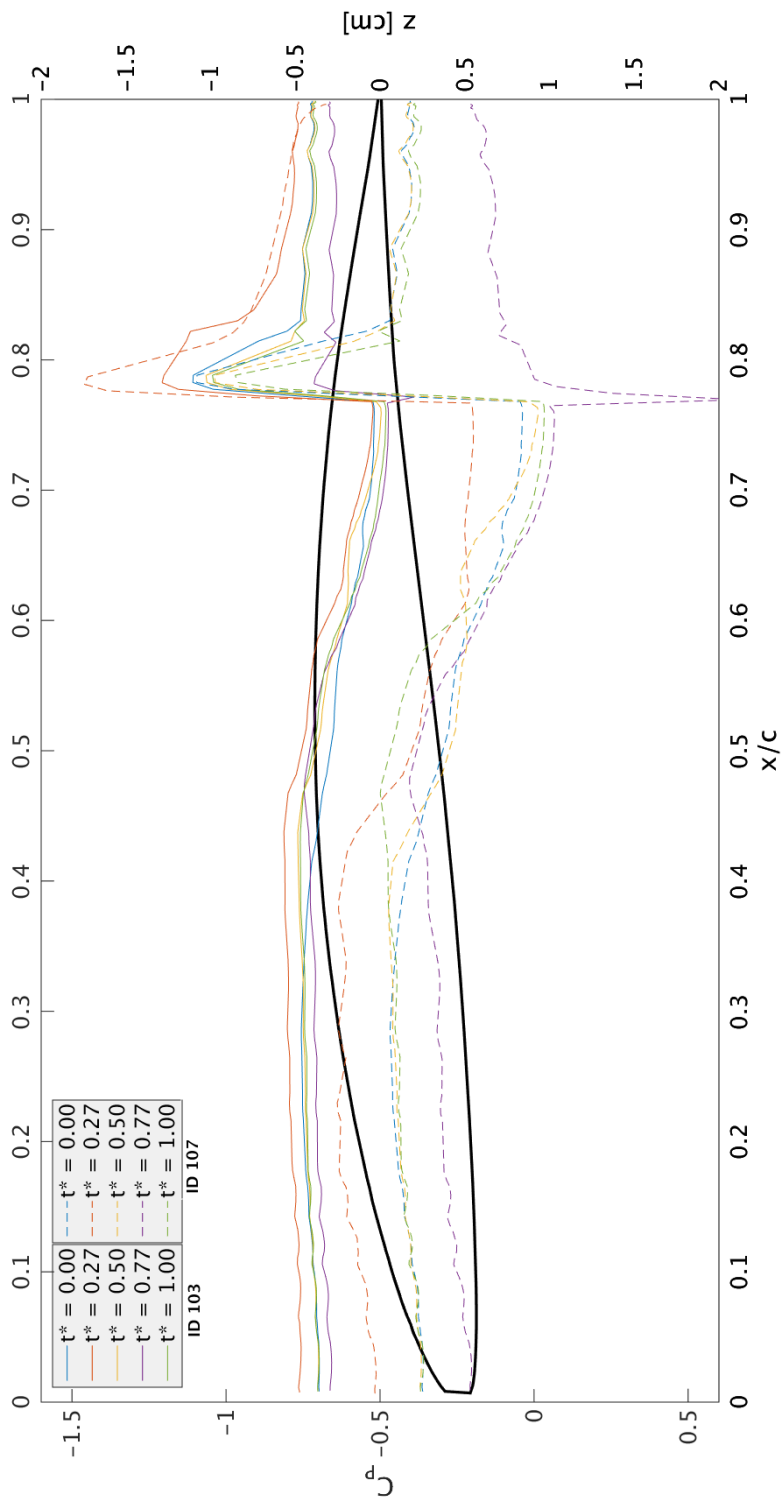
Figure 4.8: C_P on the surface at pressure station three at Mach of 0.9, trim of 4°, frequency of 7.6 Hz and varying oscillation amplitude

allow for a smooth start to the oscillatory motion. The hitch manifested itself as a brief pitch downward and then back up into the motion. The amplitude of the hitch was small (between a quarter and a half of a degree), and actually scaled slightly with trim angle. The hitch was investigated to determine if it had a major impact on the flow field. However, two complete sinusoidal waves for several cases were completed and each period was compared. The comparison showed good agreement between periods, ruling out the long term importance of the hitch in the motion. This was also demonstrated by the similar C_P plots at $t^* = 0.0$ and $t^* = 1.0$.

After rectifying the differences at the first time step, the analysis process focused on shock translation over the top surface of the semispan. The shock for both cases started between 45% and 50% of the chord length. The lower amplitude case showed less shock movement and a weaker shock over the entire motion. This was indicated by the smaller increase in C_P over the length of the shock and that the onset point of the shock did not translate during the motion. On the other hand, the higher amplitude case did show shock translation during the motion. At the top of the motion (highest angle of attack), the shock onset was at 51.4% of the chord length while is was at 48.4% of the chord length at the bottom of the motion. The shock also strengthened considerably between the $t^* = 0.27$ and $t^* = 0.77$ points in the motion; the increase was 61.3%. These results indicated that the amplitude of oscillation is an important parameter in determining the amount of shock translation and change in shock strength. The low trim angle case showed that higher amplitudes caused more translation but more cases needed to be analyzed to attempt to confirm the conclusion.

Figure 4.9 shows Mach contours for two 7° trim angle cases, one with an oscillation amplitude of 4° (ID 119) and one with an oscillation amplitude of 8° (ID 123). Again, four non-dimensional time steps are shown, starting with $t^* = 0.0$. Just as with the low trim angle cases, the Mach contours at the beginning of each maneuver were nearly identical. Each case has attached flow across the entire chord, with the same two shock paradigm that was seen at the lower trim angle cases. As the model

77

was pitched up in Figures 4.9c and 4.9d, both flows separated over the top of the model. The lower amplitude case still had two shocks present over the separation region. The shocks had a lambda shock appearance, indicating a strong shock-boundary layer interaction. The shocks along the top surface of the high amplitude case were essentially totally washed out by the large amount of separation present. The surface visualization also indicated immediate separation as the for the high amplitude case and almost immediate separation for the low amplitude case. This separation was expected since the 10° trim angle case was also totally separated and each of these two cases pitches higher than 10°.

Figures 4.9e and 4.9f show the oscillation returning to the starting trim angle. Both flows are still totally separated along the top surface, as shown by the surface visualizations. A shock could be found near the leading edge of the lower amplitude case, as the flow started working towards reattachment. Just as with the low trim angle cases, the oscillatory maneuver keeps a flow separated past a trim angle at which the flow was attached to the surface. As the model was pitched to the lowest point of the oscillation, plotted in Figures 4.9g and 4.9h, the flow did manage to reattach for each case. The low amplitude case shows a single shock in the Mach contour slice, similar to both low trim angle cases at the bottom of the motion. The angle of attack for high amplitude case was low enough that the shock along the top surface disappeared even though the flow was attached. While there appeared to be some trailing edge shock motion during the high trim angle cases, examining the C_P plots was the only quantify the amount of translation.

Figure 4.10 shows the surface C_P of simulations ID 119 (solid lines) and ID 123 (dashed lines). Upon initial inspection of the C_P data, it was evident that there was a significant amount of separated flow throughout the motion. The low and high amplitude cases showed the impact of several shocks throughout the motion. For most of the motion, each case had a shock occur between 50 to 60% of the chord length. Following the shocks, the separation spike occurred for both cases. The unsteadiness in the flow at the top of the motion could be seen in the oscillatory nature of the those

78

(a) $t^* = 0.00$, $\alpha = 7°$

(b) $t^* = 0.00$, $\alpha = 7°$

(c) $t^* = 0.27$, $\alpha = 11°$

(d) $t^* = 0.27$, $\alpha = 15°$

(e) $t^* = 0.50$, $\alpha = 7°$

(f) $t^* = 0.50$, $\alpha = 7°$

(g) $t^* = 0.77$, $\alpha = 3°$

(h) $t^* = 0.77$, $\alpha = -1°$
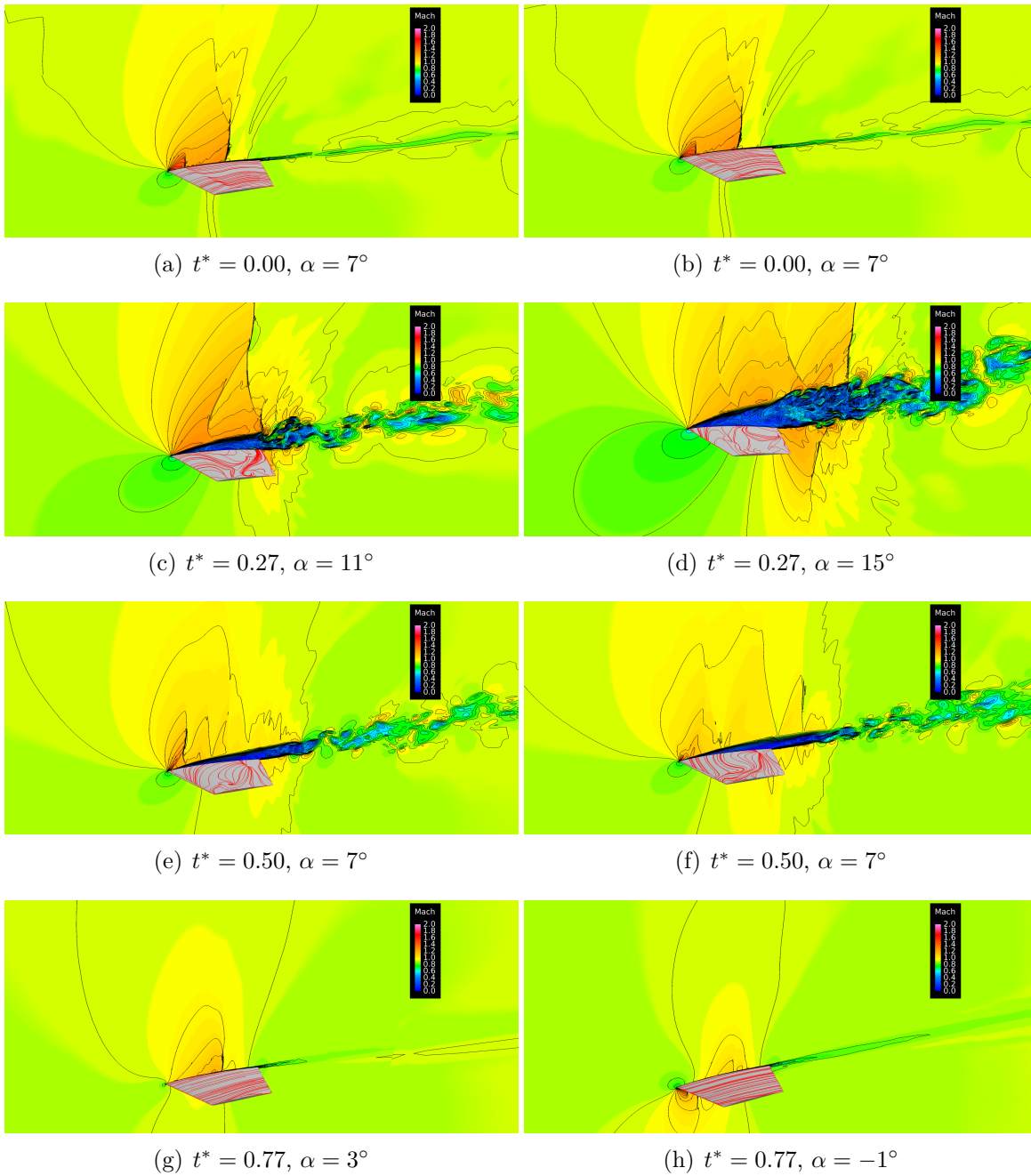
Figure 4.9: Mach contours comparison at pressure station three with a Mach of 0.9, trim of 7°, frequency 0f 7.6 Hz. The left column used an amplitude of 4° while the right used 8°
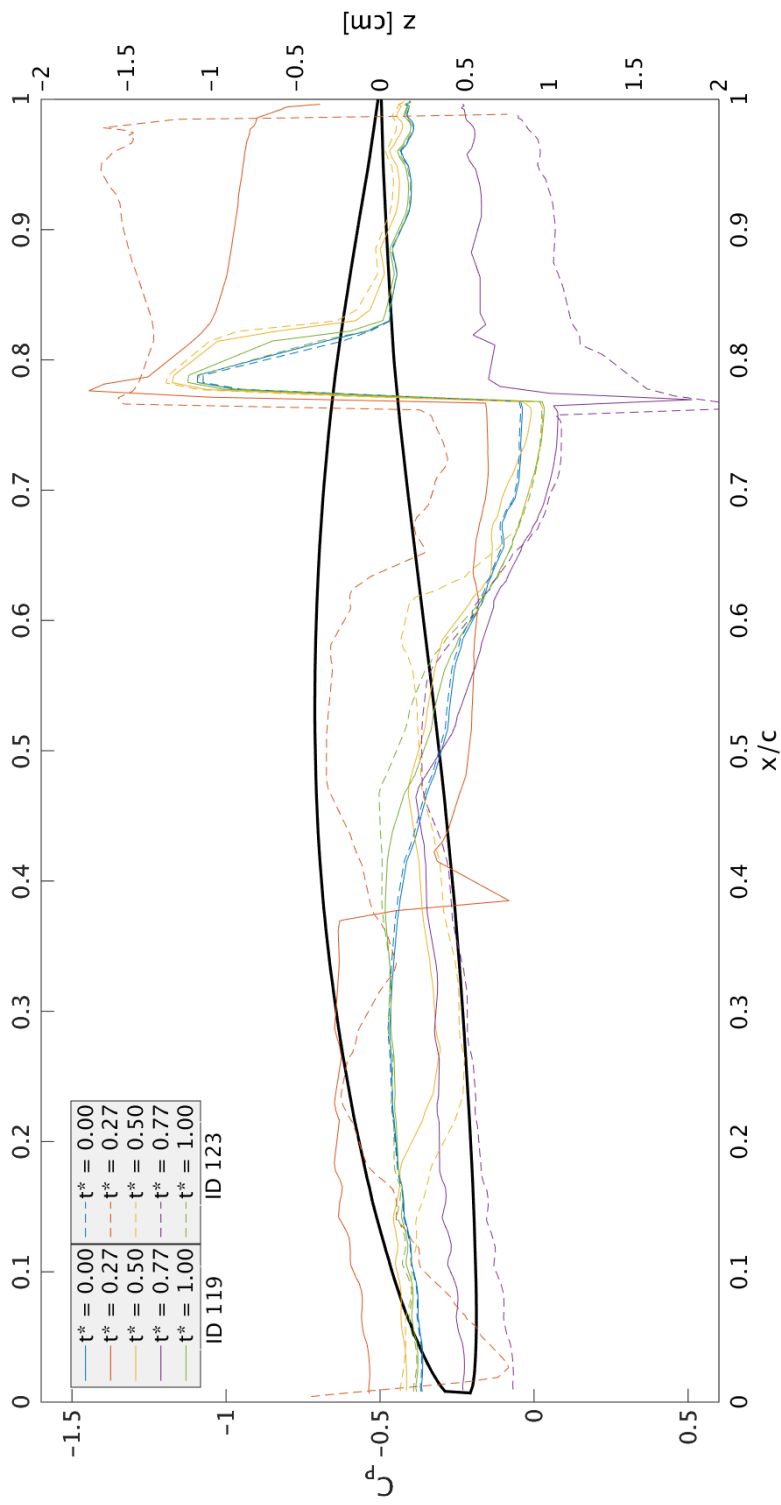
Figure 4.10: C_P on the surface at pressure station three at Mach of 0.9, trim of 7°, frequency of 7.6 Hz and varying oscillation amplitude

lines. The high amplitude case had an extended region of low pressure following the initial separation spike. This agreed with the observation made on the Mach contours that indicated a region of very separated flow near the trailing edge. Both the low and high amplitude cases experienced about the same amount of change in C_P during oscillation (47.0% and 45.7%). However, the lower amplitude case actually experienced more shock translation at the t^* values that were investigated (8.00% and 2.96%). This result opposed the conclusions made using the low trim angle cases. Since the trim angle was shown to heavily alter the flow field, the oscillation amplitude was expected to be a parameter of significance. On the other hand, the oscillation frequency was flow parameter with a less known impact.

4.2.4 Oscillation Frequency Sensitivity. Two different oscillation frequencies were investigated during the research, 5.7 and 7.6 Hz. Two combinations of Mach number, trim angle and oscillation amplitude were each test with both frequencies to determine the impact the frequency of the oscillation has on the flow field. The two variable combinations tested were a Mach of 0.9, trim of 4° and amplitude of 2° or a Mach of 0.9, trim of 7° and amplitude of 4°. The analysis process started with the lower trim angle cases.

A qualitative comparison of ID 101 and ID 103 was conducted to try and detect any significant changes in the flow field due to the change in oscillation frequency. Figure 4.11 shows three different non-dimensional points in time obtained from the low frequency maneuver while Figure 4.12 shows the same three points at the higher frequency. The Mach contours of the two cases show little to no differences between them. Both cases showed a small amount of separation at the top of the motion that has vanished by the time the model sweeps past the original trim angle. Both shocks on the top surface of each case are less pronounced at the bottom of the motion. The only slight difference in the plots when comparing the same non-dimensional time step were very minor changes in the surface visualization lines of separation and attachment. None of these differences were significant enough to expect vastly

81

different flow physics from either case. Next, the surface C_P was examined to check if they were any hidden differences that between the cases that could not be seen on the Mach contours.

Figure 4.13 shows the surface C_P for the two lower trim angle cases, each simulated with a different oscillation frequency. ID 101 was the 5.7 Hz case (solid lines) and ID 103 was the 7.6 Hz case (dashed lines). Upon examining the plot, the line for each of the five non-dimensional times lined up nearly perfectly with the same time from the other case. This result was clearly indicative of the oscillation frequency having little to no impact on the flow field this trim angle and oscillation amplitude combination. This was the same conclusion that was arrived using the Mach contours, providing additional confidence in the theory. Also, Hope observed the frequency of the oscillation had essentially no impact on the Euler solutions. The analysis of cases 101 and 103 showed the N-S solutions, at low trim angles, agreed with this conclusion. After this discovery, the focus of the analysis turned to the higher trim angle cases.

The higher trim angle and oscillation amplitude cases presented more interesting results. Similar to the plots shown in Figure 4.11 and 4.12, spotting clear differences between the Mach contours for ID 117 and 119 was difficult. However, unlike at the lower trim angle, the C_P plot for each case was quite different. Figure 4.14 shows the C_P values at pressure station three for each case at the same non-dimensional point in the maneuver. Also displayed is the results Hope obtained using the same flow parameters at a frequency of 5.7 Hz [8]. As previously mentioned, Hope concluded the impact of frequency on the flow field was minimal for the Euler model so, the 5.7 Hz case can be safely used to compare to both N-S cases. All three of the numerical simulation showed very different behavior over the surface of the model.

The high frequency case showed a trend similar to the rest of the N-S simulations that had been examined, with large jump in C_P between 70% and 85% of the local chord length, likely caused by some sort of seperation bubble just aft of the shock. However, the other two cases did not exhibit this behavior. Instead, the low frequency

82
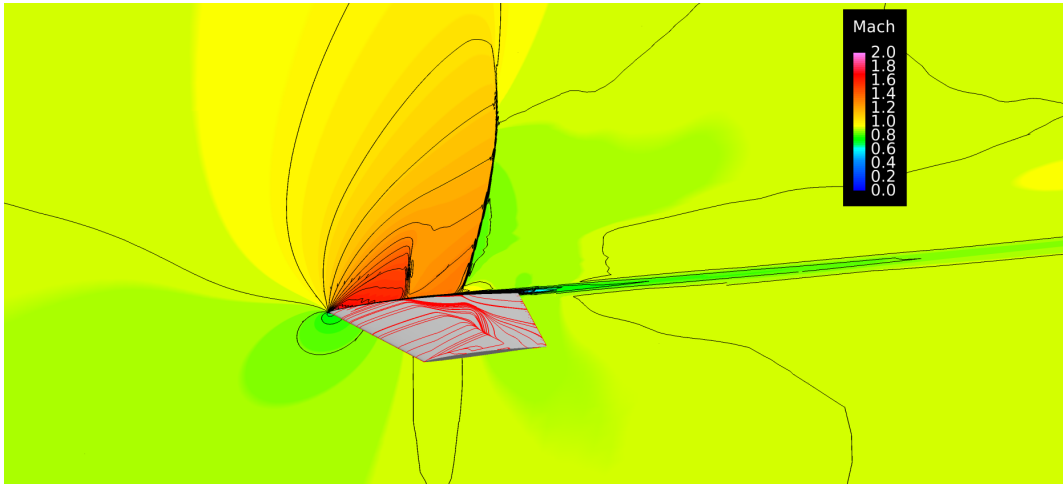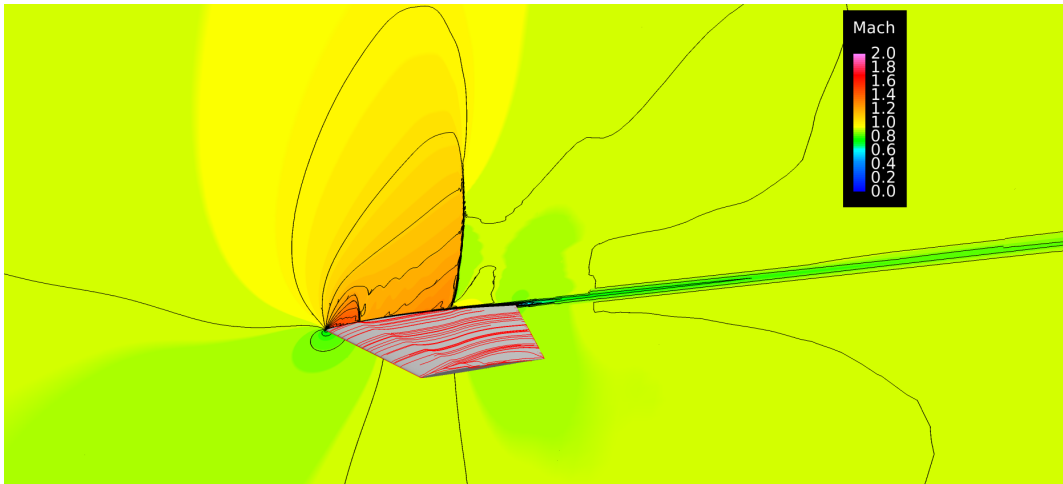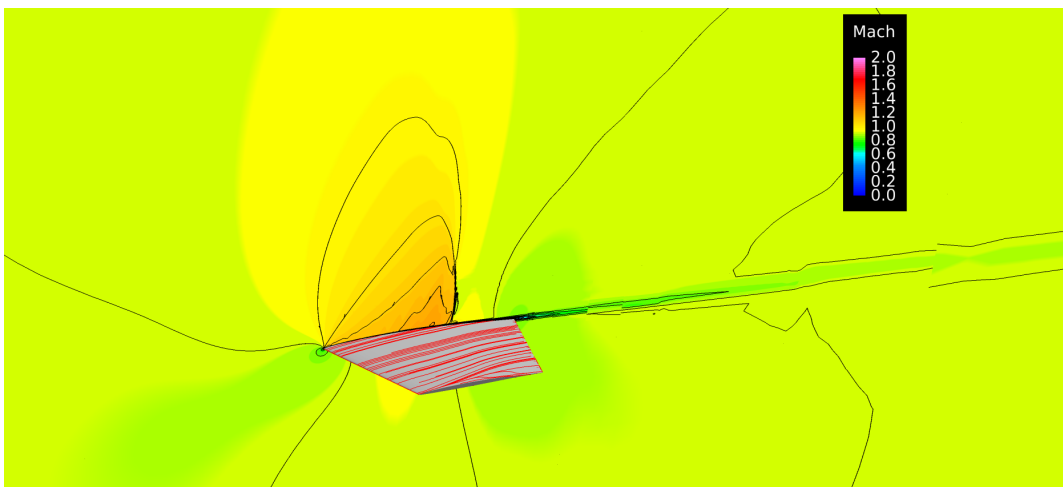
(a) $t^* = 0.27$

(b) $t^* = 0.50$

(c) $t^* = 0.77$

Figure 4.11: Mach contours of 5.7 Hz oscillation case with Mach of 0.9, trim of 4° and amplitude of 2°

83
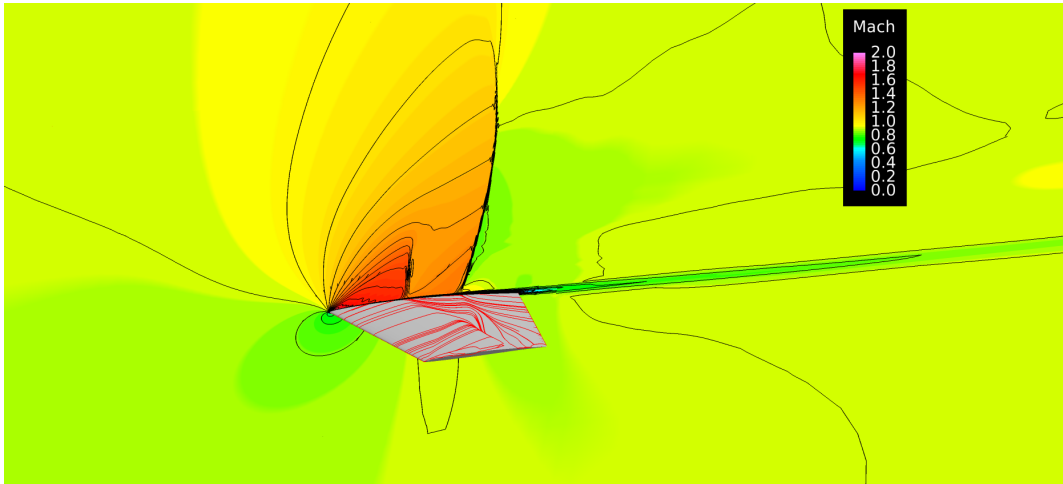
(a) $t^* = 0.27$
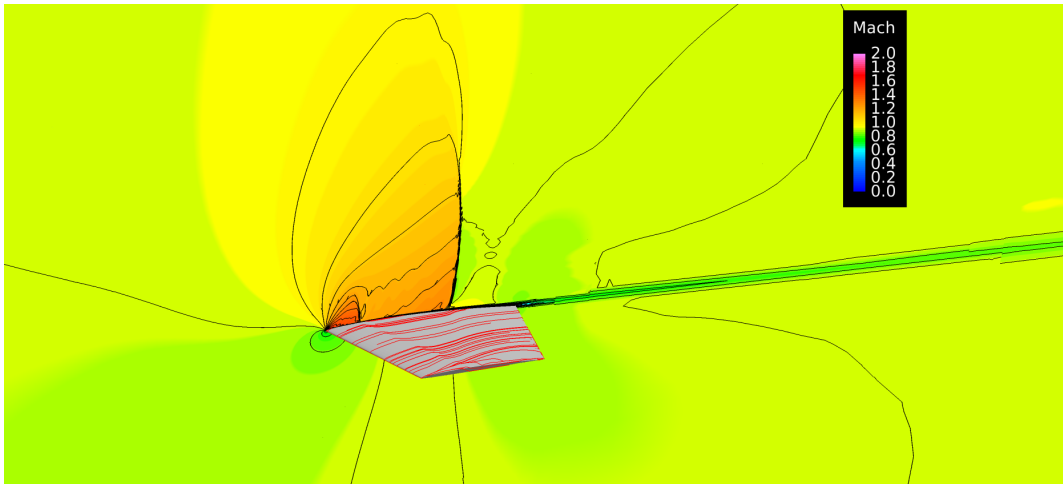
(b) $t^* = 0.50$
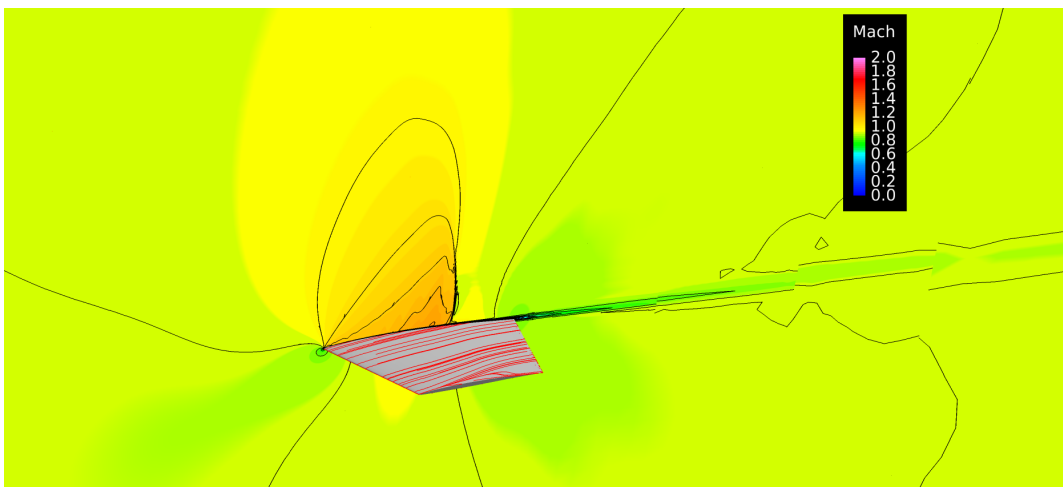
(c) $t^* = 0.77$

Figure 4.12: Mach contours of 7.6 Hz oscillation case with Mach of 0.9, trim of 4° and amplitude of 2°

84
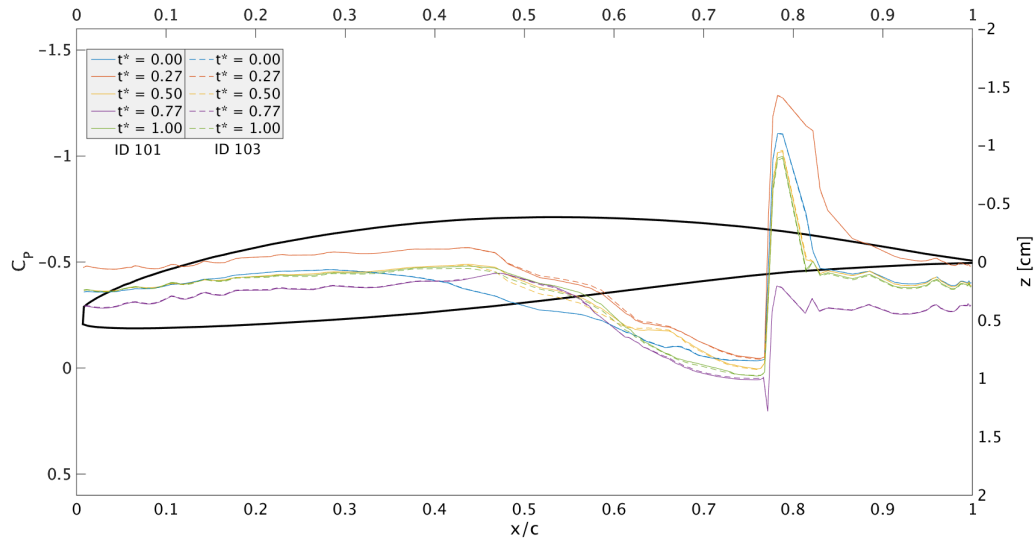
Figure 4.13: Comparison of C_P values at pressure station 3 for runs cases ID101 (5.7 Hz) and ID103 (7.6 Hz)

case lacks the large decrease in C_P, which also seemed to alter the rest of the C_P profile. While this behavior was different from the other cases simulated during the effort, the C_P actually has a more traditional pattern for flow over an airfoil. This was an interesting result since this large difference based on the oscillation frequency did not appear at the lower trim angle. Also, the lower frequency case actually showed better agreement to the Euler case than the high frequency case. As the shown in Figure 4.14, no evidence of a separation bubble was observed in the Euler solutions. This difference in the other cases could be easily explained by the separation being a primarily viscous flow effect, which would not be easily detected with even a boundary layer coupled Euler code. However, further investigation was required to show why the two oscillation frequencies showed such different surface pressure results.

The differences between the the two numerical solutions are shown further in Figure 4.15. The figure shows C_P values, pulled from the 70.0% chord location along pressure station three, plotted versus angle of attack. This figure more clearly showed that the two cases exhibited different trends throughout the maneuver. The low frequency case was much more impacted by the changing angle of attack than the high

85
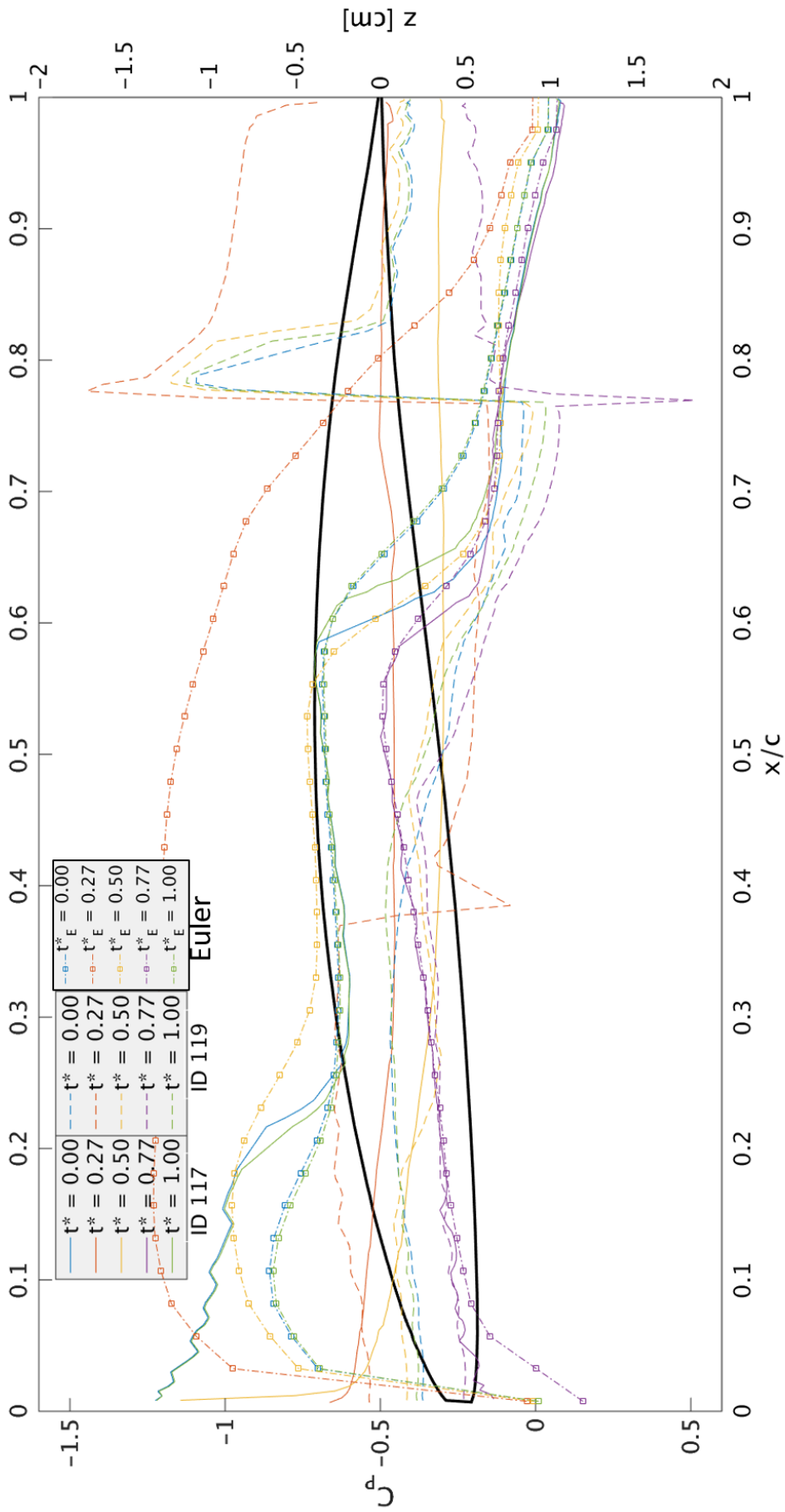
Figure 4.14: Comparison of C_P values at pressure station 3 for runs cases ID117 (5.7 Hz) and ID119 (7.6 Hz), as well as the corresponding data from the Euler model

frequency case, especially at the top of the motion. While both cases showed relatively little change at the bottom of the motion, the C_P values were significantly offset at the same angles of attack. These observations provided a better understanding of how the C_P was changing over time at a specific location along the surface of the model but more information was needed to determine the cause of the differences between the two solutions.
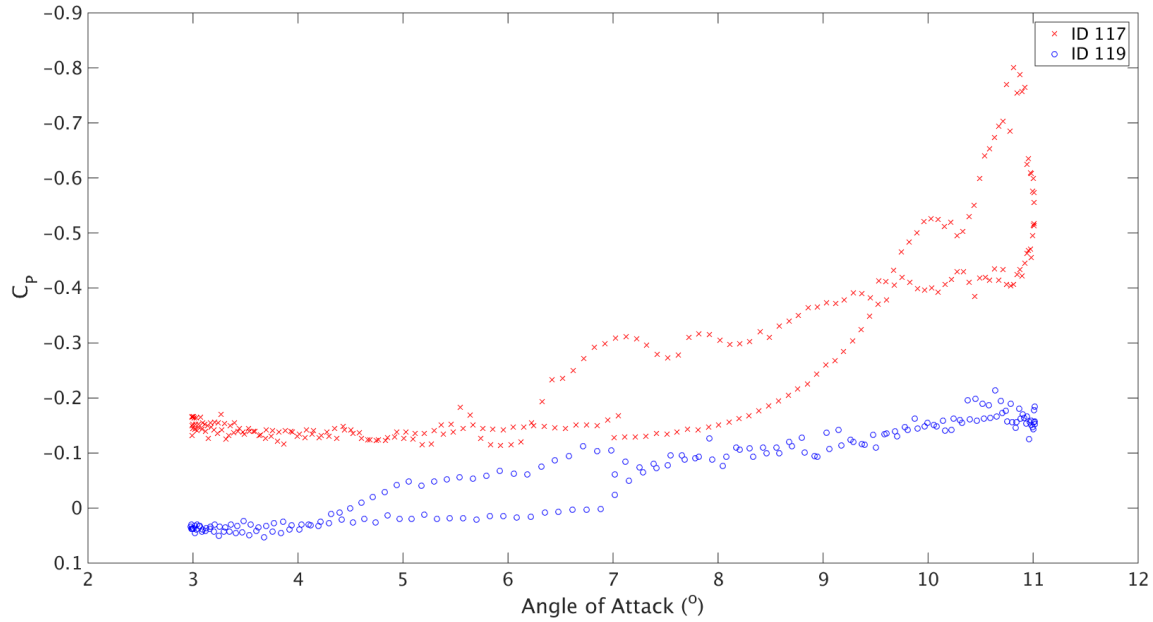
Figure 4.15: Comparison of C_P values at pressure station 3, at 70.0% chord for runs cases ID117 (5.7 Hz) and ID119 (7.6 Hz)

To achieve a more global understanding of the differences at the surface of each case, the pressure was projected on to the semispan for both cases at a number of time steps, which is shown in Figure 4.16. At the beginning of each case, Figures 4.16a and 4.16b, the qualitative plots show similar trends, as they should since these two plots were captured at not only the same angle of attack but the same global time as well. Most importantly, each showed a region of significant pressure increase following the shock. As the maneuvers continued, the qualitative similarities diminished when the same non-dimensional times were compared. This result made sense because of the differences in frequency, which caused the model to reach different angle of attack at different times after the motion began. This was significant because of the

87

(a) 5.7 Hz: $t^* = 0.00$

(b) 7.6 Hz: $t^* = 0.00$

(c) 5.7 Hz: $t^* = 0.27$

(d) 7.6 Hz: $t^* = 0.27$

(e) 5.7 Hz: $t^* = 0.50$

(f) 7.6 Hz: $t^* = 0.50$

(g) 5.7 Hz: $t^* = 0.77$

(h) 7.6 Hz: $t^* = 0.77$
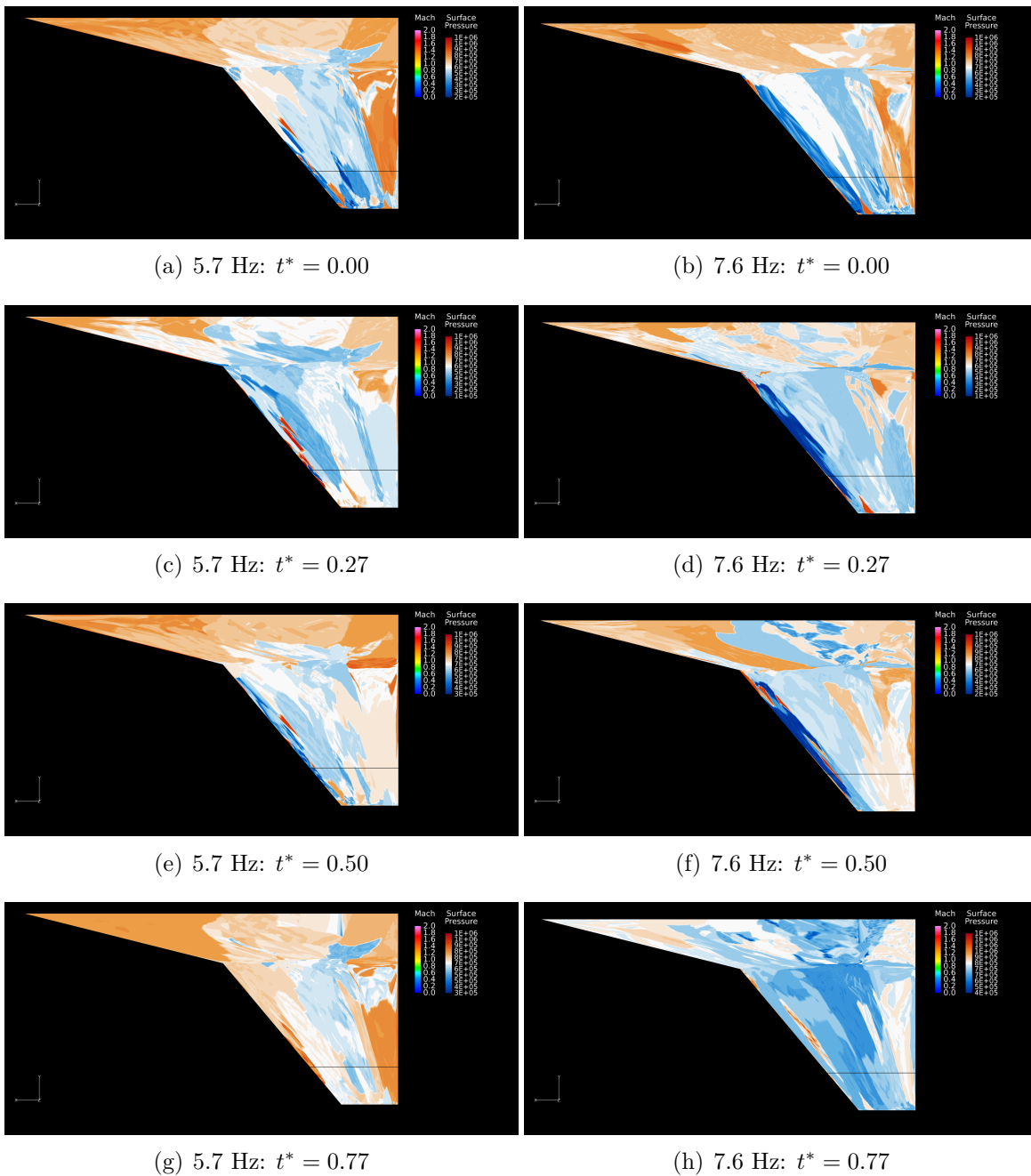
Figure 4.16: Surface Pressure comparison at a Mach of 0.9, trim of 7°, amplitude of 4° and varying frequency

unsteadiness in the flow. At the lower frequency, the flow was given more time to effect the region around it between each non-dimensional time step. Also, based on the free-stream velocity, a "packet" of air could have moved 12.87 meters based on the difference in time it took for the 5.7 Hz case to reach the $t^* = 0.77$ position compared to the 7.6 Hz case. The 12.87 m is over 66 chord lengths at pressure station three. In other words, the peak acceleration of the model at 7.6 Hz was higher than at 5.7 Hz. The higher model acceleration would cause a more significant change to the streamlines above and below the semispan. The difference between the two was pronounced enough to cause the disappearance of the separation bubble. The lack of evidence of a separation bubble in the C_P plot at 5.7 Hz was also like caused by a combination of the unsteadiness in the flow field as well as the elongated motion over the longer period of time.

This new finding directly contradicted the conclusions made from the Euler model and based on the lower trim angle cases. The significance of the frequency at the higher trim angles was likely caused by the amount of separated flow experienced in those cases. The altered frequency presented a different amount of time for the flow at alter the what the surface was experiencing and the unsteadiness caused by separation is a very time dependent phenomenon. Conversely, the flow at the low trim angles in cases 101 and 103 exhibited less intensely separated flow and over a smaller portion of the maneuver. This would indicate the lower trim angle cases would be less dependent on the exact time a solution is collected. The Euler model, even with a boundary coupling capability, would not be capable of determining an accurate solution for regions of large separation. All of these individual observations point to the highly unsteady flows at the higher trim angles and oscillation amplitudes having some dependency on the frequency at which the semispan was oscillated.

4.2.5 Mach Number Sensitivity. To investigate the impact of airspeed on shock translation, two cases were compared that used different transonic Mach numbers. The first case was run at a Mach number of 0.9 (ID 119) and the second

case was simulated at a Mach of 0.95 (ID 120). Both cases had a trim angle of 7°, oscillation amplitude of 4° and oscillation frequency of 7.6 Hz. Figure 4.17 shows a number of Mach contours slices from pressure station 3 at four non-dimensional times. Since the ID 119 case has been examined a number of times during this thesis

(a) M = 0.90: $t^* = 0.00$　　　　　　(b) M = 0.95: $t^* = 0.00$

(c) M = 0.90: $t^* = 0.27$　　　　　　(d) M = 0.95: $t^* = 0.27$

(e) M = 0.90: $t^* = 0.50$　　　　　　(f) M = 0.95: $t^* = 0.50$

(g) M = 0.90: $t^* = 0.77$　　　　　　(h) M = 0.95: $t^* = 0.77$
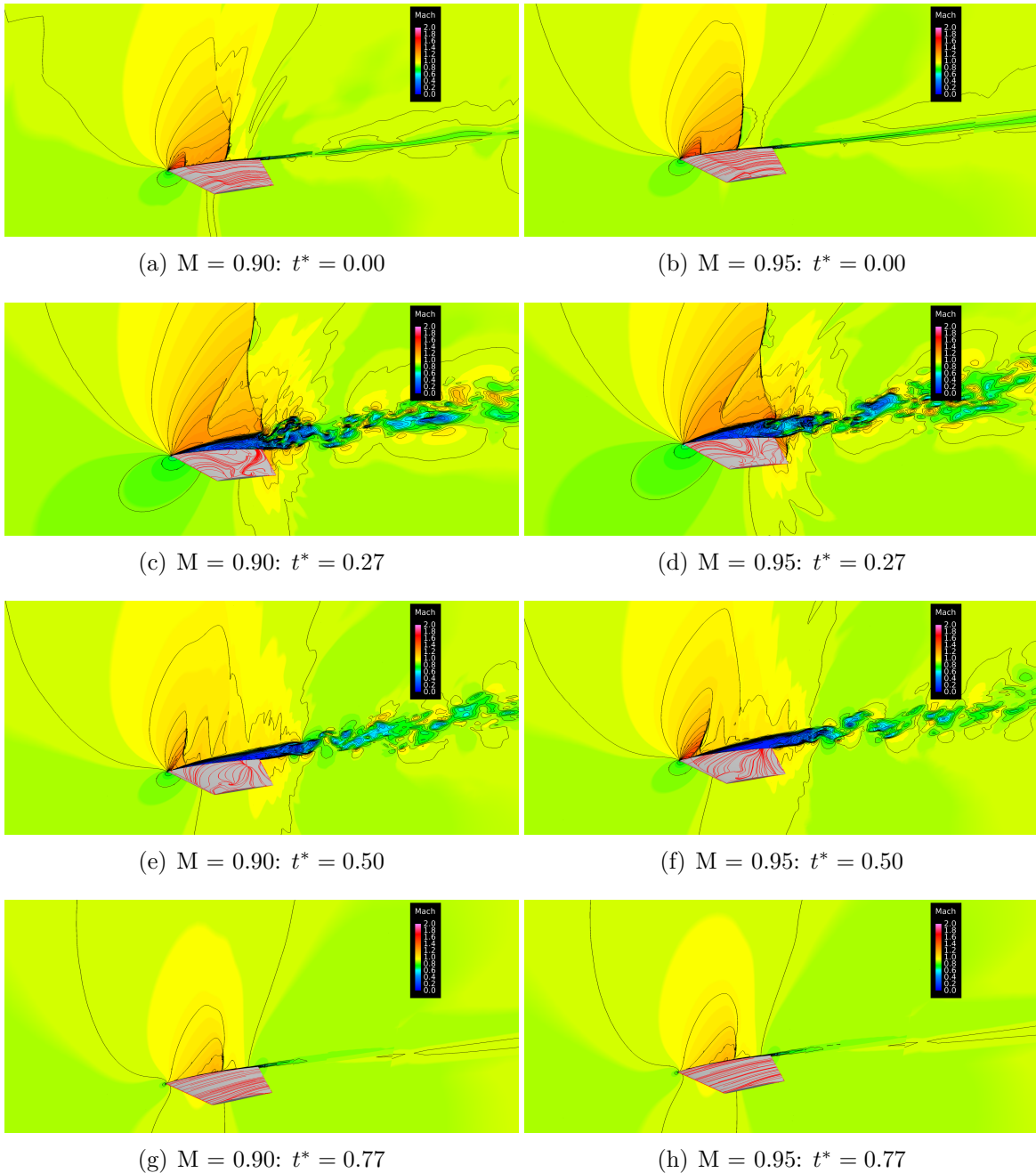
Figure 4.17: Surface Pressure comparison at a trim of 7°, amplitude of 4°, frequency of 7.6 Hz and varying free-stream Mach number.

90

document, most of the analysis will focus on the ID 120 case. First, the beginning of each maneuver was compared. Figure 4.17b shows a similar flow field to the lower Mach number case. The main difference in the contour slices was the higher free-stream Mach case had a slightly "cleaner" Mach contour which was likely stabilized by the higher Mach number. As each model was pitched up in Figures 4.17c and 4.17d, the flow separated for each case. Again, the Mach contours and surface visualization indicated the two solutions were very similar, even presenting the same lambda shock profile in each solution. One of the biggest differences between the simulations is shown in Figures 4.17e and 4.17f. As the model was pitched back down, both flow began to reattach at the leading edge. In the higher Mach number case, the reattached shock at the leading edge was stronger than the lower Mach case. The fact that the higher Mach case began to reattach slightly before the lower could indicate that the point of separation could be severely effected by free-stream Mach number. However, this trend was not reflected in the C_P plot of the two cases.

Figure 4.18 shows the surface C_P for the ID 119 and ID 120 cases. The plots showed that the surface pressure for each case is simply a shifted version of one another. Other than a slight shift, the same t^* values between each case were very similar. The small increase in Mach number did not have a significant impact on the flow field. This is the opposite behavior that was seen in the Euler model, which saw an increase C_P change and shock translation at these flow conditions. The opposing trends could be explained by the differences in the Euler and N-S equations. The Euler model would be more sensitive to changes to the freestream conditions since it lacks the viscous terms that would limit these effects. Understanding the impact of Mach number on the flow field was important to determine because of the wide regime of Mach numbers high performance aircraft can operate in. While a wider variety of Mach numbers should be tested to validate the range of the finding, the numerical simulation results would suggest that the small perturbations in Mach number simply slide the trend line up or down on the C_P chart. This is a potentially important finding that could simplify modeling efforts in the future.

91
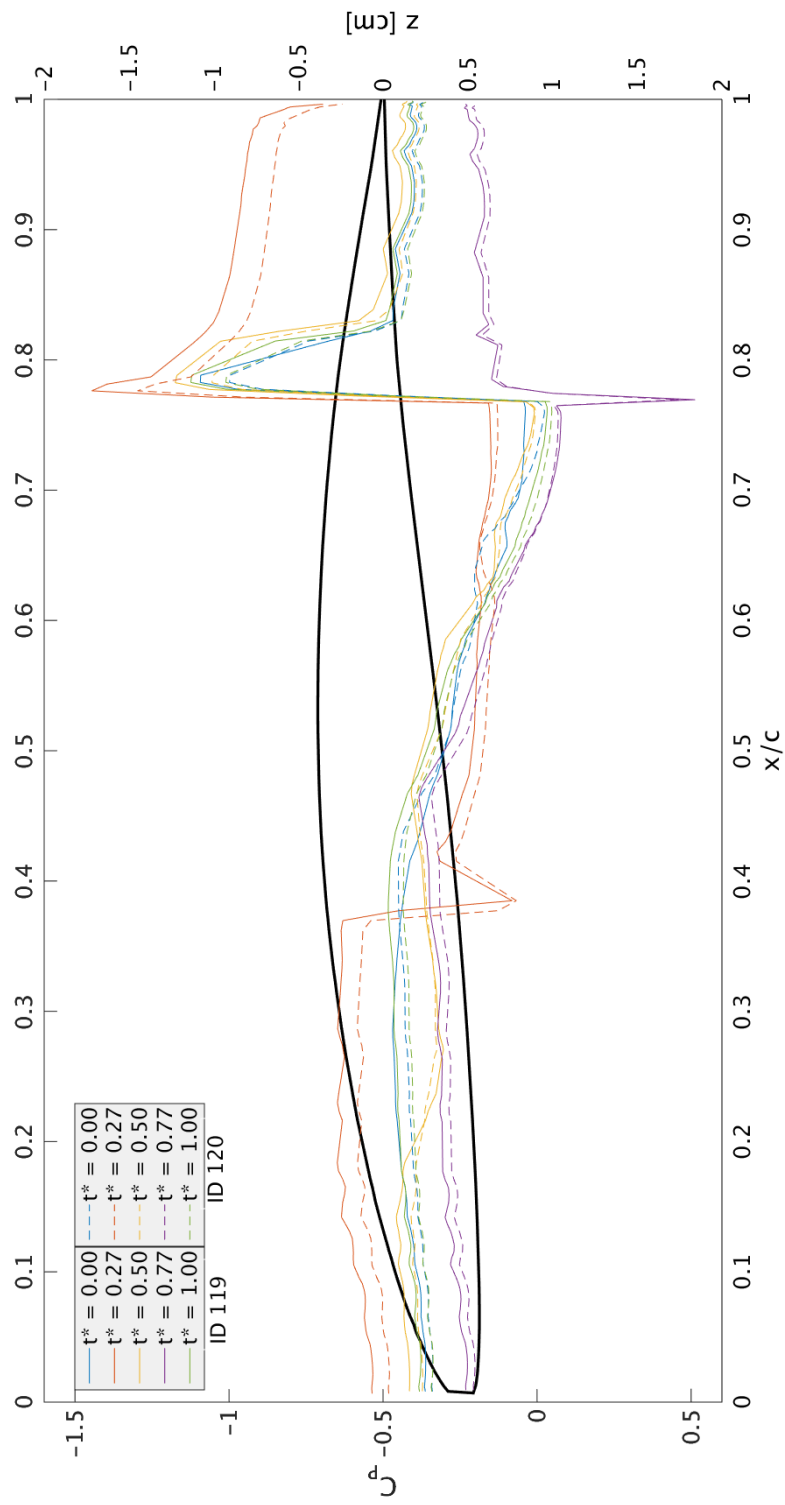
Figure 4.18: Comparison of C_P values at pressure station 3 for runs cases ID119 (Mach = 0.9) and ID120 (Mach = 0.95)

4.3 Cosine Maneuver

After the sine maneuvers were completed and analyzed, a more drastic oscillatory motion was tested. The cosine maneuvers tested by Cunningham were designed to better mimic actual motion a high performance aircraft like the F-16 could experience. The cosine cases were especially trying for the numerical model due to the large change in angle of attack throughout the motion. Also, since the flow field becomes separated at trim angles over 10°, much of the motion will be heavily separated. This increased the computational costs as the mesh refinement attempted to render the large vortical structures present in the Cartesian mesh. For these reasons, only one cosine maneuver was tested using the numerical model. The "1 - Cos" maneuver started at a trim angle of 6°, pitched up to 38° and then back to the original position. The original trim angle was then held for the remainder of the period. The motion was simulated at a Mach number of 0.9 and oscillation frequency of 3.8 Hz. First, the Mach contours of the maneuver were examined.

Figure 4.19 shows a selection of Mach contour slices at pressure station three during the cosine maneuver with the instantaneous angle of attack noted below each subplot. These particular plots were selected to highlight different points of the cosine maneuver. Starting with Figure 4.19a, the flow showed the first signs of separation following a shock at about 60% of the local chord length. The quick change in the angle of attack kept the flow attached over more of the model than was seen at the starting trim angle of 10°. This was yet another demonstration of the flow field exhibiting a slight hysteresis effect, meaning the aerodynamics had not yet fully reacted to the change in angle of attack. All of the points in the maneuver over 10° showed a completely separated flow field over the top surface of the semispan, as shown in Figures 4.19b through 4.19g. The flow field at the top of the motion was dominated by large vortical structures peeling off the leading edge of the semispan. The flow remained separated through out the downward portion of the motion, even when the model initially returned to the starting trim angle, as shown in Figure 4.19h. A brief time later (1.4E-2 seconds), the flow is completely attached at the trim angle of 6°

93

(a) $\alpha = 10.03°$ (b) $\alpha = 15.27°$ (c) $\alpha = 20.26°$

(d) $\alpha = 35.00°$ (e) $\alpha = 33.04°$ (f) $\alpha = 29.83°$

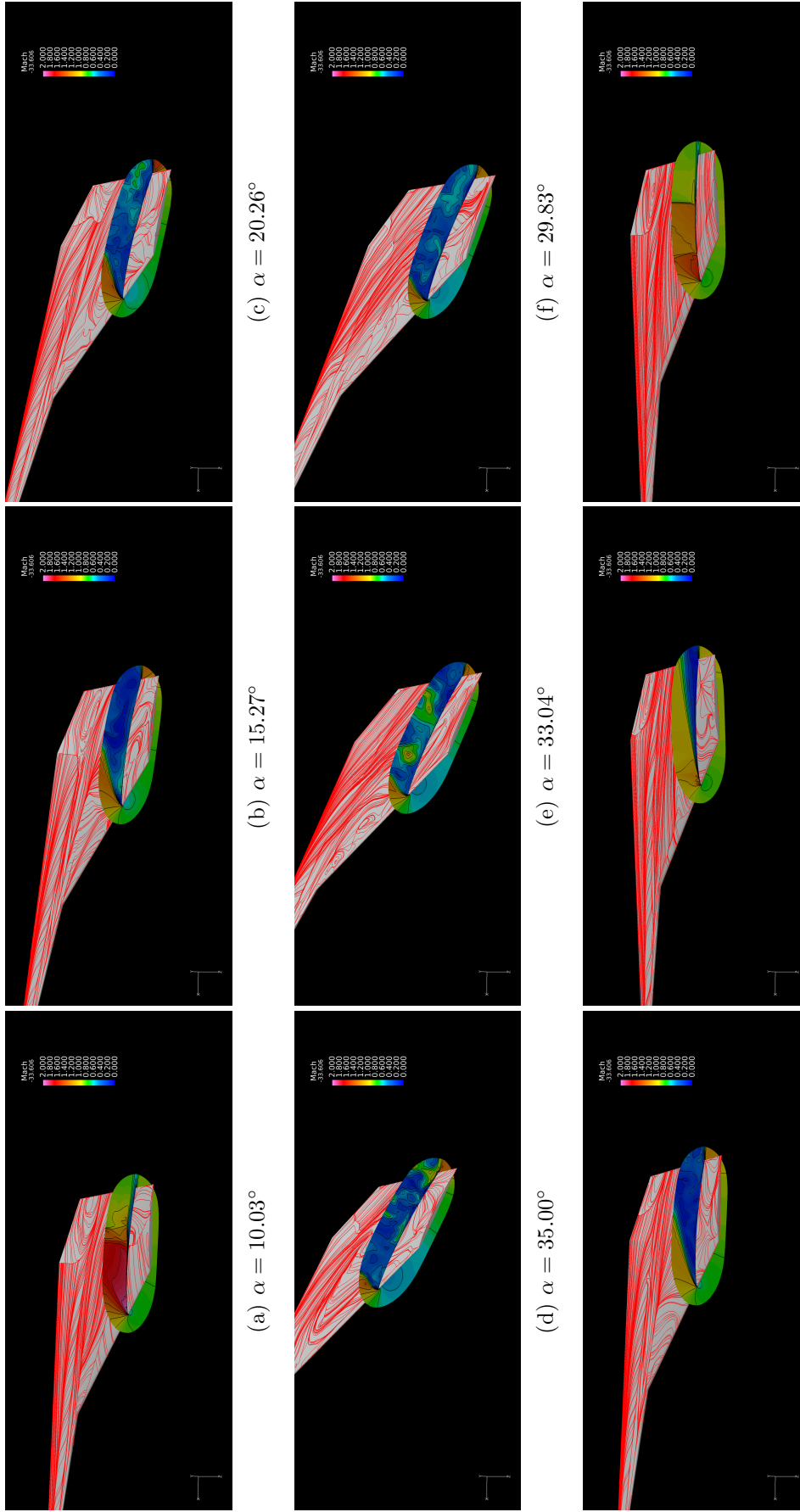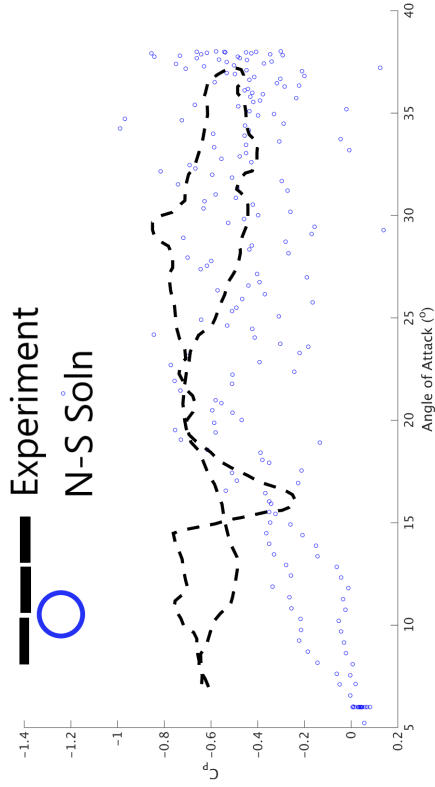(g) $\alpha = 11.54°$ (h) $\alpha = 6.00°$ (i) $\alpha = 6.00°$

Figure 4.19: First half of cosine maneuver pitching from 6° to 38° at a Mach of 0.9, oscillation frequency of 3.8 HZ

94

in Figure 4.19i. The C_P plots of the cosine of the maneuver show that after small amount of time, the surface pressure returned to the original value.

Numerous plots are displayed in Figure 4.20, which show the change in surface C_P over the entirety of the cosine maneuver. Instead of examining slices at individual pressure stations, the analysis for the cosine maneuver focused tracking the change in C_P at individual taps. This was done primarily to compare the numerical solution to data from the Cunningham experiments [6]. The plots in Figure 4.20 show the numerical solution (blue circles) plotted against the first harmonic of the unsteady pressure data gathered by Cunningham (dotted lines) against the angle of attack. Though it is standard practice to plot data collected during an experiment as discrete points, that practice was not followed here because the data from the experiments was presented in the original document as a line chart. The numerical solution was plotted as discrete points to distinguish the two more effectively. At first glance, it could be observed that the numerical solution did not match the values recorded during the experiments. However, some of the trends of the experimental data were captured. For example, the solution at the pressure tap located at 70% of the chord length had a slight shift in C_P at the lower angles of attack but bounds the experimental data at the higher angles of attack. Also, in Figures 4.20b, 4.20c, and 4.20d, the numerical solution followed a similar trend to the experimental data, especially at the higher angles of attack. Considering the differences in geometries and the challenges presented by modeling such extremely separated flows, the solution was a reasonable comparison to the data. These results helped confirm the idea that current N-S computational solvers are capable of satisfactorily modeling these unsteady flows at high Reynolds number conditions.

Cunningham also collected data on the changing forces acting on the model during the oscillatory motion. These data were then used to calculate a value for C_N over the entire motion for the entire model. Figure 4.21 shows this value plotted along with the C_N that was calculated during the numerical simulation. The plot showed excellent agreement between the experimental and numerical values. At lower angles

95

Figure 4.20: Surface C_P versus angle of attack for individual tap locations at pressure station one. Tap labels refers to Cunningham numbering system; cosine maneuver simulated at Mach of 0.9 and oscillation frequency of 3.8 Hz

(a) Tap 110, 70% chord
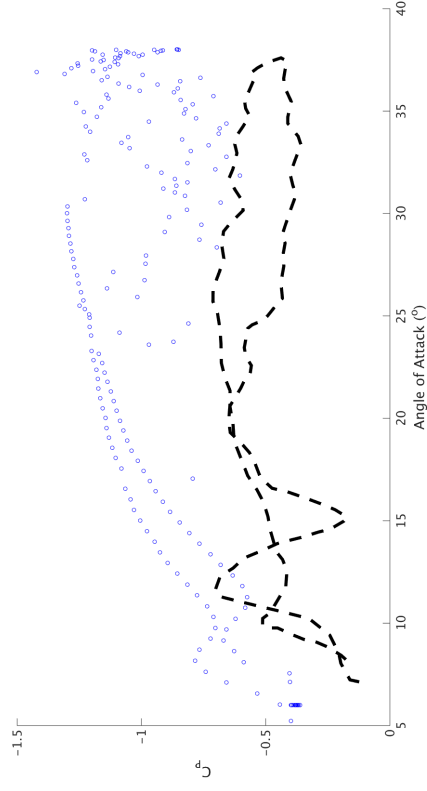
(b) Tap 111, 79% chord
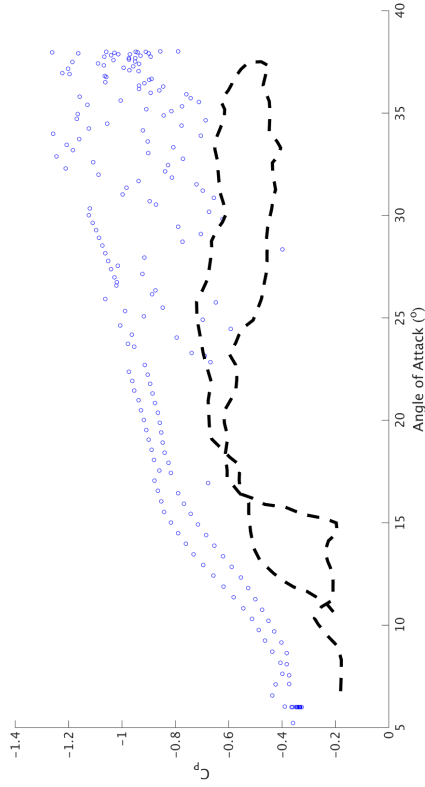
(c) Tap 113, 85% chord

(d) Tap 115, 95% chord

of attack, both sets of data changed linearly until beginning to plateau at around 22°. Even in the region of highly separated flow, the solution from the simulation is completely bounded by the values from the wind tunnel. This plot produced two important conclusions. First, like the unsteady C_P plots above, it provided confidence in the solutions being generated by the numerical model. Second, it showed the decreased sensitivity of integrated quantities to small changes in geometry and flow unsteadiness. That is why quantities like C_N can be useful for general validation of a model but might not indicate small differences in the unsteady aerodynamic behavior.
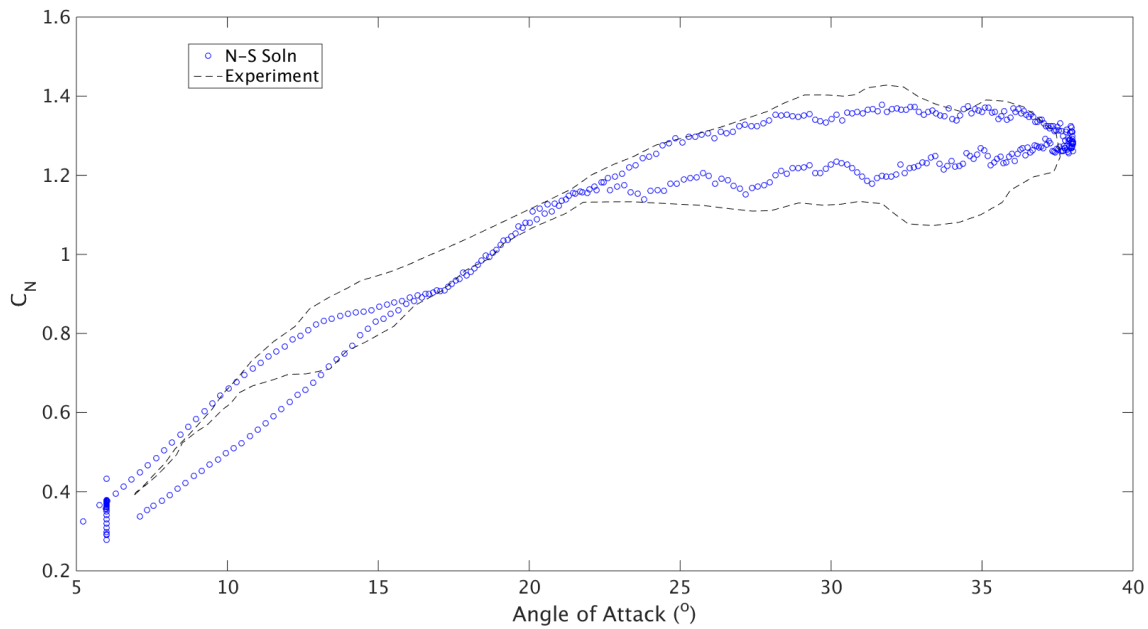
Figure 4.21: Figure showing C_N versus angle of attack from the wind tunnel experiment and numerical model during "1 - Cos" motion

4.4 Summary

The flow field around an oscillating, straked semispan was solved for numerically. The solutions were analyzed for sensitivity to a number of parameters including the starting trim angle, oscillation amplitude, oscillation frequency and free-stream Mach number. The results of the numerical simulations indicated a number of important

trends that could influence the onset or sustainment of LCO. A number of these global trends were qualitative in nature.

The most important trend was the SITES phenomenon was identified at a number of points through out many of the cases that were simulated. Since SITES remains one of the leading candidates for driving LCO, its presence during the oscillations was significant. There were also multiple simulations that showed significant separation at trim angles lower than what was found during the static analysis. This finding also applied the other direction during the cosine motion when the flow was less separated at a higher trim angle than previously observed. The delay in re-attachment could cause additional change to the forces acting on the wing and help propagate LCO. The sensitivity analysis of the different flow parameters also produced a number of interesting results.

Table 4.1: Comparison of N-S and Euler solutions showing percent change in local chord position of shock and surface C_P.

Case Number	Solver	$\Delta_x[\%]$	$\Delta_P[\%]$
ID 101	Euler	5.00	35.0
	N-S	0.85	39.1
ID 103	Euler	5.00	35.0
	N-S	0.85	46.2
ID 107	Euler	7.50	76.0
	N-S	2.99	61.3
ID 117	Euler	15.0	67.0
	N-S	65.9	192.3
ID 119	Euler	15.0	71.0
	N-S	8.00	47.0
ID 120	Euler	7.50	53.0
	N-S	8.00	47.9
ID 123	Euler	N/A	N/A
	N-S	2.96	45.7
ID 131	Euler	N/A	N/A
	N-S	43.5	16.0

In total, four different flow parameters were studied. For each of the cases analyzed, the percent change in C_P was calculated across the shock as well as the amount of translation in shock starting position. The results of these calculations

98

for pressure station one are shown in Table 4.1. The calculations were accomplished at pressure station one since that is where the Euler calculations were made. Those values are also displayed in Table 4.1. As discussed in the chapter, all four flow parameters had some sort of effect on the flow field. In general increased oscillation amplitude caused additional shock translation and strengthened the shock as well, except the 8° amplitude case. The oscillation frequency had little effect on the flow field at the lower trim angle (4°) but significantly altered the flow field at the higher trim angle (7°). The slight increase in Mach number had little effect on the surface C_P. When compared to the Euler solutions, the low trim angle and oscillation amplitude cases showed good agreement, both in shock translation and change in C_P. However, as the trim angle and oscillation amplitude is increased, the similarities diminished. This was likely caused by the increased separation at the higher angles of attack, a feature of the flow field that would be handled very differently by each model. This result pointed to the most fundamental difference between the models tested and possibly indicated an upper ceiling of applicability of an Euler solution for this type of flow.

V. Conclusions and Recommendations

The flow field around an oscillating, straked delta wing was investigated using a Navier-Stokes computational solver. The results of the numerical model shed light on a number of important trends that could help explain the prevalence of LCO in high performance aircraft that the semispan was designed to mimic. Section 5.1 summarizes the main conclusions pulled from the analysis of the numerical solutions. Section 5.2 discusses possible paths forward for furthering unsteady aerodynamic research with regards to the LCO nonlinearity.

5.1   Important Conclusions

By utilizing both quantitative and qualitative analysis techniques, a number of conclusions were drawn from the N-S numerical simulations. First, the qualitative features of the flow field match the observations made by Cunningham during the original wind tunnel experiments. While Mach contours and different flow visualizations are only a piece in understanding a flow field, observing the same general features as seen in the wind tunnel provided confidence in the solutions. Next, SITES was identified during most of the simulations. The prevalence of the phenomenon at a number of Mach numbers, trim angles, oscillation amplitudes and oscillation frequencies showed SITES could potentially drive LCO at a number of operating conditions. Third, a noticeable recovery time was required for the flow to reattach during an oscillation, even at trim angles at which no separation was present for a static flow. The delayed response of the flow showed the complicated nature of the unsteady aerodynamics. Finally, the geometry of the model had a discernible impact on a variety of flow features in the flow including to help anchor shock and eject vortices downstream. The discrepancy in surface C_P behavior between the numerical models and wind tunnel data could be because of the differences in geometry from the model that was tested in the tunnel.

The surface C_P plots showed a number of trends that concurred with the Mach contour analysis but also revealed other details. First, all four flow parameters that

100

were tested were shown to have some impact on the flow field behavior. The oscillation amplitude/trim angle had the most significant influence, with sweeping changes in the flow field occurring angles of attack around 10°. Altering the oscillation frequency had no effect on the surface C_P at the low starting trim angle but did at the higher trim angles. The separation bubble that was present for every other simulation had disappeared during the low frequency case at the higher trim angle. The separation bubble was difficult to identify with the Mach contours but there were regions of near zero velocity flow following the aft shock. Mach number had the least significant impact, only resulting in a small change to the strength of the shock. When the surface C_P from the new model was compared to the Euler results and data from the wind tunnel experiments, there were some differences. The two numerical models showed fairly good agreement at lower angles of attack, where separated flow is less prevalent. At the higher trim angles, the Euler model generally showed more shock translation and change in shock strength than the N-S solution using an IDDES turbulence model. As shown with the cosine maneuver data, the N-S model matched the general trend of the unsteady C_P measurements but did not correspond closely with experimentally-measured values. The difference between the values was likely caused by the differences in geometry used by the numerical model versus what was used by Cunningham.

The results of this numerical effort could also have an important impact on future flight tests studying the LCO phenomenon. As mentioned in Chapter 2, previous tests conducted by Tauer did not observe any significant shock translation during flight [26]. The results of the this numerical study, as well as any additional studies using the actual geometry of a F-16, could help point future tests in the direction of possible shock translation. Observing evidence of SITES during an actual flight test would be an monumental step in confirming the importance of the phenomenon in causing LCO onset.

5.2 *Future Research Recommendations*

The Cunningham wind tunnel experiments provided a good initial data set to establish the capabilities of current numerical solvers. However, there would also be a number of benefits in generating a new data set by investigating a similar flow problem with new wind tunnel experiment. First, the new data set would be more readily available than the data collected almost 30 years ago. The geometry of the new model could also be easily obtained, meaning the impact caused by a subtle geometry change would not need to be considered. Second, new flow visualization techniques could provide additional information about the flow field while also providing qualitative validation data for future numerical models. Finally, the new tunnel tests could attempt to cause the onset of legitimate LCO motion to truly understand the effect of the combined pitching and bending moments. This new data set could then be used in the creation of more advanced numerical models.

Kestrel and the numerical model created for this effort demonstrated the ability to at least qualitatively match the complex, unsteady aerodynamics around the oscillating straked semispan. The next step in the modeling progression would be to create a finite element model of a new wing and allow the aerodynamic and aeroelastic forces to deform the structure. Many N-S solvers have been coupled with finite element solver, Kestrel included. This would be in-depth and complex research project however, it would also provide great insight in to the real impact LCO has on a flow field.

Bibliography

1. Hodges, D. H. and Pierce, G. A., *Introduction to Structural Dynamics and Aeroelasticity*, Cambridge University Press, New York NY, 1st ed., 2002.

2. Bunton, R. W. and Denegri, Jr., C. M., "Limit Cycle Oscillation Characteristics of Fighter Aircraft," *Journal of Aircraft*, Vol. 37, No. 5, Sep 2000, pp. 916–918.

3. Denegri, C., "Limit Cycle Oscillation Flight Test Results of a Fighter with External Stores," *Journal of Aircraft*, Vol. 37, No. 5, September 2000, pp. 761–769.

4. Aregentini, T., Diana, G., and Rocchi, D., "A case-study of double multi-modal bridge flutter: Experimental result and numerical analysis," *Journal of Wind Engineering and Industrial Aerodynamics*, Vol. 151, 2016, pp. 25–36.

5. Cunningham, A. M., "The Role of Shock Induced Trailing-Edge Seperation In Limit Cycle Oscillations," Tech. rep., General Dynamics, 1989.

6. Cunningham, A. M. and den Boer R.G., "Overview of Unsteady Transonic Wing Tunnel Test on a Semispan Straked Delta Wing Oscillating in Pitch, Part 1," Tech. rep., Lockheed Fort Worth Company and Nation Aerospace Laboratory, 1994.

7. Cunningham, A. M. and den Boer R.G., "Overview of Unsteady Transonic Wing Tunnel Test on a Semispan Straked Delta Wing Oscillating in Pitch," Tech. rep., Lockheed Fort Worth Company and Nation Aerospace Laboratory, 1994.

8. Hope, D., *An Efficient Euler Method to Predict Shock Migration on an Oscillating Straked Delta Wing Design*, Master's thesis, Air Force Institute of Technology, 2018.

9. Meijer, J. J. and Cunningham, A., "A Semi-Empirical Unsteady Nonlinear Aerodynamic Model to Predict Transonic LCO Characteristics of Fighter Aircraft," 36th AIAA/ASME/ASCE/AHS/ASC Structures, Structural Dynamics and Materials Conference, New Orleans LA, April 1995.

10. Pope, S., *Turbulent Flows*, Cambridge University Press, 2000.

11. White, F., *Viscous Fluid Flow*, McGraw-Hill, 1974.

12. Berselli, L. and Illiesu, T., *Mathmatics of Large Eddy Simulation of Turbulent Flows*, Springer-Verlag Berlin and Heidelberg GmbH Co., 2006.

13. Perlin, M., Dowling, D., and Ceccio, S., "Freeman Scholar Review: Passive and Active Skin-Friction Drag Reduction in Turbulent Boundary Layers," *Journal of Fluids Engineering*, Vol. 138, September 2016, pp. 1–16.

14. Meijer, J. J. and Cunningham, A., "Understanding and Developtment of a Prediction Mehtod of Transonic Limit Cycle Oscillation Characteristics of Fighter Aircraft," Tech. Rep. ICAS-92.6.4.3, 1992.

15. Federal Aviation Administration, 800 Independence Avenue SW, Washington, DC 20591, *The Airplane Flying Handbook*, 2004.

16. Shur, M., Spalart, P., Strelets, M., and Travin, A., "A hybrid RANS-LES approach with delayed-DES and wall-modelled LES capabilities," *International Journal of Heat and Fluid Flow*, 2008.

17. Spalart, P., Deck, S., Shur, M., and Squires, K., "A new version of detached-eddy simulation, resistant to ambiguous grid densities," *Theoretical Computational Fluid Dynamics*, 2006.

18. Cummings, R. M., Mason, W. H., Morton, S. A., and McDaniel, D. R., *Applied Computational Aerodynamics: A Modern Engineering Approach*, Cambridge University Press, 2015.

19. Cummings, R. M., Morton, S. A., and McDaniel, D. R., "Experiences in accurately predicting time-dependent flows," *Progress in Aerospace Studies*, 2008.

20. Zhi-cheng, L. and Lei-ping, X., "Detached-Eddy Simulation of wing-tip vortex in the nearfield of the NACA 0015 airfoil," *Journal of Hydrodynamics*, Vol. 26, 2014, pp. 199–206.

21. Menter, F. and Kuntz, M., "Adaptation of Eddy-Viscosity Turbulence Models to Unsteady Separated Flow Behind Vehicles," United Engineering Foundation Conference: The Aerodynamics of Heavy Vehicles., January 2004, pp. 339 – 352.

22. Qin, N., Vavalle, A., and Le Moigne, A., "Spanwise Lift Distribution for Blended Wing Body Aircraft," *Journal of Aircraft*, Vol. 42, No. 2, 2005, pp. 356–365.

23. Pletcher, R., Tannehill, J., and Anderson, D., *Computational Fluid Mechanics and Heat Transfer*, CRC Press, 3rd ed., 2013.

24. Eymann, T., Nichols, R., and McDaniel, D., "Cartesian Adaptive Mesh Refinement with HPCMP CREATE-AV Kestrel," *53rd AIAA Aerospace Sciences Meeting*, January 2015.

25. ZONA Technology, Inc., 9489 E. Ironwood Square Drive, Scottsdale, AZ 85258-4578, *ZEUS Version 3.7 User's Manual*, 4th ed., February 2012.

26. Tauer, T., *Identifying Non-linear Aerodynamic Phenomena Contributing to F-16 Limit Cylcle Oscillation*, Master's thesis, Air Force Institude of Technology, 2015.

27. McDaniel, D., Tuckey, T., and Morton, S., "The HPCMP CREATE-AV Kestrel Computational Environment and its Relation to NASA's CFD Vision 2030," *55th AIAA Aerospace Sciences Meeting*, AIAA.

28. Weiss, J., Mohammed-Taifour, A., and Schwaab, Q., "Unsteady Behavior of a Pressure-Induced Turbulent Separation Bubble," *AIAA Journal*, Vol. 53, September 2015, pp. 2634–2645.

Vita

Captain Justin Pung was born and raised in the state of Michigan. He earned his undergraduate degree in Aerospace engineering from the University of Michigan. After earning his commission through the Air Force Reserve Officer Training Corps, he was assigned to the Air Force Research Labs, Directed Energy Directorate. This thesis completes his degree requirements to earn a Master of Science degree in Aeronautical engineering.

Permanent address: 2950 Hobson Way
Air Force Institute of Technology
Wright-Patterson AFB, OH 45433

105

REPORT DOCUMENTATION PAGE			Form Approved OMB No. 0704–0188

The public reporting burden for this collection of information is estimated to average 1 hour per response, including the time for reviewing instructions, searching existing data sources, gathering and maintaining the data needed, and completing and reviewing the collection of information. Send comments regarding this burden estimate or any other aspect of this collection of information, including suggestions for reducing this burden to Department of Defense, Washington Headquarters Services, Directorate for Information Operations and Reports (0704–0188), 1215 Jefferson Davis Highway, Suite 1204, Arlington, VA 22202–4302. Respondents should be aware that notwithstanding any other provision of law, no person shall be subject to any penalty for failing to comply with a collection of information if it does not display a currently valid OMB control number. PLEASE DO NOT RETURN YOUR FORM TO THE ABOVE ADDRESS.

1. REPORT DATE (DD–MM–YYYY) 21-03-2019	2. REPORT TYPE Master's Thesis	3. DATES COVERED (From — To) Aug 2017 – Mar 2019

4. TITLE AND SUBTITLE Tracking Shock Movement on the Surface of an Oscillating, Straked Semispan Delta Wing	5a. CONTRACT NUMBER
	5b. GRANT NUMBER
	5c. PROGRAM ELEMENT NUMBER
6. AUTHOR(S) Pung, Justin A., Capt, USAF	5d. PROJECT NUMBER
	5e. TASK NUMBER
	5f. WORK UNIT NUMBER

7. PERFORMING ORGANIZATION NAME(S) AND ADDRESS(ES) Air Force Institute of Technology Graduate School of Engineering and Management (AFIT/ENY) 2950 Hobson Way WPAFB OH 45433-7765	8. PERFORMING ORGANIZATION REPORT NUMBER AFIT-ENY-19-M-238

9. SPONSORING / MONITORING AGENCY NAME(S) AND ADDRESS(ES) Air Force SEEK EAGLE Office (46 SK/SKC) ATTN: Dr. Chuck Denegri 205 West D Ave Suite 348 Eglin AFB FL 32542-6866 Charles.Denegri@eglin.af.mil (850) 882-0396 (DSN: 872-0396)	10. SPONSOR/MONITOR'S ACRONYM(S) AFOSR
	11. SPONSOR/MONITOR'S REPORT NUMBER(S)

12. DISTRIBUTION / AVAILABILITY STATEMENT DISTRIBUTION STATEMENT A. Approved for public release. Distribution Unlimited.

13. SUPPLEMENTARY NOTES   This material is declared a work of the U.S. Government and is not subject to copyright protection in the United States.

14. ABSTRACT
Limit cycle oscillations (LCO), an aeromechnical instability similar to flutter, have affected high performance aircraft, like the F-16 and F-18, for years. To better understand the nature of LCO and why high-performance aircraft were typically afflicted, a series of wind tunnel experiments were conducted. The experiments were designed to investigate the flow field around a straked, semispan delta wing and monitor the changes as the semispan was pitched in an oscillatory fashion. By understanding the flow field around an oscillating wing, the fluid force that causes the motion could be discerned. The wind tunnel experiments and recent computational methods have focused on tracking shock movement along the top surface of the semispan to confirm the presence of shock-induced trailing edge separation, one possible LCO driver. For the current effort, a computational model was developed to compare to the results of the wind tunnel tests and discern more information about the flow features around a straked, delta wing. The computational model was constructed using the Cartesian overset capabilities of the fixed wing fluid dynamics solver Kestrel. Overall, the numerical results showed good qualitative agreement with the wind tunnel tests. Shock-induced trailing edge separation (SITES) was observed during a large number of the simulations, proving its prevalence at flow conditions pertinent to LCO motion. The high angle of attack simulations demonstrated good agreement with the experimental data, especially the integrated values.

15. SUBJECT TERMS Flutter   Limit Cycle Oscillation   LCO   SITES   F-16

16. SECURITY CLASSIFICATION OF:			17. LIMITATION OF ABSTRACT	18. NUMBER OF PAGES	19a. NAME OF RESPONSIBLE PERSON Lt Col Darrell S. Crowe
a. REPORT U	b. ABSTRACT U	c. THIS PAGE U	UU	122	19b. TELEPHONE NUMBER (Include Area Code) (937-255-6182) Email: darrell.crowe@us.af.mil

Standard Form 298 (Rev. 8–98)
Prescribed by ANSI Std. Z39.18

106